

---

# DEVELOPMENT OF ULTRA SENSITIVE LOCALISATION TECHNIQUES FOR FAILURE ANALYSIS OF SOFT BREAKDOWN EVENTS IN LOW K DIELECTRICS

---

vorgelegt von M.Sc Norbert Herfurth



von der Fakultät IV - Elektrotechnik und Informatik  
der Technischen Universität Berlin  
zur Erlangung des akademischen Grades  
Doktor der Ingenieurwissenschaften  
Dr.-Ing.

genehmigte Dissertation

Promotionsausschuss:

Vorsitzender: Prof. Dr. Jean-Pierre Seifert  
Gutachter: Prof. Dr.-Ing. Christian Boit, Technische Universität Berlin  
Gutachterin: Prof. Dr. Ingrid De Wolf, Katholieke Universiteit Leuven  
Gutachterin: Prof. Dr.-Ing Julia Kowal, Technische Universität Berlin

Tag der wissenschaftlichen Aussprache: 04. September 2020

### *Eidesstattliche Erklärung*

Hiermit versichere ich an Eides statt die eigenhändige Anfertigung dieser Arbeit. Soweit andere Werke genutzt oder zitiert wurden, sind diese entsprechend mit Angabe der Quelle gekennzeichnet.

### *Affidavit*

I hereby declare that this thesis is my own work and that it contains no material previously published or written by another person, except where due acknowledgment has been made in the text.

Berlin, den 10.06.2020

---

Datum Unterschrift

# Zusammenfassung

Das Phänomen des entstehenden Soft Breakdown Defekts bei der Degradation von dielektrischen Materialien mit niedriger Dielektrizitätskonstante wird seit vielen Jahren beobachtet. Bislang ist die Defektentwicklung noch nicht vollständig verstanden. Eine detaillierte physikalische Defektanalyse ist eine Notwendigkeit, um die Defektentwicklung zu verstehen.

Diese Arbeit beschreibt einen detaillierten Weg zur Entwicklung von Fehleranalysemethoden für Teststrukturen mit niedriger Dielektrizitätskonstante. Die entwickelten Methoden werden verwendet, um Soft Breakdown Defekte mit Probenwiderständen von  $\sim 200\text{G}\Omega$  zu lokalisieren. Anschließende hochauflösende Mikroskopie (TEM) und hochauflösende chemische Analyse (STEM-EDX) verifizieren die entwickelten Lokalisierungsmethoden und geben einen ersten Eindruck der Defektentwicklung. Das Verständnis der gewonnenen physikalischen Analyse erfordert jedoch eine detaillierte Defektcharakterisierung mit mehreren Techniken wie „electro optical frequency mapping“ oder „spectral photon emission microscopy“. Erst die Verknüpfung der Ergebnisse der verschiedenen bearbeiteten Themengebiete, wie elektrische Charakterisierung, physikalische Analyse, Defektcharakterisierung und numerische Defektsimulation hat zu einer Synergie geführt, die es erlaubt, die beobachtete Defektmorphologie zu verstehen. Die Zusammenfassung prägnanter Ergebnisse in einem Prolog erleichtert es das Zusammenwirken der einzelnen Teilgebiete zu erfassen.

# Abstract

The phenomenon of generating a soft breakdown defect on degrading low k dielectric materials has been observed for many years. So far, the development of such defects has not been fully understood. For the reconstruction of said developments, it is necessary to perform a detailed physical defect analysis.

This thesis describes a detailed way to develop failure analysis methods for low k dielectric test structures. The developed methods are used to localise soft breakdown defects with sample resistances of  $\sim 200\text{G}\Omega$ . Subsequent high resolution microscopy (TEM) and high resolution chemical analysis (STEM-EDX) verify the localisation methods developed and give a first impression of the defect development. However, understanding the acquired physical analysis requires detailed defect characterisation using multiple techniques such as electrooptical frequency mapping or spectral photon emission microscopy. Only the consideration of the results of different topics such as electrical characterisation, physical analysis, defect characterisation and numerical defect simulation has led to a synergy that makes it possible to understand the observed defect morphology. These topics have been processes in the framework of this thesis. In order to facilitate the understanding of the interrelationships of the individual parts of the thesis, a prologue provides the results of the individual topics.

# Acknowledgements

My family Anna, Dagmar, Elke and Robert for supporting me personally. Be it by believing that this doctoral thesis is achievable or by the little extra push when it was needed. To all of them for taking care of me, not working too many night shifts.

Philipp Scholz, for employing me as a tutor at the HLB Institute 10 years ago. This gave me the opportunity to grow into an excellent team. It was also Philipp who supervised my bachelor thesis and thus not only introduced me to scientific writing but also showed me how valuable a great supervisor is.

Many thanks to Clemens Helfmeier and Heiko Lohrke, who never hesitated to ask the "unpleasant" questions and therefore taught me how to deal with scientific problems.

Ingrid DeWolf, Kristof Croes and Chen Wu of imec for supporting me with knowledge in the field of back end of line reliability and, more importantly, for granting me access to the state-of-the-art test structures.

Many thanks to Michelé Simon-Najasek and Susanne Hübner from Fraunhofer IMWS Halle, who prepared the physical analysis and contributed their years of experience in this area to the discussion of the results.

A big thank you to Andreas Eckert, for the constant sample preparation. Without him many experiments would simply not have been possible. Stefan Keil, for finding uncomplicated solutions, as well as for the preparation of samples - in this case especially for bonding. Thanks to Uwe Kerst for his always open ear, especially for the more complex theoretical questions.

Thanks to Nadine Schulz, my sister in law, for offering last minute help and the willingness to engage with the topic.

My colleagues, Anne Beyreuther and Elham Amini for the extraordinary good coworking during the experimental work, paper writing and problem discussion.

A special thanks to my supervisor Christian Boit, for opening my eyes and showing me my achieved progress whenever necessary - I doubt I would have finished my thesis without his dedicated support, his eager exchange of knowledge, ideas and contacts, as well as his open-mindedness.

*Always Look On The Bright Side Of Life*  
*Monty Python*

# Content

1	Prologue.....	11
1.1	Samples and stress methods .....	11
1.2	Localisation.....	11
1.3	Physical defect analysis .....	13
1.4	Advanced evaluation methods .....	14
1.5	Conclusion .....	15
2	Introduction .....	16
3	Devices.....	18
3.1	Metal insulator semiconductor (MIS) test structures.....	18
4	Laboratory environment .....	21
4.1	Low current measurements.....	21
4.1.1	Coaxial vs. Triaxial cables .....	21
4.1.2	Keithley SCS 4200.....	22
4.1.3	Chip package .....	23
4.2	Phemos-1000 .....	24
4.3	Voltage amplifier .....	24
5	Experimental methods and experiments .....	25
5.1	Electrical characterisation .....	25
5.2	Photon Emission.....	27
5.2.1	Basics .....	27
5.2.2	Setup.....	28
5.2.3	Detectors.....	29
5.2.4	Optical resolution.....	31
5.2.5	Solid Immersion Lens .....	32
5.2.6	Experiments .....	33
5.3	Spectral Photon Emission .....	35
5.3.1	Basics .....	35
5.3.2	Setup.....	35
5.3.3	Information obtained from spectral characteristics .....	39
5.4	Electro optical frequency mapping.....	41
5.4.1	Basics .....	41
5.4.2	Setup.....	42
5.5	Optical Beam Induced Resistance Change .....	44

5.5.1	Basics .....	44
5.5.2	Setup.....	45
5.5.3	Measurements .....	47
5.5.4	Setup variations.....	47
5.5.5	Transferring OBIRCH into the optical near field .....	47
5.6	Destructive failure analysis methods.....	51
5.6.1	Destructive sample preparation using a Focused Ion Beam.....	51
6	Results .....	55
6.1	Electrical characterisation .....	55
6.1.1	Ramped voltage stress .....	55
6.1.2	Constant voltage stress .....	56
6.1.3	Failure Analysis Stress Methods – Constant-Voltage-Stress with Current-Compliance .....	58
6.1.4	Failure Analysis Stress Methods – Ramped-Voltage-Stress with Current-Compliance .....	61
6.1.5	Quantifying the level of degradation.....	62
6.1.6	Additional results .....	62
6.2	Photon emission microscopy .....	65
6.2.1	Si – CCD detector.....	65
6.2.2	InGaAs detector.....	69
6.3	Spectral photon emission.....	79
6.3.1	Hard breakdown spectra.....	79
6.3.2	Soft breakdown spectra .....	81
6.3.3	Degradation characterisation with SPEM.....	83
6.4	Optical beam induced resistance change .....	86
6.5	Physical analysis.....	89
6.5.1	Soft breakdown defects .....	90
6.5.2	Hard breakdown defects.....	99
6.5.3	Defect development.....	103
6.6	Thermal modelling .....	105
6.6.1	Defect modelling .....	106
6.6.2	Modelling results.....	107
6.7	Electro-optical frequency mapping .....	110
6.7.1	Measuring an electro-optical frequency mapping characteristic.....	110
6.7.2	Degradation monitoring with electro-optical frequency mapping .....	113

6.8	Experiments for future applications – OBIRCH with a SNOM .....	116
6.8.1	Optical near field measurements .....	116
7	Conclusion .....	118
7.1	Defect localisation .....	118
7.1.1	Photon emission microscopy .....	118
7.1.2	Optical beam induced resistance change .....	119
7.2	Physical analysis .....	119
7.3	Non Invasive defect analysis .....	119
8	Epilogue .....	121
9	References .....	122
10	List of Figures .....	126
11	List of Equations .....	131
12	List of Tables .....	132

## 1 Prologue

The active devices of integrated circuits are processed into the surface of a silicon wafer. The wiring between these active devices is set up on top and is referred to as **back end of line** (BEOL). It consists of several metal layers and electrically insulating dielectric material in between. In such a capacitive system, a considerable charge can build up and slow down the chip. The use of new porous material reduces the capacitive load of the BEOL, but suffers from the **soft breakdown** (SBD) of the dielectric material. The SBD is characterised by a constant degradation under electrical stress rather than a spontaneous **hard breakdown** (HBD), which is known from classical dielectric materials e.g. silicon oxide. In HBD a high discharge current flows over a narrow path in the dielectric, generating a significant amount of joule heat that melts and breaks the surrounding materials. Thus, the original breakdown point is destroyed and no further root cause analysis is possible. Therefore, an analysis of pre HBD degradation would be particularly important to reliability modelling and proper device design. A localisation of the degradation area is required for the physical defect analysis. This is done using **contactless fault isolation** methods (CFI). So far, the sensitivity of CFI techniques has not been high enough to match the low leakage current levels associated with a SBD defect. This work uses a combination of specific test structures and highly enhanced sensitivity of CFI techniques in order to isolate the location of dielectric degradation in soft breakdown condition.

### 1.1 Samples and stress methods

The BEOL wiring structures are built of metal and dielectric materials. Typical test structures are therefore designed as a **metal insulator metal** (MIM) material stack, in which the dielectric material is covered with metal at the front and the back. The metal electrodes are optically opaque and show high thermal and electrical conductivity, which prevents most CFI techniques from being applied to this type of sample. The recent development of **metal insulator semiconductor** (MIS) test structures, which show similar degradation characteristics as corresponding MIM test structures, has enabled direct optical access to the dielectric via the infrared transparent semiconductor. This work focuses on MIS structures and the development of CFI techniques to localise a SBD on those.

The development of electrical stress methods that enable accurate monitoring and control of the degradation state is a prerequisite for the enhancement of the sensitivity of CFI methods to localise SBD defects. A combination of **constant voltage stress** (CVS) with a **current compliance** (CC) enables the degradation to be slowed down at a predefined level.

### 1.2 Localisation

**Photon emission microscopy** (PEM) is a common failure analysis method in the field of semiconductor failure analysis. The low internal noise generation of a silicon-based CCD detector enables extraordinary long signal integration times, which is beneficial in terms of improving the **signal to noise ratio** (SNR) during weak signal measurements. The faint **photon emission** (PE) intensity that is expected from the low leakage current levels during a SBD can be sufficiently visualised by these long integration. With integration times of more than 2000s for one measurement, SBD defects featuring a leakage current of less than 1nA and a resistance of 26,5GΩ have been detected with PEM measurements from the chip

## 1. Prologue

front side using a silicon CCD detector. However, enormous progress of CFI sensitivity and image resolution has been achieved by detecting PE through the chip's backside, especially by using a solid immersion optic. The advantages of direct optical access to the low  $k$  dielectric via the back side of the device under test (DUT), which are achieved by using MIS structures, are negated by the spectral sensitivity characteristics of a silicon CCD. The signal intensity that can be measured from the chip back side is correlated to the bulk silicon thickness. By thinning the back side, the signal absorption can be minimized. However, extreme thinning of the back side to thicknesses smaller than  $5\mu\text{m}$  require specialised tools. On the other hand, measurements from the front of the DUT are limited in terms of localisation, because the front metal plate shadows the PE signal. In addition to these limitations of PEM with a silicon CCD detector, the very first detection of a SBD defect with this technique encourages further research to develop more reliable and predictable detection methods as well as to find a way to not only detect the defect but also to be able to localise it. Further progress in terms of localisation and detection sensitivity has been made with PEM and the use of an Indium-Gallium-Arsenide (InGaAs) detector. The narrower band gap of this detector material compared to a silicon detector enables the spectral parts of the light to be detected, in which the bulk silicon is transparent. The benefit of direct access to the low  $k$  dielectric, which is gained from MIS structures, can thus be utilised. On the other hand, the narrower band gap of the detector material generates a higher noise level compared to a silicon CCD detector. This results in a limited maximum signal integration time, requiring an increased basic SNR of the measured signal. The use of a solid immersion lens (SIL) increases the numerical aperture of an optical system. In combination with PE, this means an increasing amount of gathered photons, thereby increasing the SNR. By using an InGaAs detector in combination with a SIL, it is possible to reliably detect SBD defects from multiple samples with a leakage current of  $100\text{pA}$  and a DUT resistance of several  $100\text{G}\Omega$ .

Thermal laser stimulation is evaluated as an alternative method for localizing SBD defects. Whereas this technique easily localises a SBD defect from a  $1\text{nA}$  leakage current with a DUT resistance of  $35\text{G}\Omega$  there is a hardware limitation for further improvements. The  $100\text{M}\Omega$  input resistance of the available voltage amplifiers is orders of magnitude lower compared to the DUT resistance in lower SBD condition. The current that flows through the DUT from an external applied current source will be determined by the ratio of the DUT resistance and the input resistance of the voltage amplifier connected in parallel. As a result, the DUT is no longer sufficiently stimulated by an externally applied current for lower levels of degradation, so that the applied laser cannot generate a sufficient voltage alteration. Even though this effect can be tempered by means of proper signal amplification and filtering. With the available hardware, the minimum degree of degradation, which enabled defect localisation came from a DUT with  $35\text{G}\Omega$ .

Electro optical frequency mapping (EOFM) allows visualising local changes in the index of refraction. In silicon, the index of refraction is related to the effective charge carrier density. An electrically stressed MIS system changes its charge carrier density at the interface between dielectric and silicon and below in relation to the applied voltage. Consequently, EOFM measurements can directly deduce locally changed electrical field strength, which lead to local changes in the charge carrier density. By sweeping the DUT input voltage and analysing the EOFM signal it is possible to extract an EOFM-voltage characteristic. As the measured MIS structure degrades, the EOFM-voltage characteristic changes. This change takes place gradually in SBD, whereby the relative change of various characteristic parameters of the measured structure e.g. the flat band voltage, can be determined. In HBD

the EOFM-voltage characteristic changes significantly compared to the SBD, allowing to determine between both degradation states, without knowledge of the sample resistance. Overall, EOFM offers a way to detect and monitor the SBD of MIS systems. Whereas no localisation of a SBD has been demonstrated so far, the additional use of a SIL will significantly increase the optical resolution. Compared to other failure analysis methods, the measurement of an EOFM-voltage characteristic applies a lower voltage stress to the DUT.

As stated above, the localisation of the SBD defect is a necessary step in planning physical analysis of such a defect. Due to the development of electrical stress methods specially designed for low intensity PEM and the resulting reliable SBD defect detection from defects featuring a leakage current of 100pA, it is now possible to plan and perform an accurate physical analysis of SBD defects. Overall, this thesis discusses physical results from two different levels of HBD defects and from several samples with different SBD defect degradation levels, including a defect that was localised from a 10pA leakage current from a 3.4T $\Omega$  sample.

### 1.3 Physical defect analysis

With the PEM assisted localisation, a preparation of 100nm - 500nm thick sample lamellae of the defects is possible. A transmission electron microscopy (TEM) analysis of the prepared sample lamellae gives a detailed optical information of the defect morphology. Even though the HBD is electrically defined by a point at which the current increased by several orders of magnitude in a short time, MIS structures in combination with a current compliance enable the analysis of different levels of a HBD. A TEM-analysed HBD defect from a 12k $\Omega$  resistance sample shows a defective area with a diameter of 200nm on the top of the dielectric layer which, extends downwards into a filigree copper-structured hemisphere within the bulk silicon featuring a diameter of 400nm. A second HBD defect analysed from a sample with a one order of magnitude higher resistance of 314k $\Omega$  also shows a hemispherical defect with a diameter of 400nm within the bulk silicon. Compared to the more degraded defect, the defect hemisphere is only partially filled with filigree copper structure, while the remaining part of the hemisphere consists of amorphous silicon. With a defect diameter of 200nm inside the dielectric layer, the defect dimensions are similar in both HBD levels analysed. An analysed SBD defect with a resistance of 260G $\Omega$ , i.e. a resistance six orders of magnitude higher compared to the lesser-degraded HBD defect shows a different defect morphology. The defect region inside the low k dielectric has shrunk by 50% to a diameter of 100nm. Still, a hemispherical defect of amorphous silicon can be found inside the silicon. Even though, the defect diameter has only shrunk by approximately 40%, the filigree copper structuring that was observed in both HBD defects could not be found in any SBD defects. This observation was verified by multiple samples, all of which showing the same characteristic defect morphologies. This leads to the hypothesis, that the low ohmic behaviour in HBD is mainly dominated by the copper recrystallization within the bulk silicon. In contrast, the dimensions of the hemispherical defect of amorphous silicon as well as the defect dimensions inside the low k dielectric increase during SBD degradation.

A hypothesis of the defect development based on the presented physical analysis of SBD defects as well as the physical analysis of different levels of HBD defects has been developed.

#### 1.4 Advanced evaluation methods

An energy dispersive x-ray (EDX) analysis and spectral photon emission measurements are performed to obtain a better insight into the changing defect morphology. With EDX analysis, it is possible to measure a detailed element map of the analysed defect. This leads to a better understanding of the material movement between different analysed levels of degradation. Spectral photon emission microscopy provides more information about the characteristics of the source of the photon emission. It allows identifying the physical reason for the photon emission. The parameter extraction from measured photon emission spectra at different degradation levels enables the monitoring of changing parameters of the photon emission origin. A simulation of the thermal conditions during the analysed SBD defect is evaluated by a finite element solver program.

The element mapping of the analysed defects by EDX confirms the results of the physical analysis. A mapping of tantalum allows the detection of a locally thinned diffusion barrier in the SBD defect and a locally missing diffusion barrier for the HBD. This explains the copper silicon diffusion, which is massive during the HBD defect, but which can also be found in the analysed SBD defect. All analysed degradation levels feature a hemispherical shape of amorphous silicon, which contains diffused copper. While the copper content inside the silicon increased with increasing degradation, the copper at HBD begins to recrystallize within the defective silicon hemisphere. This leads to the conclusion that the amount of thermally driven copper silicon interdiffusion determines the resistance of the sample. In HBD the degradation process is mainly characterised by an increasing area of recrystallized copper inside a hemispherical shape of amorphous silicon. During the SBD, the size of the amorphous silicon hemisphere grows.

Spectral photon emission measurements are another method to monitor the SBD degradation. In addition, it allows verifying the hypothesis developed from physical analysis results. The spectra of all analysed degradation levels show an exponential relationship between the intensity of photon emission and the photon energy. This relation is characteristic of field assisted photon emission. The exponential slope of this kind of photon emission spectra can be evaluated to extract the electron temperature parameter. The source of the photon emission is thus characterised. It is shown that the source of the photon emission in MIS structures is partially localised inside the low k dielectric as well as in the bulk silicon. The ratio in which both parts contribute to the full photon emission signal is related to the degradation level. In HBD condition, the low k dielectric layer is shortened by copper diffusion. Thus, the photon emission has its origin in the bulk silicon. This is supported by physical analysis, in which main morphological changes between different HBD states are located within the amorphous silicon hemisphere inside the bulk. During the SBD, the electron temperature is logarithmically connected to the DUT resistance. It indicates the continuous change in the internal field properties during the SBD degradation, where physical analysis has shown dimensional growth of the defect as well as a semi-intact dielectric layer.

To understand the appearance of an amorphous silicon hemisphere in all defects analysed, a numerical model of the DUT, including the SBD defect, can be used to simulate the thermal conditions during the SBD defect. Whereas the amorphous recrystallisation of silicon requires a temperature peak of at least 1414°C, an alloy of silicon and copper can reduce this temperature. Depending on the material ratio, the required temperature can be

reduced to a minimum of 802°C. The simulations show that a sweet spot for the applied power density exists to significantly heat up the test structure.

## 1.5 Conclusion

The special characteristics of BEOL MIS test structures have been successfully utilised to localise different levels of low k dielectric degradation. Using photon emission microscopy, a SBD defect with a DUT resistance of 2.6TΩ and a leakage current as low as 10pA was localised. The localisation of such low degradation levels within area test structures enables further research to investigate new approaches for analysing root causes of SBD degradation within a low k dielectric. Performing a physical analysis of the localised defects with subsequent optical and chemical analysis has presented new results of the SBD defect morphology. Subsequent numerical simulations of the thermal conditions within the defect joint by spectral photon emission measurements at different defect levels deepen the understanding of the presented physical analysis.

## 2 Introduction

The rapid development in the field of microelectronics in the last decades has been accompanied by ever-new upcoming problems. In popular media the decreasing minimum feature size is the number that is cited frequently. However, making use of this minimum feature size is accompanied by other, not so popular, problems that need to be solved to take full advantage of the improved feature size. The minimal feature size is usually used to design the active devices, created in the initial process steps. This part of the integrated circuit is called the front end of line (FEOL). In order to create an actual working circuitry, the active devices (the FEOL) need to be wired. An interconnect system built on top of the FEOL creates the functionality of the integrated circuit. This interconnect system is called the back end of line (BEOL). The increasing device density in the FEOL correlates with an increasing number of metal layers in the interconnect system. Different technical and electrical requirements for the lower interconnect layers compared to the upper layers established the name of the middle end of line (MEOL) for the interconnect layers directly on top of the FEOL. The capacitive characteristics of the BEOL and the MEOL are inevitable. Thus, the signal propagation initiated by the FEOL is slowed down by the capacitive load of the MEOL and the BEOL. Reducing the capacitive load of the interconnect system is essential in order to maintain the performance increase gained from the improved FEOL. One way to reduce the capacitive loss in the interconnect system is to use new insulation materials between the metal layers. The traditional used dielectric material is silicon oxide. Due to decades of research with silicon oxide as a dielectric, it has become common to handle this material within a complex process. Nonetheless, it has a relative dielectric constant ( $k$  value) of 3.6, which limits a further reduction of the capacitive loss. Other materials promise lower capacitive losses due to lower  $k$  values. The development of new dielectric materials with low  $k$  values has resulted in a porous dielectric structure. Many problems that came up with these kinds of materials have been sufficiently addressed, so porous low  $k$  dielectrics with a  $k$  value of 2.3 are included in today's functional high volume technology nodes. However, a further reduction of the effective dielectric value is desirable for the ongoing development in the FEOL. With an increased ratio of pores, the effective dielectric constant of the material can be reduced, but existing problems such as mechanical stability and electrical reliability are becoming increasingly complicated to avoid or solve. The degradation behaviour of low  $k$  dielectrics differs from classical dielectric materials. Low  $k$  materials show a constant degradation under electrical field strengths that are below the material specific maximum electrical field strength. This degradation process is called the soft breakdown (SBD). The constant degradation during a SBD usually ends in a hard breakdown (HBD) of the material. The HBD is related to high current densities that generate an extraordinary amount of joule heat. This joule heat leads to a destruction of the defect area. A common approach to solving the problem of the SBD is the use of statistical evaluation methods such as Weibull plots. Thus, the product lifetime estimation can be extracted from the statistical analysis from a set of samples with variations in the process parameters. This approach has led to success in the past. However, it cannot solve reliability problems for new experimental materials. As a result, the reduction of the  $k$  value is stuck at around 2.3. So far, due to the lack of physical evidence of the SBD defect, it has been difficult to prove simulations and theories about the development of the SBD defect. The preparation of a physical analysis requires a precise localisation of the defect, which is generally implemented with failure analysis methods. The localisation of HBD defects is an everyday business for failure analysis laboratories. However, the HBD defect localisation techniques commonly used are not sensitive enough to localise a SBD defect. In addition, the destructive character of a HBD extinguishes the evidence of a SBD. Therefore, for better understanding what happens

during early defect development as well as to prove or disprove existing theories about SBD defect development, it is necessary to develop advanced failure analysis methods that can be used to detect and localise a SBD defect.

In this work a new generation of a low k dielectric material with a 45% porosity and a k value of 2.0 is used. To date, the electrical reliability problems associated with this material have not been sufficiently resolved for adopting it into high volume production. Therefore, this makes this material perfect for developing advanced failure analysis methods. BEOL test structures are used to characterise new materials. Traditionally, the BEOL is approximated by a metal insulator metal (MIM) material stack. Thus, test structures for the BEOL are commonly designed as MIM structures. In terms of failure analysis this setup is one of the worst possible setups. The metal optically encapsulates the low k dielectric from the front as well as from the back. The high thermal conductivity of the metal makes it difficult to apply heat-based failure analysis methods. In addition, the high electrical conductivity of the metal is likely to prevent the development of locally changing charge distributions, making it difficult to use failure analysis methods based on local voltage changes. Recent research carried out by the Interuniversity Microelectronics Centre (imec) has shown that specially designed test-structures which feature a semiconductor on the underside of the low k dielectric instead of a metal electrode have an electrical degradation behaviour similar to that of equivalent MIM test structure. These new metal insulator semiconductor (MIS) test structures open the field for a wide variety of failure analysis methods, including optical and thermal beam-based methods. The field of semiconductor failure analysis offers a great base of knowledge for different kinds of beam-based techniques. However, the current levels as well as the device resistances related to the SBD are orders of magnitude lower compared to common semiconductor device analysis. This challenges the detection sensitivities of known failure analysis methods. The evaluation of different failure analysis methods such as photon emission microscopy, thermal laser stimulation and electro optical frequency mapping to localise a soft breakdown defect in BEOL test structures is set out in the first part of this thesis. In this part, the detection sensitive limits of the methods analysed will be assessed to determine a minimal level of degradation, and the localisation accuracy for further physical analysis will be evaluated. The limiting factors of the different techniques will be identified, and improvement possibilities will be shown. Succeeding physical analysis validate the developed localisation techniques.

### 3 Devices

Within an integrated circuit, the back end of line (BEOL) is the interconnect system that connects the active parts of the chip. Whereas the connections are realised with metals, the spacing material in between must be insulating. Reducing the capacitive load that is caused by the insulating dielectric material is subject of research. The development of porous low k materials significantly reduced the capacitive load of the BEOL. However, these materials show a different degradation behaviour than the classical dielectric material. Under nominal operation conditions, the low k material show a constant degradation, this degradation is called the soft breakdown (SBD). Contrary to the hard breakdown (HBD) during a SBD the device parameters are changing over time but the device itself is still functional. The characterisation of the SBD region for the analysed samples is performed in this thesis and presented in 6.1.

The natural design of a test structure that aims to characterise the insulating BEOL material would be realised as a metal insulator metal (MIM) material stack. However, different variations of BEOL test structures have been developed over the last decade to provide more insight into the degradation process of low k dielectrics. Among other variations of the test structure designs, a one-sided replacement of the copper metallisation by other materials was realised to investigate specific degradation causes. This has led to a development of a metal insulator semiconductor (MIS) test structure by imec [1–5], the research center on nanoelectronics and digital technologies in Leuven (Belgium).

Aiming for failure analysis, especially the localisation of failures within the low k dielectric material, the analysis of MIS structures is much more rewarding compared to MIM structures. MIS structures allow direct optical access to the object of interest, the low k material, respectively. In contrast, in MIM structures, the low k material is encapsulated with metal from the front as well as from the back. The optically opaque properties as well as the good electrical and thermal conductivity of metal complicate the failure analysis on MIM structures significantly compared to MIS structures.

#### 3.1 Metal insulator semiconductor (MIS) test structures

The available MIS test structures are designed and fabricated by imec. The low k dielectric used is also a imec development. A schematic drawing of the available MIS test structure is shown in Figure 1. The base of the test structure is n-doped bulk silicon. The back of the silicon is completely coated with aluminium to achieve a low ohmic contact of the n-doped bulk silicon. In the area of the examined test structures, the aluminium is locally removed. The front side of the silicon is isolated with a few nm of thermally grown oxide. The examined low k dielectric is produced on top of the thermal oxide. The low k dielectric is a porous SiOCH type material with an effective dielectric constant of  $k=2.0$ . The 40nm thick dielectric layer has a porosity of 45%. The top of the low k dielectric is sealed with a physically vapour-deposited Tantalum-Nitride / Tantalum diffusion barrier. This kind of sealing is a standard to prevent the overlying copper from diffusing into the dielectric. The copper is connected via an aluminium plug, which creates a low ohmic connection to a larger probe pad.

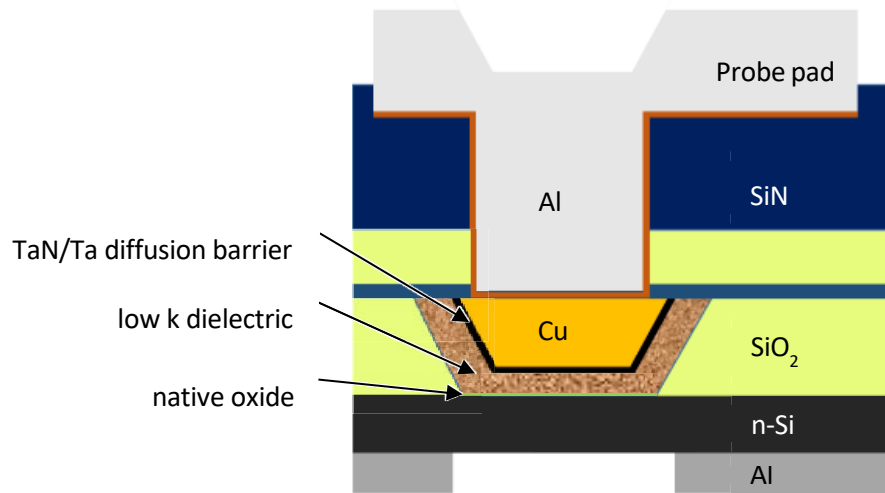


**Figure 1: Schematic drawing of a metal insulator semiconductor test structure; the aluminium on the back is removed locally to grant optical access to the bulk silicon and the test structure**

With this sample layout, a capacitive MIS test structure is formed between the bulk silicon and the upper copper electrode. With the fixed height of the low k dielectric the capacitance per unit area is determined by sample provider (imec) to:  $c''_{ox} \approx 5 \times 10^{-8} \frac{F}{cm^2}$ . The width and the length of the test structures vary from  $1\mu m \times 1\mu m$  up to  $1000\mu m \times$

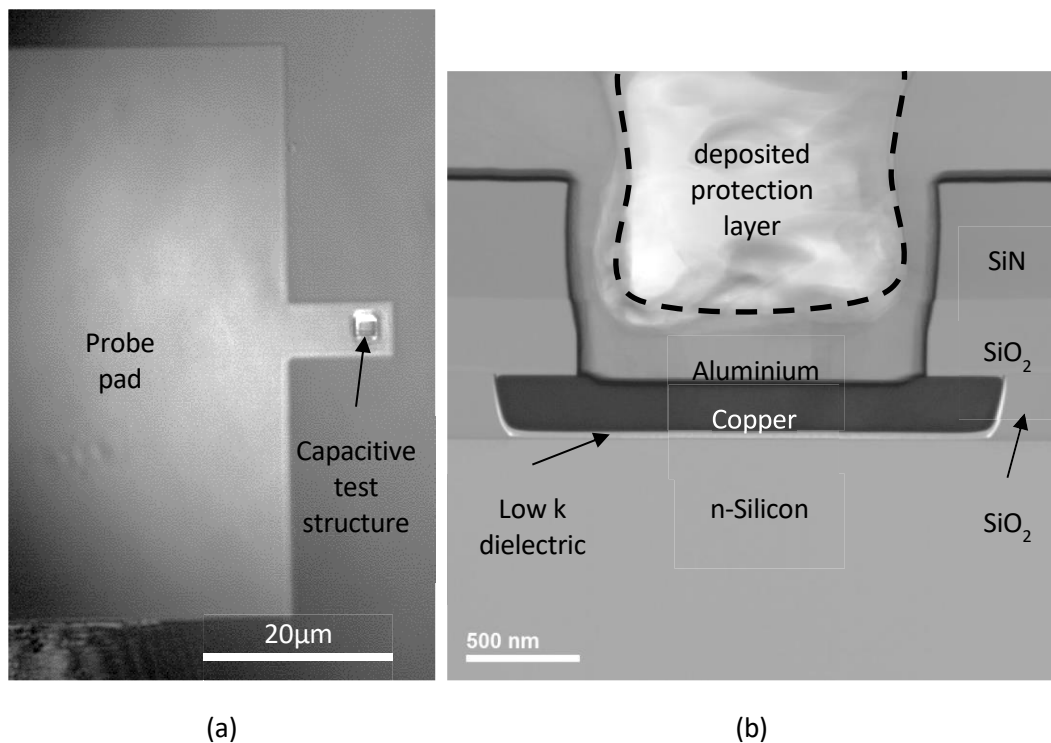


**Figure 2: Images of a analysed non-degraded test structures; (a) laser scanning microscope image measured from the back; (b) Cross section measured with a transmission electron microscope**

### 3. Devices

1000 $\mu\text{m}$ . The leakage current through the capacitive test structure determines the level of degradation of the isolating low k dielectric.

Figure 2a shows a back view of the test structure. The image was measured with a near infrared laser scanning microscope that can measure through the bulk silicon. Thus, the cavity of the capacitive test structure can be identified. Figure 2b shows a cross section of the MIS test structure, a transmission electron microscopy (TEM) image being displayed. To prepare this kind of image, on top of the sample a protective layer must be deposited. This protective carbon layer fills the cavity above the aluminium plug. The thin layers sealing the low k dielectric, namely a native silicon oxide and the Tantalum nitride – Tantalum diffusion barrier, cannot be resolved on this overview image.

## 4 Laboratory environment

### 4.1 Low current measurements

The electrical characterisation of the degradation behaviour of insulating materials places advanced demands on the electrical characterisation system. Ideally, the leakage current of the dielectric material is minimal and the acceptable electrical field across the dielectric is maximal. Whereas, in this context “minimal” and “maximal” means as high or as low as possible. Furthermore, the leakage current increases by many orders of magnitude during the degradation of the isolating material. These characteristics can be transferred into the measuring device:

- The system must be able to measure small leakage currents
- Voltage levels that exceed normal characterisation parameters for semiconductor device must be available
- High power outputs are required to follow the leakage current in higher levels of degradation

#### 4.1.1 Coaxial vs. Triaxial cables

In Order to measure low current levels, it must be ensured that the signal measured comes from the device under test (DUT) rather than the measurement setup. Figure 3 shows a schematic drawing of a coaxial [6] and a triaxial cable [7]. The coaxial cable uses the force signal line to guide the voltage to the DUT and the shielding line to implement the earth contact. The insulating material between force and shield is subject to a leakage current. The limitations of coaxial cables are shown in this simplified calculation of the leakage current:

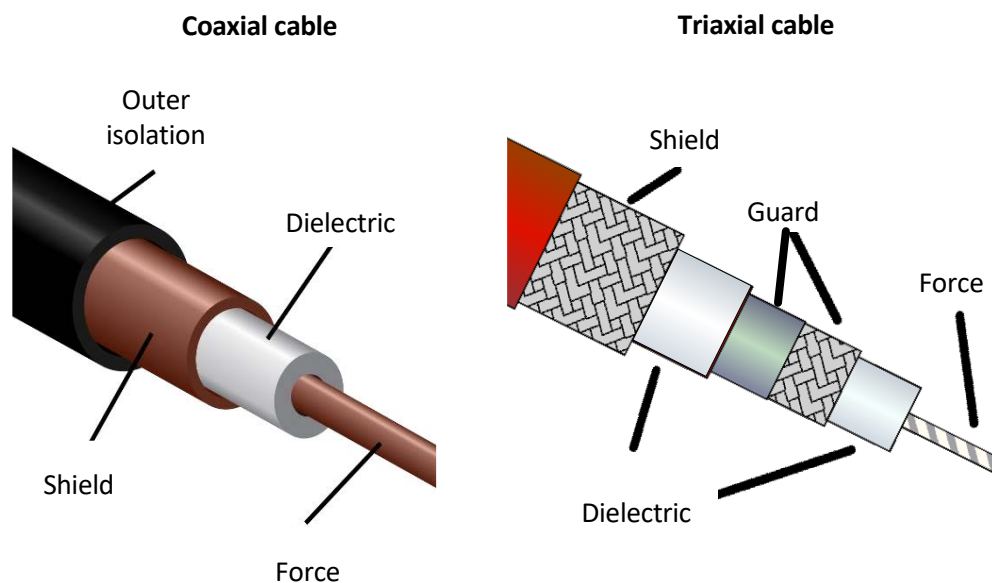


Figure 3: Schematic drawing of coaxial and triaxial cable cross sections.

#### 4. Laboratory environment

The absolute dielectric resistance of the coaxial cable depends on the length and quality of the cable. However, an assumed resistance of the dielectric material within a coaxial cable of  $R_{di} = 100G\Omega$  is realistic. Furthermore, the applied voltage is assumed to be 10V. By Ohm's law the leakage current can be calculated to

$$i_{leak} = \frac{10V}{10^{11}\Omega} = 0,1nA$$

Such a high parasitic leakage current from the cable means it is not possible to measure leakage currents from the DUT in the range of pA.

Triaxial cables use a third signal line, which is located between the force and the shield line, the so called guard line. This guard line is operated with the same voltage as the force line. The leakage current from the force line is therefore related to the voltage difference between force line and guard line. Assuming the same cable properties as for the coaxial cable and a voltage adjustment between force and guard line of  $\frac{1}{100.000}$ , the leakage current calculates to:

$$i_{leak} = \frac{10.0001V - 10V}{10^{11}\Omega} = 1fA$$

Consequently, guarding the force line reduced the leakage current by many orders of magnitude compared to measurements with only a shield line. This simplified calculation clarifies the inevitable requirement of triaxial cables for low current measurements. As a rule of thumb, it can be said that measurements below 1nA should use guarding [8]. However, a practical problem of low current measurements is keeping the guarding and shielding as close to the DUT as possible, especially when the DUT is packaged. The influence of the package to the minimum current measurable is discussed in chapter 4.1.3.

##### 4.1.2 Keithley SCS 4200

The laboratories at the TU Berlin offer a wide variety of electrical characterisation tools. The available Keithley SCS4200 is equipped with multiple source measurement units (SMUs) as well as two pre-amplifier units (preAmp's). The current measurement resolution of a preAmp unit is specified to 0.1fA. The maximum current output is 100mA and the maximum power is limited to 2W [9]. These specifications fit the requirements for dielectric test structure characterisation listed above, which qualifies the SCS4200 for the planned experiments.

Preliminary tests have shown that the SCS 4200 can achieve the specified measurement accuracy under ideal measurement conditions, with terminated connection jacks. However, a real measurement setup reduces the minimum measurable current depending on various factors. For example, connecting micromanipulators to the preAmp's increases the current noise floor to 10fA. This is still good enough to characterise the available low k dielectric test structures. The electrical characterisation of the available test structures can be performed directly on the wafer by bringing the sample directly into contact with

micromanipulators. In summary, the accessible Keithley SCS4200 is a suitable choice to characterise the low k dielectric test structures available.

#### 4.1.3 Chip package

To perform failure analysis measurement from the back of the chip, it is inevitable to package the test structures. Throughout the experimental work of this thesis it was found that the selection of the correct sample package is important, as it significantly influences the leakage currents and the current noise floor respectively. Three different types of packaging were tested and compared in terms of minimally measurable current levels. Real measurement conditions were used for these tests. This means that the test structures were mounted into the package, bonded and moulded.

Ceramic packaging showed by far the best electrical results as the measurement resolution did not change significantly compared to wafer level measurements with micromanipulators. Unfortunately, a ceramic package is not suitable for back side analysis as its mechanical modification is not practicable.

The second type of package was a ball grid array (BGA) package. The preparation for backside measurements of this package type was well understood as it has been used by the TU-Berlin failure analysis group for the last decade. Unfortunately, a dedicated test series revealed a leakage current of approximately 1-10pA. Even a delayering of the package did not reveal the cause of the increased leakage. With such a significantly increased leakage current, the package is not suitable for the planned low current measurements.

Finally, a printed circuit board (PCB) package offered good electrical conditions and easy-to-handle mechanical preparation. The packaged and moulded chip with the package mounted in an outbreak box showed a current noise level of 100fA. This is one order of magnitude higher than wafer level measurements, but still good enough to monitor the degradation of the analysed low k dielectric test structures. Figure 4 shows the PCB package with a mounted chip. The moulding of the chip is optional depending on the planned experiments.

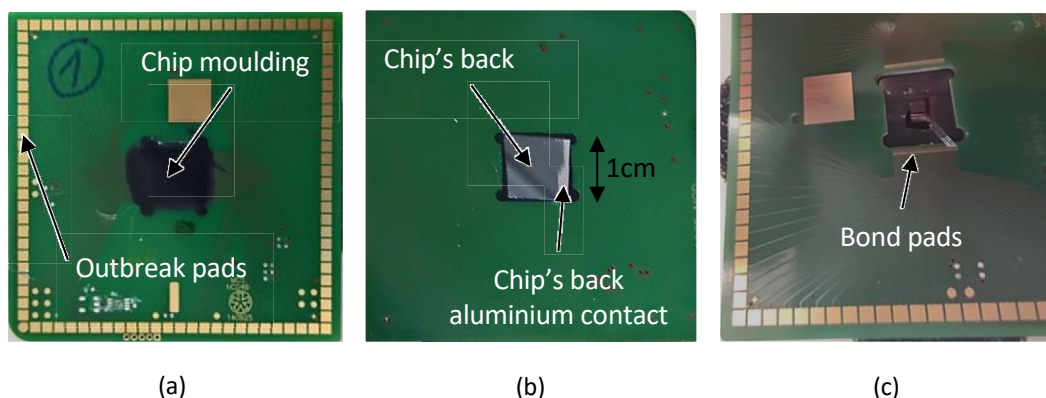


**Figure 4:** Printed circuit board package for low current measurements; (a) from the front side with moulded chip; (b) from the back side with the blank chip back side and aluminium substrate contact visible; (c) front side view of the non-moulded chip – showing the bond wires

## 4. Laboratory environment

### 4.2 Phemos-1000

The Phemos-1000 is a high resolution emission microscope that combines various methods for semiconductor failure analysis in one tool. Due to the capability of exposing weak light emissions as well as heat emissions from operating semiconductor devices, the implementation of photon emission microscopy (PEM) and optical beam induced resistance change (OBIRCH) measurements is a matter of course. In addition, various laser source units can be used to acquire high resolution laser scanning microscopy images and perform electro optical probing / electro optical frequency mapping. The broad possibilities of the Phemos-1000 make it the ideal tool for the development of failure analysis methods for low k dielectric test structures. Due to the possibility of using a solid immersion lens (SIL), the resolution of the acquired measurement results need not be considered. The hardware specifications of the individual measurement methods as well as the basics of the corresponding measurement technique are described in the corresponding chapter "Experimental methods and experiments".

### 4.3 Voltage amplifier

Various failure analysis methods require measurements of low voltage signals as well as the possibility to adjust the gain factor, the bandwidth and the coupling mode. Stanford Research's low-noise preamplifier SR560 combines these requirements. In addition, the device can be operated with a highly stable battery power supply. Throughout this thesis it will be shown that the input resistance of the voltage amplifier is significant for the positive result of failure analysis techniques based on thermal laser stimulation. The input resistance of the SR560 is 100M $\Omega$ , which is a several orders of magnitude higher resistance than most operating semiconductor devices. However, a transistor operating at sub-threshold or functional capacity can feature resistances of the same order of magnitude or even higher. Figure 5 shows a schematic drawing of the front panel of the SR560, taken from the operations manual.

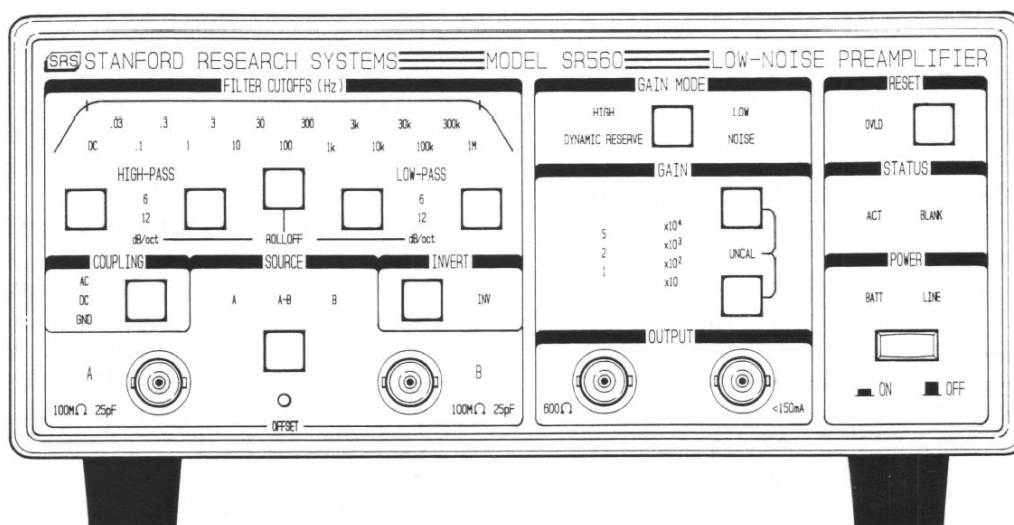


Figure 5: Schematic drawing of the front panel of the low noise preamplifier SR560.

## 5 Experimental methods and experiments

### 5.1 Electrical characterisation

In order to plan controlled degradation, it is essential to fully understand the degradation behaviour of the analysed samples. However, due to the statistical nature of the degradation process, gathering convincing degradation data can be time consuming. In the past, four types of electrical measurements have been discussed and performed by the reliability community to characterise dielectric breakdown [10]:

1. The ramped voltage stress (RVS) is the most basic characterisation method. By gradually increasing the applied voltage, the device under test is stressed until it fails. This method can generate stress data with short turn-around times. Monitoring the breakdown voltage enables direct measurement of the breakdown voltage ( $V_{BD}$ ). RVS measurements do not allow to directly extract information about the product lifetime. Nevertheless, the RVS can be used during early process development in the manufacturing environment to investigate the dependence of  $V_{BD}$  on different production parameters, e.g. the structural geometry.
2. One of the less discussed characterisation techniques is ramp current stress (RCS) or exponential ramp current stress (ERCS). Here the applied current is increased during the measurement. The measurement of the voltage drop at the DUT provides information about the basic functionality of the device. In some cases, direct monitoring of the breakdown current ( $J_{BD}$ ) can be useful. Additionally, a first approximation of the charge to breakdown ( $Q_{BD}$ ) can be extracted from RCS measurements. As with the RVS method, this technique cannot extract lifetime information directly.

Overall, due to the short turn-around time and the limited parameter extraction capability of (E)RCS and RVS measurements, they are particularly suitable for early process development in a manufacturing environment.

3. One method of characterisation that is considered closer to device operation is constant voltage stress (CVS). Stressing the device with a higher than nominal constant voltage accelerates the degradation compared to normal device operation. The stress conditions are considered as real device operation. Correctly selected stress parameters will not change the defect mechanism but will accelerate the degradation. A CVS is the classical method to perform time dependent dielectric breakdown (TDDB) measurements. With appropriate TDDB measurements, voltage or field acceleration models can be extracted. These models allow the extrapolation a lifetime estimate for a certain operational voltage. The time-consuming nature of these measurements makes it difficult to implement them in an inline workflow. Therefore, these measurements are best suited in a research environment.
4. The constant current stress (CCS) keeps the stress current constant and monitors the voltage drop at the DUT. Increasing leakage current is often considered the main driver of degradation. The limited current during a CCS measurement limits the rate of degradation. This is beneficial if the degradation processes needs to be controlled accurately. On the downside, choosing the correct current level can be challenging. If the current level is too low, the degradation might be stuck in the

## 5. Experimental methods and experiments

defect nucleation. If set too high, the defect might be driven into HBD too quickly. CCS can evaluate the breakdown dependency of process conditions such as the content of dielectric nitrogen, annealing temperatures or impurities in the dielectric surrounding electrodes [11].

Due to the statistical nature of the dielectric breakdown, the turn-around time for CVS and CCS measurements can vary by many orders of magnitude from sample to sample. Whereas these two methods allow an accurate prediction of the expected lifetime, (E)RCS and RVS measurements have a short turn-around time. All four methods have their own advantages and disadvantages, as well as their own field of application. Ambitions to make use of the fast turn-around times from (E)RCS measurements and convert them into accurate live time models obtained from CVS results have been subject of current research [10] but have not been widely established so far. As a result, it is necessary to carefully evaluate the depth of degradation characterisation required, the time frame available and to select the correct characterisation method.

This work aims for the development of failure analysis methods to localise the early degradation. In this context, a well-controlled degradation process is beneficial, which keeps degradation at a specified level. CCS measurements fulfil this requirement. However, in order to determine the working point for the following degradation experiments, RVS measurements are performed for all analysed structures. The following CVS measurements give additional information about the degradation behaviour.

## 5.2 Photon Emission

### 5.2.1 Basics

In the field of semiconductor device failure analysis, photon emission is a well-known technique that detects photons emitted by the device under test (DUT). These photons are usually emitted because the DUT is electrically stimulated. In the past, photon emission was used for the back end of line (BEOL) to detect hard breakdown (HBD) failures. Contrary to the HBD, the current levels involved in the soft breakdown (SBD) are orders of magnitude lower. Traditionally, these low current levels have prevented the use of photon emission for SBD defect detection. This chapter discusses the theoretical basics of photon emission to understand the measuring principle as well as its limiting sensitivity factors.

There are two main mechanisms that can cause photon emission in a semiconductor device, both are shown schematically in Figure 6 [12]. Recombination of electron hole pair is a process that is well known and utilised in LED technology. A forward biased pn-junction causes a minority carrier accumulation at the verge of the space charge region. As the recombination rate is linearly related to the minority carrier concentration, an increased recombination rate at the edge of the space charge region is the result of the forward bias applied. The recombination of electron hole pairs can generate photons proportional to the flowing current. The energy of the emitted photons is related to the material-specific band gap. However, in the case of silicon-based devices, the ratio of emitted photons to the applied current is significantly lower compared to that of LED materials. This effect is mainly caused by the fact that silicon is an indirect semiconductor, whereas direct semiconductors are preferably used for LEDs. Further information on direct and indirect semiconductors can be found in [13]. For the utilised metal insulator semiconductor (MIS) structures, the absence of a pn-junction makes excessive recombination unlikely. The second mechanism

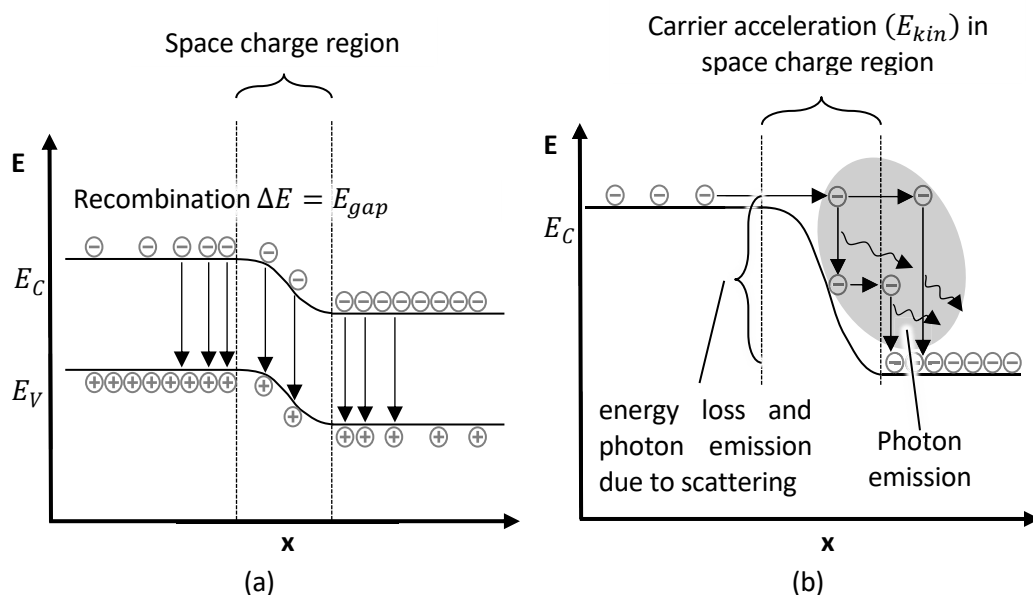


Figure 6: (a) Band diagram of a pn-junction in forward bias; increased recombination due to an increased minority carrier concentration at the boundary of the space charge region and an increased carrier density in the space charge region; (b) Conduction band of a band diagram from a pn-junction in reverse bias; intra-band relaxation processes and resulting photon emission.

## 5. Experimental methods and experiments

that can cause photon emission is shown in Figure 6b. Electrons that are accelerated in an electrical field, are subject to scattering with the atomic lattice or relaxation after leaving the electrical field. The kinetic energy that the accelerated electrons absorb within the electrical field is released during the scattering or relaxation. This loss of energy can lead to the generation of a photon. Whereas Figure 6b shows the field-accelerated photon emission exemplary for a pn-junction in reverse bias, the principle of operation is the same for structures without a pn-junction, but with high electric fields, e.g. a MOS transistor in saturation or a MIS structure.

### 5.2.2 Setup

A schematic setup for measuring the photon emission from a semiconductor device is shown in Figure 7. The DUT is electrically driven by an external unit to bring the device into a condition in which photon emission is expected. An optical system is used to collect the emitted photons and to deflect them onto a photon sensitive 2D detector. The optical system features a high numerical aperture lens to maximise the number of photons collected, a lens tube optimised for a dedicated wavelength regime to minimize losses and ensure a good optical projection onto the 2D photon detector. In addition to the photon emission detection system, it is possible to illuminate the DUT with an additional light source and measure a reflection image. Thus, the photon emission measurement can be superimposed with a reflection image in order to enable an accurate localisation of the photon emission measurement in relation to the chip layout. A generic photon emission measurement from a hard breakdown on a metal insulator semiconductor test structure

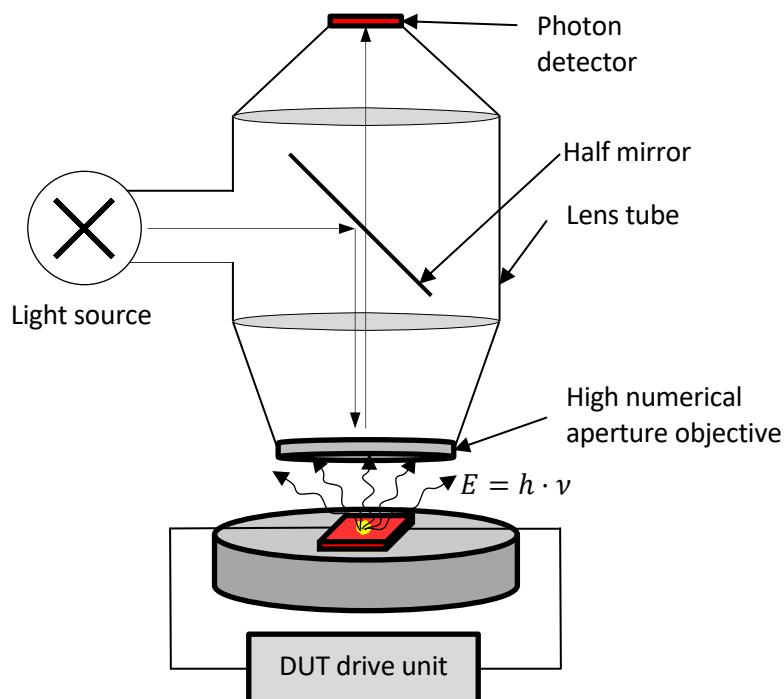


Figure 7: Schematic drawing of a photon emission measurement setup with the possibility to acquire a reflection image

can be seen in Figure 8. Additionally, a superimposed image of the reflection image and the photon emission image is shown.

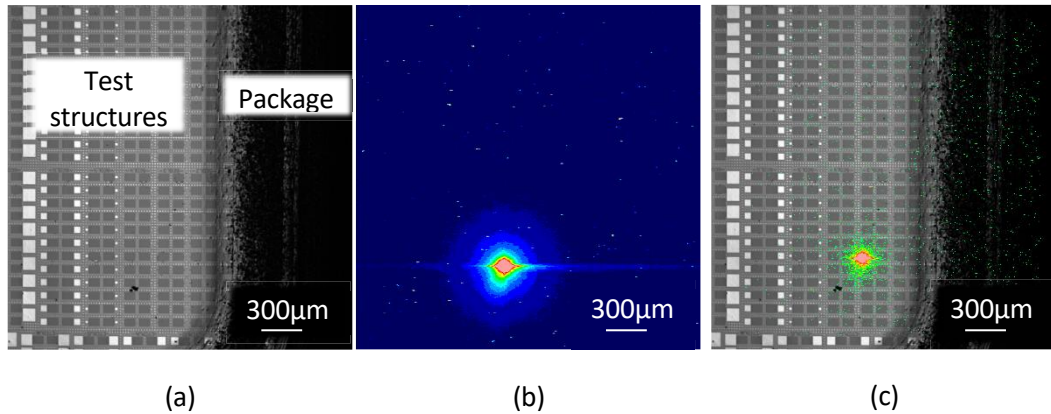


Figure 8: (a) reflection image of a generic test structure; (b) generic photon emission measurement image; (c) superimposition of the reflection image and photon emission measurement

### 5.2.3 Detectors

Over the decades of photon emission measurements, several photon emission detectors have been developed. The silicon CCD has long been the standard detector. However, its spectral sensitivity for a wavelength's domain from 300nm to 1000nm favours front side measurements only. With an increasing number of metal layers, though, shadowing effects made the measurement of the front more and more complicated. On the other hand, back side measurements suffer from enormous photon absorption for wavelengths below 1000nm. The absorption within the bulk silicon is strongly related to the doping of the bulk

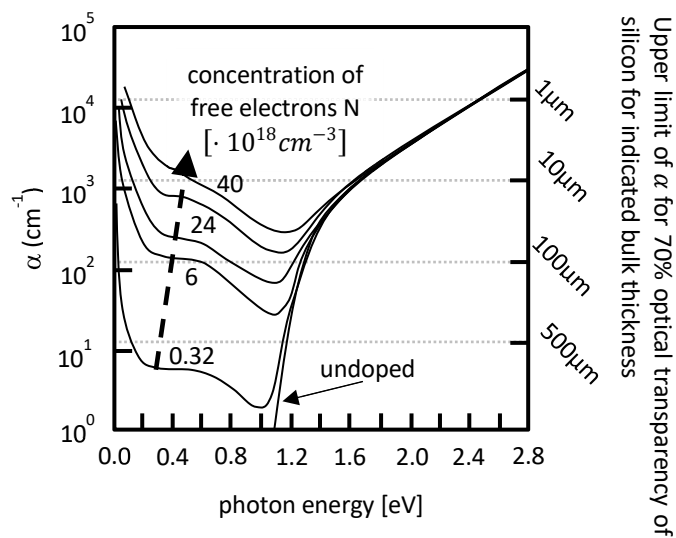


Figure 9: Photon energy related silicon absorption coefficient for different doping concentrations

## 5. Experimental methods and experiments

material as well as the bulk thickness. Soref et al. [14] analysed this relationship experimentally. Absorption increases with raising doping concentration (Figure 9). Thus, if one would like to maintain a low back side absorption for a given photon energy e.g. to extract photons through the back of the chip, it is required thinning of the bulk silicon with respect to an increasing doping concentration. A great deal of effort has recently been put into thinning the bulk silicon to less than  $1\mu\text{m}$  remaining thickness to reduce the effect of the bulk absorption. Thus, it was possible to measure photon emission in the visible spectral range [15]. However, it turned out that the extreme thinning of the bulk silicon is associated with mechanical problems that require special tools and know-how. An alternative detector that can measure in a spectral range that does not require thinning of the bulk silicon is based on Indium-Gallium-Arsenide (InGaAs). With a spectral sensitivity ranging from 900nm to 1700nm, detection in the infrared range is possible, where silicon shows a high transmittivity. Furthermore, there is a relatively new detector is based on mercury-cadmium-telluride (MCT). Its spectral sensitivity ranges from 800nm up 2500nm. In the course of this research, a Si-CCD and an InGaAs detector were available for the planned analysis. A summary of the spectral sensitivity of the various detectors as well as the absorption for different bulk silicon thicknesses is given in Figure 10 [16].

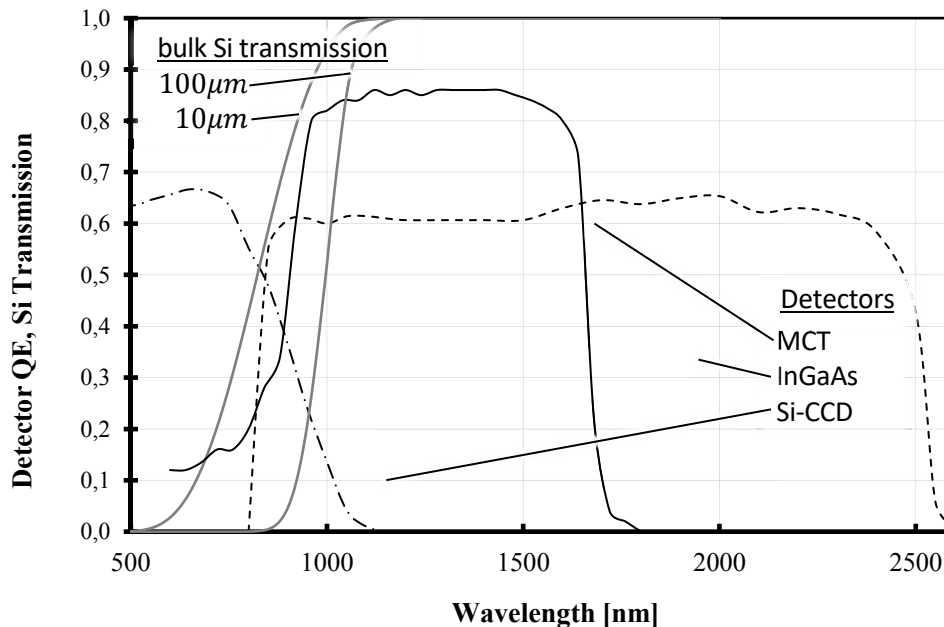


Figure 10: Spectral sensitivity of photon emission microscopy detectors and wavelength dependent silicon transmission for  $10\mu\text{m}$  and  $100\mu\text{m}$  silicon thickness

Next, the advantages and limitations of the two available detectors are discussed in general, but also the consequences for the planned measurements are shown. Measurements from the front generally suffer from shadowing effects due to the metal in the back end of line. The analysed metal-insulator-semiconductor structures are no exception to shadowing effects. For an exact localisation of a defect underneath a metal line or plate, it is therefore required to measure from the back of the chip. Figure 10 shows that the InGaAs detector is favourable for back side measurements as it does not require a costly and risky sample thinning to match its spectral sensitivity with the transmissivity of silicon. However, the longer detectable wavelengths are exchanged for an increasing generation of internal noise. The spectral sensitivity of a detector is mainly characterised by the material band gap. As a

rule of thumb, it can be stated that a narrow band gap can detect longer wavelengths. On the downside, the narrow band gap results in an increased generation of internal thermal noise due to the intrinsic charge carrier generation. An effective means of reducing the thermal noise generation is to cool the detector. Peltier cooling with an active or passive vacuum for thermal insulation of the detector is a common cooling method. Thus the available silicon CCD was cooled to  $-50^{\circ}\text{C}$  and the InGaAs detector to  $-70^{\circ}\text{C}$ . A direct comparison of the noise characteristics from both detectors is shown in Figure 11. In order to measure the noise characteristics, measurements without a DUT were evaluated for different integration times. The calculation of the standard deviation from the noise image is used to characterise the noise. It is shown that the noise generation for the InGaAs detector is higher compared to the Si-CCD. Whereas the noise level from the Si-CCD increases only slightly with increasing integration time, a sweet spot around 100s can be identified for the InGaAs detector. After an integration time of 100s, the noise characteristics of the InGaAs detector increases significantly. According to the limitations due to the noise characteristics, the sensitivity of Si-CCD detectors with extended integration times can be improved. Whereas the InGaAs detector is limited to a maximum integration time caused by the internal noise generation.

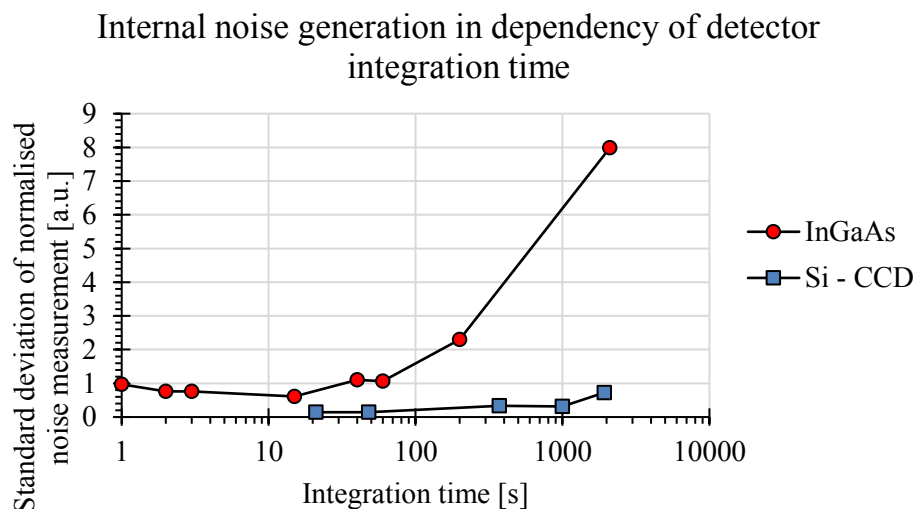


Figure 11: Comparison of internal noise generation characteristics of an InGaAs and Si-CCD photon detector

Concluding, a silicon CCD is limited in its spectral sensitivity range, but its low internal noise generation allows the selection of nearly arbitrary integration times in order to increase its detection sensitivity. This is especially beneficial if a low signal intensity is expected. The InGaAs detector enables measurement through the unthinned chip back side without signal absorption. On the other hand, its detection sensitivity is limited due to the internal generation of noise, which constantly reduces the available dynamic range of the detector. Thus, an integration time of 100s seems to be a sweet spot for the available InGaAs detector.

#### 5.2.4 Optical resolution

In the previous chapter the possibilities and limitations of different photon emission detectors for the detection of a defect were discussed. However, accurate defect

## 5. Experimental methods and experiments

localisation also requires an optical resolution good enough to locate the detected defect. A standard method to determine the optical resolution of a system is the Rayleigh criterion, which is written in Equation 1.

$$x_{min} = 0.61 \frac{\lambda}{NA}$$

**Equation 1: Minimum distance ( $x_{min}$ ) to resolve two distinct light sources according to Rayleigh (Rayleigh criterion).  $\lambda$  is the considered wavelength, NA is the numerical aperture of the optical objective used.**

The minimum distance  $x_{min}$  that can be optically resolved is mainly limited by the numerical aperture (NA) of the objective used and the wavelength ( $\lambda$ ) under consideration. Various optical objectives are available for the system used, including a high NA lens with 50x magnification and a NA of 0.71. The determination of the measured wavelength for photon emission measurements is not straightforward. In most cases, the photon emission consists of different wavelengths. Thus, the operated detector determines the resolution limiting wavelength domain. This concludes that the silicon CCD detector has an advantage over the InGaAs detector in terms of optical resolution. However, Rayleigh defines the determination of two illumination sources. For the experiments planned in the framework of this thesis, however, a single defect development is assumed in a first step. The resolution is therefore mainly limited by the pixel resolution. For calculation of the pixel resolution, the displayed field of view is divided by the detector's pixel size. The field of view is specified and defined for the available combinations of microscope optics and detector. Thus, for the 20x magnification lens the pixel resolution is 641nm/px for the InGaAs detector and 581nm/px for the Si – CCD. For the 50x lens, a pixel resolution of 253nm/px can be assumed for the InGaAs detector; it was not calculated for the Si-CCD. Chapter 6.1 shows that the favourable test structure size is 2 $\mu$ m x 2 $\mu$ m. For the evaluation of a minimum detection sensitivity, however, it must be considered that the optimal results can be achieved if the amount of collected photons is maximised and all photons are projected onto one detector pixel.

### 5.2.5 Solid Immersion Lens

A popular way to increase the optical resolution of a system is the application of a solid immersion lens (SIL). This improves the effective numerical aperture of the system. A solid immersion lens reduces the optical refraction on the surface of the back of the chip. At best, a hemispherical shape of the same material as the bulk material placed on the back of the chip above the point of interest can completely neglect the optical refraction caused by the index of refraction differences of the sample material and the air. Figure 12 shows a schematic drawing of the effect of a solid immersion lens. Eliminating refraction at the silicon-air interface increases the number of photons that can reach the detector. This has two implications: First, for reflection image measurements, this results in an increased optical resolution as well as a magnification by a factor of approximately 2.4. Second, the amount of collected photons is increased for photon emission measurements. This leads to an improved sensitivity. A more detailed description of the advantages, limitations and risks of a solid immersion lens can be found in [17].

A SIL that is made of silicon is optically opaque for visible wavelengths. An alternative SIL material is gallium phosphide, which is transparent for visible wavelengths. Even though the

improvement factor is slightly reduced, it offers the possibility to perform measurements in the optical wavelength regime and increases the sensitivity of a silicon CCD. [15]

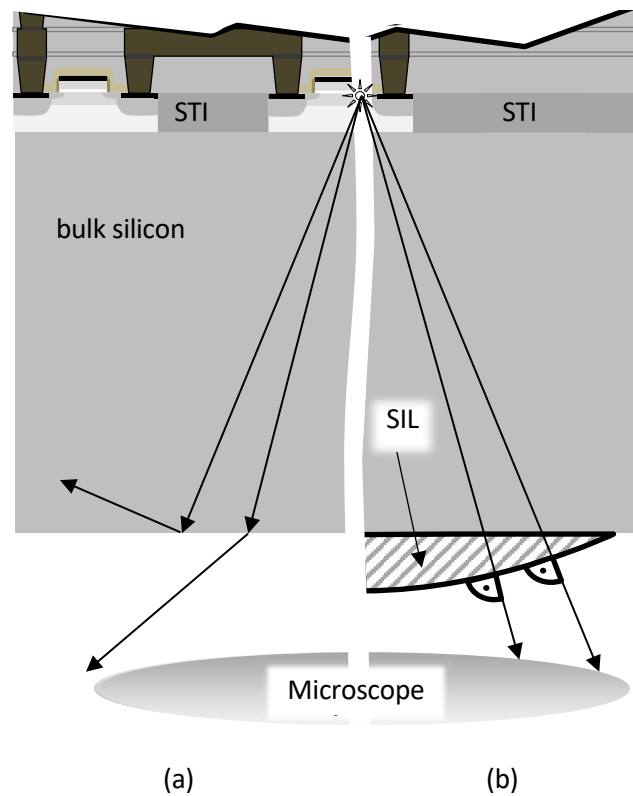


Figure 12: Back side photon emission (a) without SIL, refraction and total reflection at the silicon surface occurs (b) with SIL refraction and total reflection is prevented.

### 5.2.6 Experiments

The main goal of this thesis is the development of a localisation technique, which can detect and localise a soft breakdown defect. It is therefore desirable to locate the lowest possible level of degradation. Low current levels, associated with a soft breakdown suggest weak photon emission signals. Consequently, possibilities must be found to increase the sensitivity of the measurement. Especially when keeping in mind that the localisation of the soft breakdown is aimed at a better understanding of the defect development process, the detection of the lowest possible degradation levels is favourable.

There are two main options to increase the sensitivity of photon emission measurements. The properties of the detector operated are important in order to design the experiment. Another important tuning parameter is the effective numerical aperture. This is fundamentally based on the optical objective used and can be further improved by using a solid immersion lens. Different variations of the measurement parameter as well as optimisations of the measurement setup for photon emission measurements with a silicon CCD and an InGaAs detector are carried out in order to find optimal measurement

## *5. Experimental methods and experiments*

conditions and sensitivity limits for the localisation of soft breakdown defects. This localisation is a prerequisite for planning further analysis, e.g. physical analysis and spectral photon emission measurements for a better understanding of the process of soft breakdown development.

### 5.3 Spectral Photon Emission

#### 5.3.1 Basics

Spectral photon emission microscopy (SPEM) is a method for failure characterisation that can be affiliated to measurements of photon emission microscopy (PEM). Whereas the defect must be localised using PEM, subsequent SPEM measurements give an insight into the characteristics of the source of the photon emission.

There are two ways to measure the spectral composition of a photon emission signal. First, various optical band pass filters can be inserted into the optical path during PEM measurements. The reconstruction of the emitted spectra can be performed from such a set of measurements. Using different filters to measure an entire photon emission spectrum is time consuming and it must be ensured that the spectra do not change during the different measurements. This method is therefore not suitable for characterising defects from permanently degrading defects. Second, the spectral information can be measured in a single measurement by inserting a prism into the optical path. The analysed photon emission signal is based on a wavelength-dependent dispersion within the prism. This adds a spatial component to the measurement from which the spectral data can be extracted. Ideally, the photon emission measured during PEM measurement was projected into one pixel of the photon detector used. In such a case, the prism will add only one spatial component related to the spectral distribution of the photon emission. Whereas the emitted power of a PEM measurement and its corresponding SPEM measurement is constant, the SPEM signal is spatially spread out and thus the sensitivity is reduced.

#### 5.3.2 Setup

The SPEM measurements performed for this thesis were carried out with a prism. The prism is inserted into the existing PEM system PHEMOS 1000. Figure 13 shows a schematic drawing of multiple prisms, which spreads the spectral parts of a prism dispersion beam in parallel. However, enabling SPEM measurements requires careful calibration and preparation of the system.

The dispersion characteristics of the prism are determined using a set of optical band pass filters in combination with a broadband light source. A dedicated pixel shift for wavelength characterisation can be defined and is shown in Figure 14. A highly stable light source with

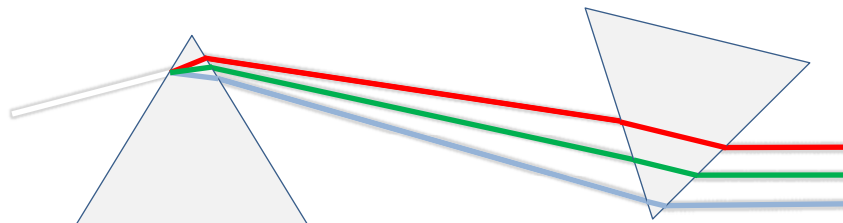
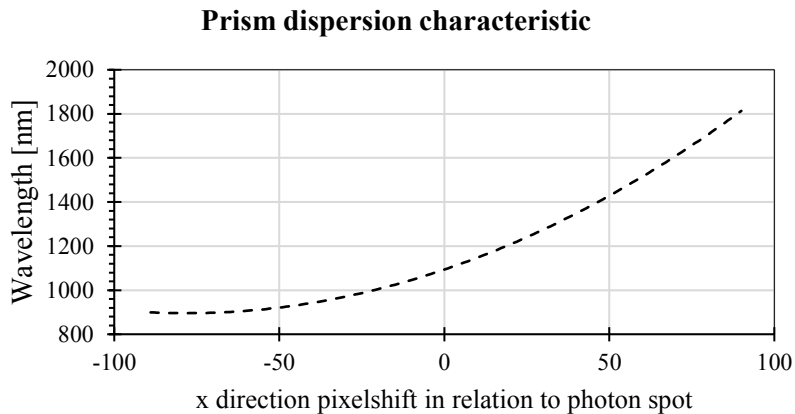


Figure 13: Schematic drawing of the dispersion on a prism

## 5. Experimental methods and experiments



**Figure 14: Dispersion characteristics of the prism used to measure the spectral photon emission from the back of the chip**

a known spectrum must be used in order to determine the correction coefficients for the different objectives available with respect to different wavelengths. The correction coefficients for the available lenses (5x, 20x, 50x, and Solid Immersion Lens) are shown in Figure 15. The 5x, 20x and 50x lens show similar behavioural characteristics. A reliable statement can be expected from a spectral range from 950nm to 1600nm. Effects associated with the detector characteristics result in a significant increase in the correction factors above and below this wavelength range. The solid immersion lens can be evaluated in a spectral range from 1050nm up to 1600nm. This is caused by the additional absorption within the silicon immersion lens that cannot be circumvented. In addition, the absorption within the bulk silicon must be corrected. The wavelength-dependent absorption with respect to the bulk silicon thickness is well known from the literature.

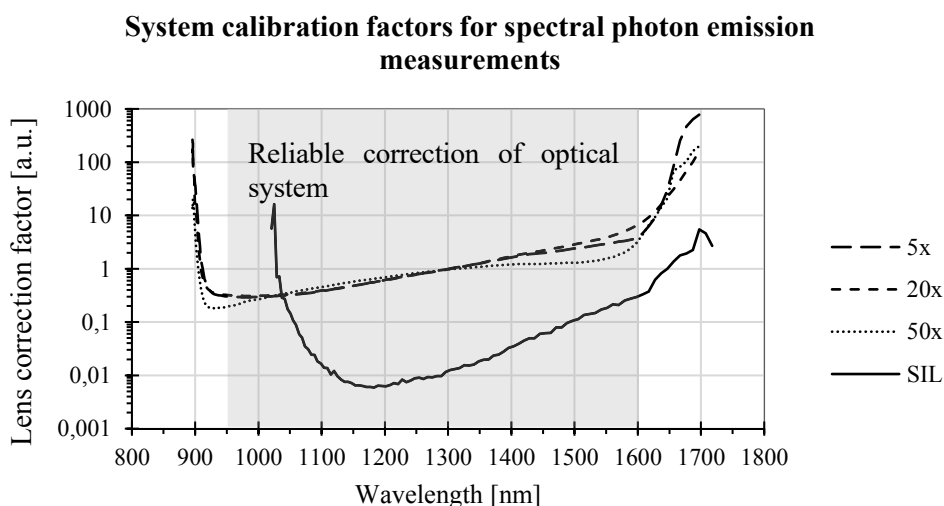


**Figure 15: Lens calibration factors for the spectral photon emission system used; factors determined from a calibration light source. Factors for different lenses are not comparable**

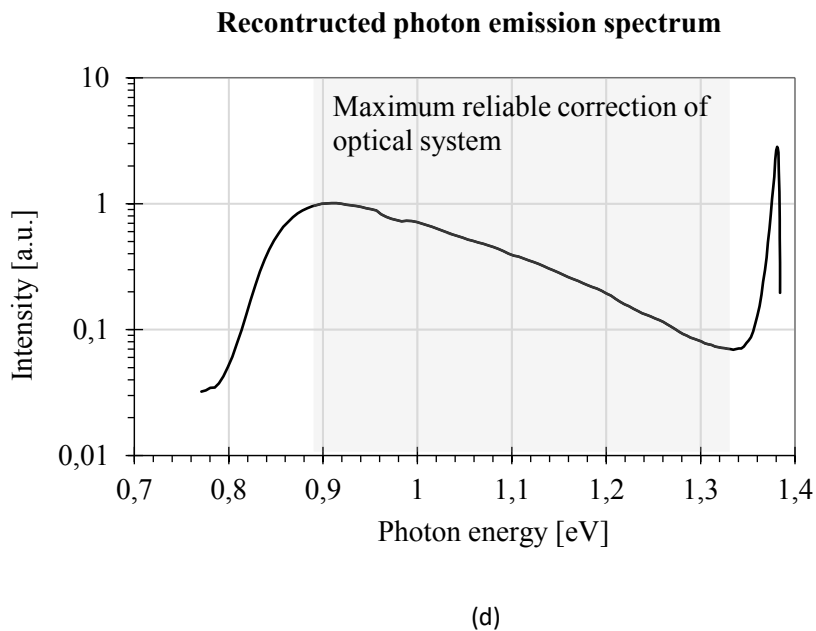
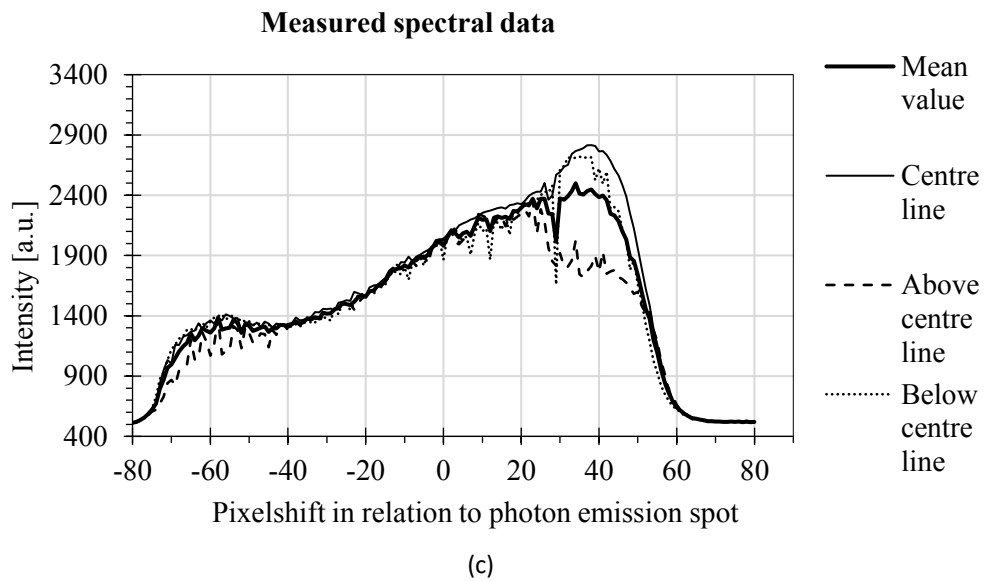


**Figure 16: Exemplary reconstruction of a photon emission spectrum: (a) image of the measured photon emission spot; (b) image of the measured photon emission with prism inserted into the optical path; (c) plotted spectral data; (d) photon emission spectrum**

## *5. Experimental methods and experiments*

Figure 16 shows the way to measure a photon emission spectrum. The basis is the photon emission spot, which is preferably of small expanse with a high signal intensity. Next, the prism is put into the optical path spreading the photon emission into one direction. Figure 16b shows that the spatial expansion of the spectral data runs in x-direction, but a minor spread into y-direction can also be observed. The non-singular photon emission spot and misalignment of the prism are the reasons for this undesirable phenomenon. In order not to lose any spectral information, it is necessary to evaluate more than one spectral line, as shown in Figure 16c. In the example presented, three adjacent spectral lines are evaluated; the mean value is then calculated. Finally, the determined dispersion relation, the correction factors of the optical system and the correction of the bulk silicon absorption are applied to obtain the emitted photon emission spectrum as shown in Figure 16d.

### 5.3.3 Information obtained from spectral characteristics

The spectral distribution of a photon emission gives a deeper insight into the physics that causes the analysed photon emission. Chapter 5.2.1 presented various mechanisms that can cause photon emission. These different photon emission mechanisms show characteristic photon emission spectra. Whereas the recombination based photon emission (R-PE) is limited to a spectral range centred around the band gap energy ( $E_g$ ). The spectral range of photon emission caused by scattering due to the carrier acceleration within an electrical field (F-PE), is continuous. The intensity of the F-PE photon emission exponentially decreases with increasing photon energy. The formal description of an F-PE spectrum is given in Equation 2 [12].

$$I = I_0 e^{-\frac{|E_{ph}|}{k_B T_e}}$$

Equation 2: Spectral distribution of an F - PE

In this equation, the parameter  $T_e$  is the electron temperature, which represents the increased kinetic energy that the charge carriers absorb by passing through the electric field. Thus,  $T_e$  can be used to monitor changing field properties within a range of photon emission. Figure 17 shows the characteristic spectral distribution of R-PE and F-PE as well as the influence of  $T_e$  to the F-PE spectrum.

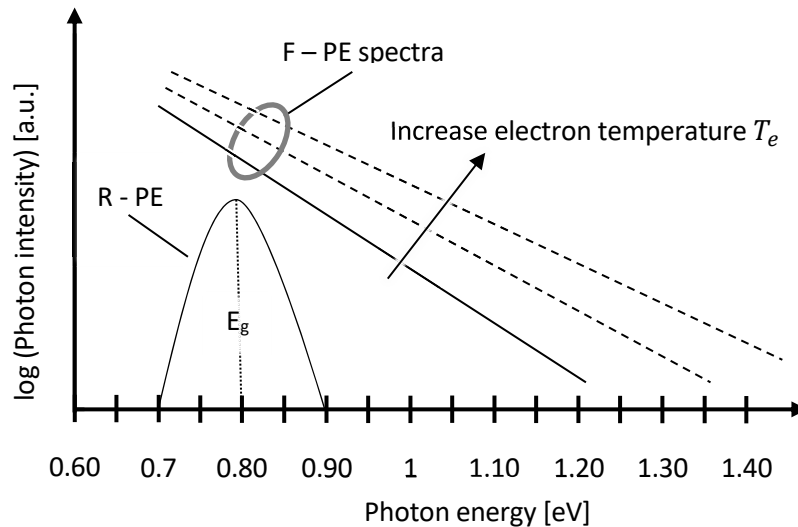
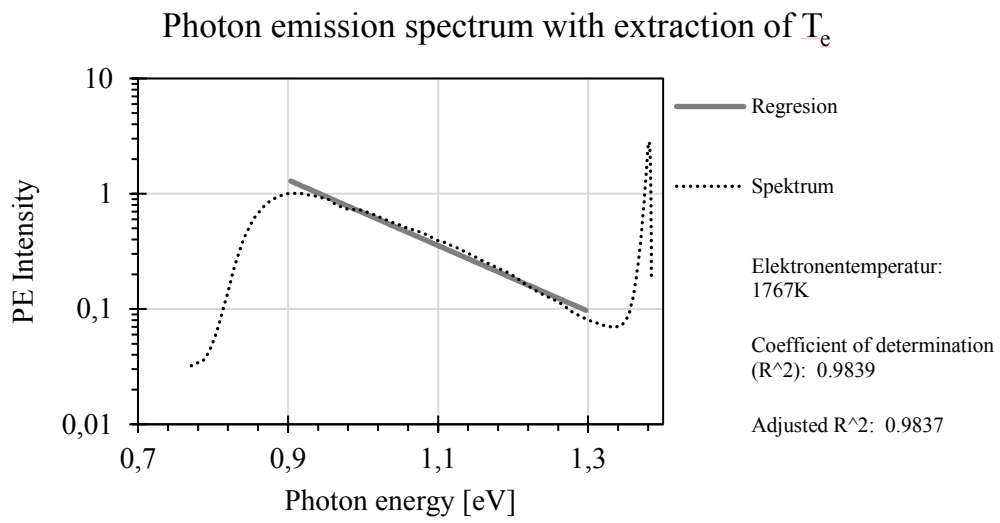


Figure 17: Characteristic spectral distribution of recombination based photon emission (R - PE) and electrical field supported photon emission (F-PE)

In order to extract the parameter  $T_e$  from a measured photon emission spectrum, it is necessary to fit a linear function into the logarithmically plotted spectrum. The slope of this linear function is " $-1/(k_B T_e)$ " from which the electron temperature can easily be extracted. However, spectral measurements are subject of a variety of failure causes. Identifying the correct focus level significantly affects the result of SPEM measurements. Due to that reason, this thesis recommends providing a goodness of fit factor to an extracted electron temperature. For this thesis, the coefficient of determination as well as

## 5. Experimental methods and experiments

the adjusted coefficient of determination are used to qualify the quality of the extracted electron temperature. A fully extracted photon emission spectrum can be seen in Figure 18.



**Figure 18: Generic fully evaluated photon emission spectra with extracted electron temperature and specification of goodness of fit**

## 5.4 Electro optical frequency mapping

Electro optical frequency mapping (EOFM) is a failure analysis method sensitive to changes in the optical properties of the analysed device. By stimulating the device under test with electrical signals, it is possible to modify the optical properties of the silicon underneath. These changes in the optical properties can modulate a passing laser beam in its amplitude, phase and frequency. The evaluation of the reflected and modulated laser beam generates an EOFM signal. The EOFM signal allows determining different device parameters and operation modes.

### 5.4.1 Basics

In order to understand the functional principles of EOFM, it is important to know the traits that can influence the optical properties of a silicon device. The optical properties of the analysed materials can be divided into two categories: voltage-independent and voltage-dependent attributes. The voltage-independent parameters generate a static part of the EOFM signal, e.g. the laser wavelength used for EOFM, the temperature of the device, the strength of the built-in field and the concentration of free carriers caused by the implantation. On the other hand, the voltage-dependent parameters, e.g. the thickness of the space charge region, the effective charge carrier density (inversion, depletion, etc.) and the strength of the external electrical field generate a voltage-dependent change in the optical properties. With a periodically changing electrical input, periodically changing optical properties are created which generate the dynamic part of the EOFM signal.

The voltage-independent parameters must be selected to fit the general requirements of an EOFM measurement. The laser wavelength used, e.g., must not be absorbed within the bulk silicon. The dynamically changing properties generate the actually measured EOFM signal. The effects that are relevant for the experiments performed in the framework of this thesis are presented and discussed below. The discussion mainly follows [18].

#### 5.4.1.1 Free carrier concentration

The free carrier effect describes the change in the refractive index and the absorption coefficient in silicon, depending on the density of free carriers. Equation 3 and Equation 4 show the relative change in the refractive index ( $\Delta n$ ) and the relative change in the absorption coefficient ( $\Delta \alpha$ ) in relation to the relative change in the concentration of free electrons and holes ( $\Delta N_e, \Delta N_h$ ). Whereas  $\lambda$  is the wavelength under consideration,  $q$  is the electron charge,  $c_0$  is the speed of light in vacuum,  $\epsilon$  is the permittivity of free space,  $n_0$  is

$$\Delta n = -\frac{\lambda^2 q^2}{8\pi^2 c_0^2 \epsilon_0 n_0} \left( \frac{\Delta N_e}{m_e} + \frac{\Delta N_h}{m_h} \right) \quad \Delta \alpha = \frac{\lambda^2 q^3}{4\pi^2 c_0^3 \epsilon_0 n_0} \left( \frac{\Delta N_e}{m_e^2 \mu_e} + \frac{\Delta N_h}{m_h^2 \mu_e} \right)$$

Equation 3: Silicon index of refraction

Equation 4: Silicon absorption coefficient

the refractive index of unperturbed c-Si,  $m_e$  and  $m_h$  are the mass of an electron or a hole, respectively. A relative change in electron and hole concentration can be achieved by

## 5. Experimental methods and experiments

applying an external voltage to the device. An example for the modulation of free charge carriers is the capacitance voltage characteristic of a metal insulator semiconductor structure. Here an applied voltage modulates the width of the space charge region or even creates an inversion channel. Both effects modulate the capacitance of a metal insulator semiconductor structure [19]. The results from [20] indicate that the concentration of free carriers is one of the major contributors to the EOFM signal generation for silicon devices. Furthermore, Kindereit in [21] investigated and simulated the strengths of various effects on EOFM signal generation and came to the same conclusion. Among other minor effects, the concentration of free carriers has the highest impact on the EOFM signal generation. Furthermore, the simulations performed in [21] demonstrate that the modulation of the refractive index plays a larger role than the modulation of the absorption coefficient.

### 5.4.1.2 Interference effects (multi-beam interference)

An optical beam that passes multiple layers of different optical properties, in particular a different refractive index, is partially reflected at each material interface. The resulting beam modulation causes interference with the incident laser beam. In [21], a two-beam interference is presented, proving that the beam interference can be calculated and simulated. However, it is also stated that more accurate modelling and calculation of beam interference in an electrically active device would require a multi-beam interference model. In general, it is possible to model a multi-beam interference, but it is also time consuming and complex. In addition, some simplifications, e.g. the thickness of the space charge region, must still be assumed.

### 5.4.1.3 Strength of the electric field

Various effects related to the electrical field may influence the optical properties of a semiconductor. Among others, Franz-Keldysh [22, 23], electro-refraction [14] and the optical Kerr effect [24]. However, even if these effects are present in the analysed structures, they are expected to contribute only a minor part to the overall EOFM signal generation in silicon devices [21, 25]. Therefore, they are not presented in detail in this thesis, but can be examined further in the given references.

## 5.4.2 Setup

Figure 19 shows an EOFM measurement setup. The device under test (DUT) is a metal insulator semiconductor structure. A pulse generator electrically operates the DUT structure at a specific frequency. The EOFM detection system installed at the TU Berlin supports pulse frequencies from 100kHz to 8GHz. The standard setup of the pulse generator was a square wave signal with a 1MHz frequency and a duty cycle of 50%. This frequency is fed into a lock-in amplifier as a reference frequency. At the same time, a laser beam is scanned over the area of interest. The portion of the laser that passes through the bulk silicon will be partially reflected or transmitted at the different material interfaces. The reflected part of the laser light can be detected by a photo diode. The signal of the photo diode detecting the reflected laser signal, is also fed into the lock-in amplifier. The signal

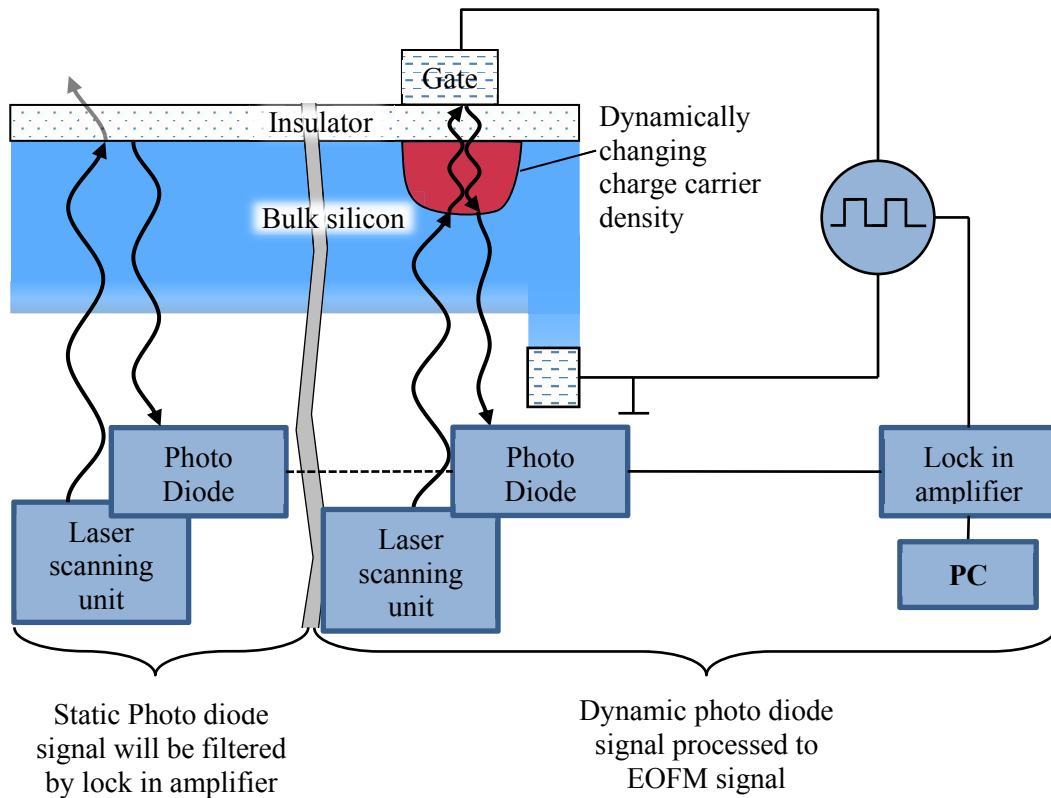


Figure 19: Schematic drawing of an EOFM setup; EOFM signal generation only occurred if the reflected laser beam was dynamically modulated

from the lock-in amplifier is processed into an EOFM image. The portion of light falling on the active areas of the electrically stimulated device is modulated by the electrically induced changes in the optical properties. Reflection signals from the non-electrically active areas will be filtered out by the lock in-amplifier, as they are not modulated with the DUT stimulation frequency. A more detailed description of a lock-in amplifier can be found in [26].

## 5.5 Optical Beam Induced Resistance Change

Optical beam induced resistance change (OBIRCH) is an optical beam base scanning technique, in which a laser beam scans an area of interest and its interaction with the device under tests (DUT) generates a trackable change in the DUT power consumption. The changing power consumption can then be mapped to the laser position, thus generating 2D information. Various conclusions can be drawn from the 2D image of the heat-dependent power consumption.

### 5.5.1 Basics

A laser beam scanning an integrated circuit can either be absorbed, transmitted, or reflected by the different material layers. In most cases of microelectronic failure analysis, a mixture of all three will likely occur. When choosing the correct laser wavelength, a small portion of the incident laser will be absorbed by the electrically active parts of the chip. These areas can be metallic elements, polysilicon elements or highly doped substrate areas. The absorbed beam energy can result in the generation of electron hole pairs or local heating. The use of electron hole pair generation is used for photon laser stimulations (PLS), which will not be discussed here. However, the reader that would like to read further into PLS can take a look at [27]. Local heating, which is generated in the electrical active areas, modifies the electrical properties of the heated medium, namely its resistivity. This change in resistivity can be monitored by the power consumption of the device analysed. The correlation of the power consumption with the position of the laser spot enables a precise localization of thermally sensitive areas. Two different effects can lead to a variation of the power consumption due to the induced heat. First, a developing temperature gradient between different materials can trigger the Seebeck effect. The Seebeck effect is a widely accepted effect, e.g. for temperature measurements with thermocouples[28]. However, the Seebeck effect is not of importance for the experiments performed for this thesis. Further information on the effect and its utilisation for OBIRCH analysis can be found in[29]. Second, the induced heat according to Equation 5 causes a variation in material resistance. Where  $\rho_0$  is the resistivity,  $\alpha_{TCR}$  is the thermal coefficient of resistance, and  $(T-T_0)$  is the heat-induced temperature variation.

$$\Delta\rho = \rho_0\alpha_{TCR}(T - T_0)$$

Equation 5: Heat induced resistance change

The power consumption can be monitored either by applying a constant voltage to the DUT and measuring the change in current or by applying a constant current and measuring the change in voltage. Both variations are formally described in Equation 6 and Equation 7 [29].

$$\Delta V = \Delta R_{DUT} I_{DUT}$$

Equation 6: Heat induced voltage alteration using a constant current source to stimulate the device under test

$$\Delta I = -\left(\frac{\Delta R_{DUT}}{R_{DUT}^2}\right) V_S$$

Equation 7: Heat induced current alteration using a constant voltage source to stimulate the device under test

### 5.5.2 Setup

The commercial implementation of thermal laser stimulation techniques usually takes place as an extension of near infrared laser scanning microscopes. A basic version of an OBIRCH measurement system is usually implemented with a laser wavelength around 1300nm in order to enable back side analysis through the chip bulk silicon. In this wavelength regime, the generation of electron hole pairs is significantly suppressed by the incident laser. Consequently, the absorbed laser energy is mainly transformed into thermal energy, thermally stimulating different parts of the chip. In order to integrate a standard laser scanning microscope into a system which is capable to perform OBIRCH analysis, the following elements must be additionally be integrated: First, the DUT needs to be operated electrically, which can be done by an electrical drive unit. Second, an adequate amplification system is required to measure minimal changes in power consumption. A high bandwidth with adjustable amplification is to be preferred for effective measurements. Third, a signal processing and imaging system is required to map the laser position to the power consumption measurement. Figure 20 shows a possible implementation of an OBIRCH measurement setup into a laser scanning microscope, including methods (A) and (B) in order to monitor the power consumption. In method (A), the thermally induced change in resistance is measured and amplified via the alteration in current, whereas the DUT is operated at a constant voltage. Alternatively, the DUT can be operated with a constant current and the thermally induced change in resistance can be monitored with a voltage measurement as shown in method (B).

5. Experimental methods and experiments

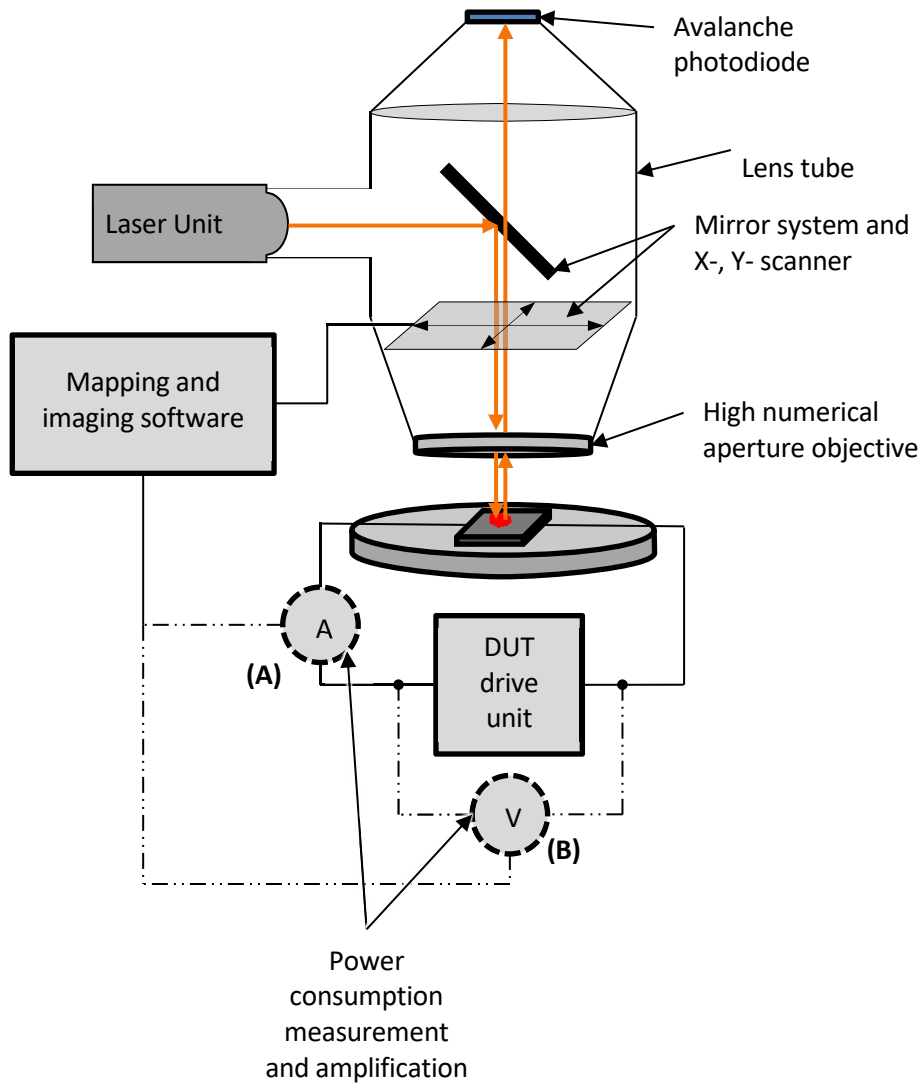


Figure 20: Schematic setup of a laser scanning microscope with extensions for measuring changes in resistance induced by optical beams

### 5.5.3 Measurements

A generic OBIRCH measurement is displayed in Figure 21. Shown is a front side measurement of a buried metal line that was operated electrically. In Figure 21a, the current path can be clearly identified by the black line, whereas the reflection image from Figure 21b does not show any metallic structure at the position of the OBIRCH signal. Only the superimposition of the measured signal and the reflection image shown in Figure 21c reveals the buried metal line. For this measurement, the device under test was operated with a constant voltage. The visualisation of such a low ohmic current path is a standard application of OBIRCH measurements. However, the development of techniques for the localisation of soft breakdown defects is planned within the scope of this thesis. The low leakage current levels associated with a soft breakdown are orders of magnitude lower and the resistance orders of magnitude higher compared to defects for which OBIRCH is commonly used.

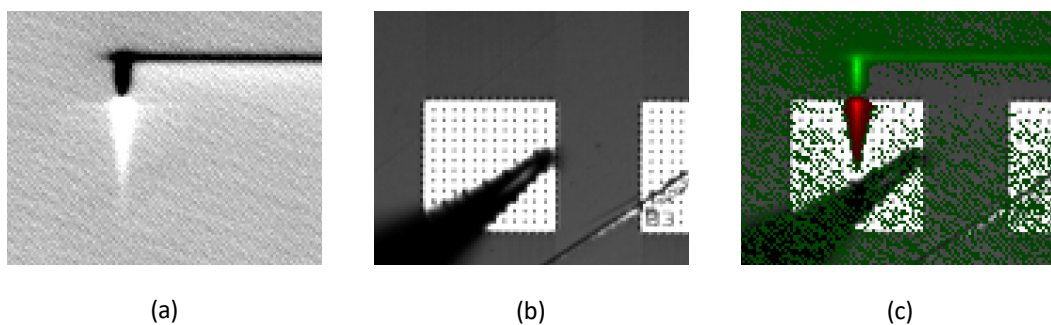


Figure 21: (a) Generic OBIRCH measurement, (b) the corresponding reflection image and (c) the overlay of OBIRCH signal and reflection image

### 5.5.4 Setup variations

During experimental work, it may happen that different sample types require an adjusted setup. An advantage of the available OBIRCH system Phemos-1000, is that the internal electric drive unit and the internal amplification unit can be replaced by external equipment. This enables the flexibility to adjust the hardware to specific use case problems. For this thesis, the Keithley SCS 4200 parameter analyser and the SR560 voltage amplifier had to be implemented into the OBIRCH measurement setup to enable localisation of soft breakdown defects. Both devices are described in chapter 4.1.2 and 4.3.

### 5.5.5 Transferring OBIRCH into the optical near field

In this thesis, the measurement principle of OBIRCH was adapted to other optical scanning techniques. One of the main driving forces to do so, was the ubiquitous need to improve the optical resolution of failure analysis techniques. The development of various scanning probe microscope techniques significantly improved the resolution limits and analysis options of microscopy techniques. Examples of scanning probe techniques are atomic force microscopy (AFM), scanning capacitance microscopy (SCM) and scanning near-field optical

## 5. Experimental methods and experiments

microscopy (SNOM). When it comes to beam based failure analysis techniques like OBIRCH, it seems sensible to evaluate the optically based technique SNOM with regard to its failure analysis capabilities.

### 5.5.5.1 Scanning near field optical microscopy

Near field optical microscopy can archive optical resolutions below the diffraction limit [30]. The basic principle of how SNOM achieves an optical resolution dependent on the aperture rather than being limited by the diffraction limit is shown in Figure 22 [31]. Incident radiation is widely blocked by an optically opaque material. The light can pass through the opaque layer via a small aperture with an opening dimension below the incident wavelength. When the object of interest is brought close to the aperture, the resulting resolution is not limited by the wavelength used, but by the dimension of the aperture. This is the case when the analysed structure is within the optical near field of the light leaving the aperture. Whereas the transition from near-field optics to far-field optics is fluent, it is often assumed that near-field optics are applicable for sample-aperture distances much smaller than the wavelength used [32]. A possible implementation of SNOM configurations uses an optical fibre that is sharpened and coated with aluminium at the end at which the light is to exit the fibre. At the tip of the aluminium-coated fibre, a defined aperture is cut into the aluminium by using a focused ion beam. Therefore, it is possible to vary the aperture size as required.

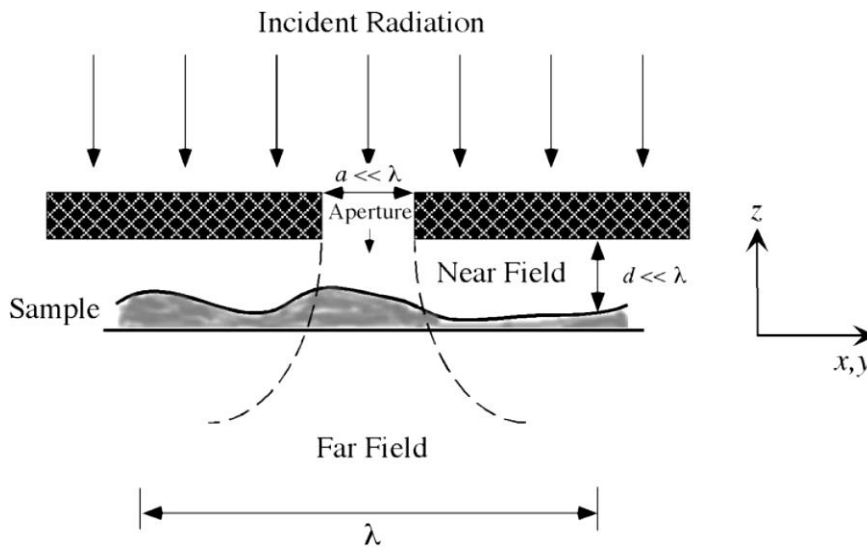


Figure 22: Schematic drawing to illustrate how near field optics can overcome the diffraction limit and thus achieve a sub-wavelength resolution.

A schematic drawing of a possible SNOM setup is shown in Figure 23. The laser light is coupled into an optical fibre that is glued onto a tuning fork. The light leaving the fibre is

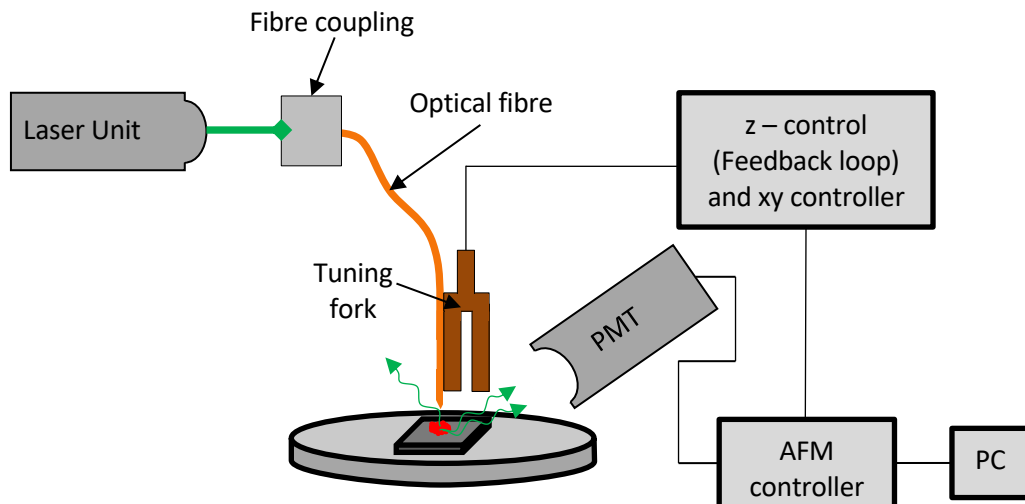


Figure 23: Schematic setup of a scanning near field optical microscopy with a tuning fork to control the height

reflected from the sample surface and collected by a photo multiplier tube (PMT). The signal from the PMT is fed into the AFM, where it is processed. The distance between fibre tip and sample surface is monitored with the tuning fork. The electrically stimulated and thus oscillating tuning fork interacts with the sample surface in such a way that the oscillation amplitude is modulated by the distance to the sample surface. By feeding the oscillation amplitude into a feedback loop, the distance to the sample surface can be kept constant. The same control system that realises z-control, also realises xy scanning of the tuning fork or the fibre tip respectively. Finally, the PMT signal and the xyz information are fed into the AFM controller to map the PMT signal to the position of the tuning fork. Different optical information can be extracted from such SNOM measurements, e.g. a high-resolution reflection image and a topographic map of the scanned area.

#### 5.5.5.2 Implementing OBIRCH into a SNOM system

Adapting the measurement principle of the change in resistance induced by optical beams into an AFM system is not obvious. Most commercially available AFM systems and their derivatives are hermitically sealed in terms of customising the setup. Even measurement parameters can often only be adjusted to a limited degree. However, the tool available from NT-MDT offers a modular setup with extensive customisation options. This includes the possibility of feeding an external voltage into the control system so that the external signal is mapped to the position of the scanning tip. Due to the scanning tip and its spatial extend, the available working space on the DUT surface is limited. Electrical contacting of the sample can therefore be challenging; and individual solutions for different samples must be developed in order to connect the electrical drive and measuring unit to the sample. Furthermore, a lock-in amplifier must be implemented to detect the minimal changes in the DUT's resistance. The implementation of a lock-in amplifier requires the establishment of a chopper in order to modulate the stimulating signal, or the laser respectively. A chopper is a spinning wheel that is placed in the optical path of the laser before it is coupled into the fibre. By blocking the laser or allowing the laser to pass, the coupled laser signal is modulated by a pre-set frequency. With the reference frequency and the measurement

## 5. Experimental methods and experiments

signal from the electric drive and the measuring unit, the lock-in amplifier can monitor the optically induced changes in resistance. These changes are fed into the AFM controller in order to be mapped to the position of the scanning tip. Figure 24 shows the adapted SNOM setup that implements the OBIRCH measurement method. Another important point is the laser power coupled into the fibre as well as the laser wavelength used. The laser available has a wavelength of 532nm and the laser power is 3mW. The laser wavelength available is suitable for measurements on the front as it can be partially absorbed by front side materials, e.g. aluminium. Thus, heat can be generated in the electrically active areas and OBIRCH can be used. On the other hand, measurements from the back would require extreme thinning of the bulk silicon to reach the electrically active areas with the laser injected. The second critical parameter is fibre-coupled laser power. In order to generate a maximum OBIRCH signal, high laser power leaving the SNOM tip is desirable. However, the coupled laser power heats the aluminium coating of the SNOM tip. Too much laser power causes a smoothing of the aluminium and in the worst case the aluminium can melt. The reformation of smoothed or molten aluminium can change the defined aperture size or can create unwanted gaps in the aluminium coating.

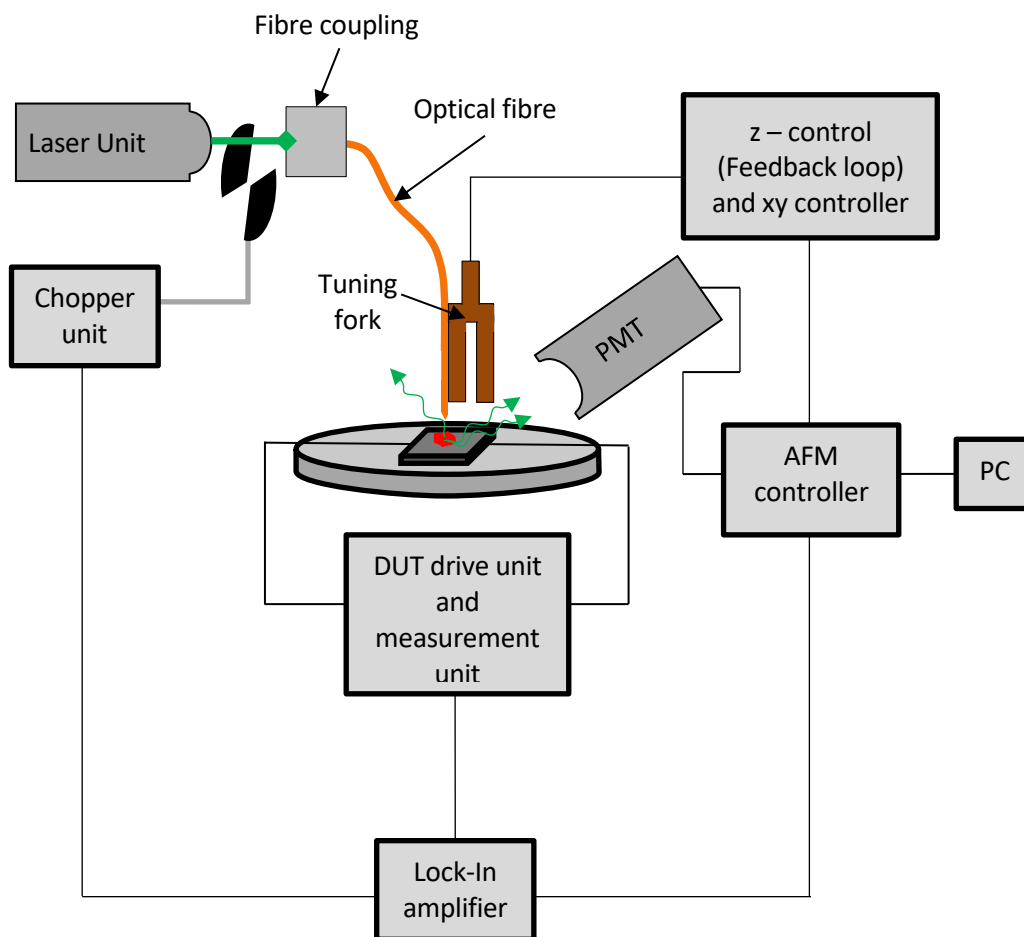


Figure 24: Schematic setup of a scanning near field optical microscopy with a tuning fork to control the height and additional extensions to allow resistance change measurements induced by optical beams.

## 5.6 Destructive failure analysis methods

The analysis of localised failures within the monolithic structure of integrated circuits makes destructive failure analysis methods inevitable. Most failure localisation techniques can provide a 2D positioning of the failure. In order to understand the root cause of the localised failure, a detailed failure analysis is followed subsequently to the defect localisation. Non-invasive analysis techniques such as spectral photon emission, x-ray imaging or ultrasonic analysis provide important information about the defect characteristics. Combined with numerical simulations and defect modelling efforts, the root cause of the defects can be well understood. Without physical evidence of the defect and its morphology, however, uncertainty about the defect characteristics and its cause will remain in most cases. Physical evidence of the defect can only be obtained using high resolution microscopy techniques such as scanning electron microscopy (SEM) or transmission electron microscopy (TEM). These techniques require direct optical access to the defect. Therefore, destructive sample preparation must be used to grant direct optical access to the defect.

### 5.6.1 Destructive sample preparation using a Focused Ion Beam

A focused ion beam System (FIB) is a commonly used tool for manipulating specimens in the micro and nanometre range. An electrically focused ion beam is used to knock atoms out of the sample, locally striping off material from the sample surface. The ability to locally remove material in the sub micrometre range enables a buried point of interest to be exposed, e.g. for further optical inspections. However, the preparation of the sample requires a precise localisation of the point of interest. The localisation of defects due to soft breakdown within a low k dielectric back end of line test structures is discussed in detail in chapters 6.2 and 6.4.

By bombarding the specimen with high energetic ions, a constant flux of charge is exerted on the sample. It must be granted that this additional charge does not accumulate on the sample, otherwise an extraordinary high voltage could build up and result in an electrostatic overstress. This is particularly problematic in capacitive test structures, in which an electrostatic overstress caused by a FIB applied charge would superimpose a controlled defect generated. By connecting the front and back of the capacitive test structure with a ground connection, it can be guaranteed that the FIB applied charge can be dispatched from the critical structure. A second unavoidable effect when creating a cross section with a FIB is the formation of rounded corners on the top of a cutting edge. This is associated with the material removal properties of the ion beam. The milling rate at corners is increased over a flat surface[33]. In order to protect the structure of interest from unwanted material removed by the FIB, a protective layer needs to be deposited. This is usually done directly by the FIB, depositing a carbon or metallic based protection film.

While addressing these two issues of FIB preparation, the defect can be exposed from one side by cutting a cross-section into the specimen, or the defect can be isolated from two sides by preparing a sample lamella.

## 5. Experimental methods and experiments

### 5.6.1.1 Preparing and analysing a cross section

Figure 25 shows a schematic drawing of a dual beam system that combines a FIB column with an electron beam column. The focused ions arriving perpendicular to the sample surface removes the sample material from top to bottom. The electron beam shifted angular can simultaneously visualise the sample cross section. The theoretical basics of electron beam imaging can be read in [34–37]. At this point, a short excerpt of important resolution limitation mechanisms is given.

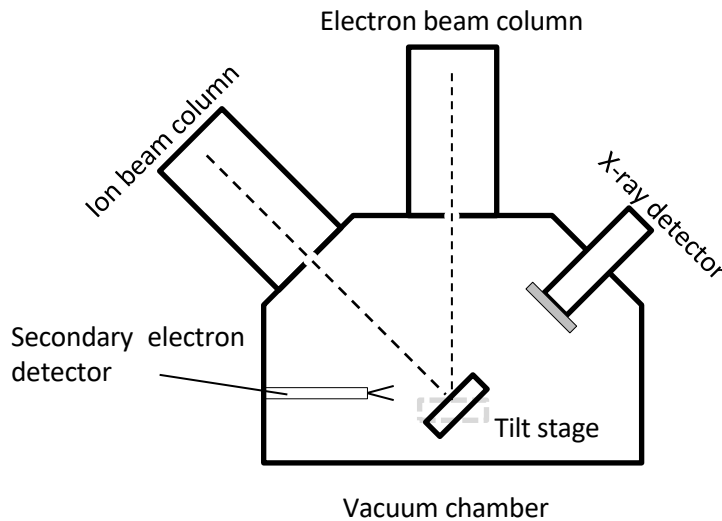


Figure 25: Basic components of a dual beam system

When an electron beam strikes the sample surface, an interaction volume as shown in Figure 26 must be considered for signal generation. Different segments of the interaction volume generate different signals. The sketch shows that secondary electrons escape from the sample close to the surface, thus generating the most topographic sensitive signal. Backscattered electrons produce a higher material contrast as heavier elements generate stronger backscattering, but they also require a larger interaction volume. Even though the

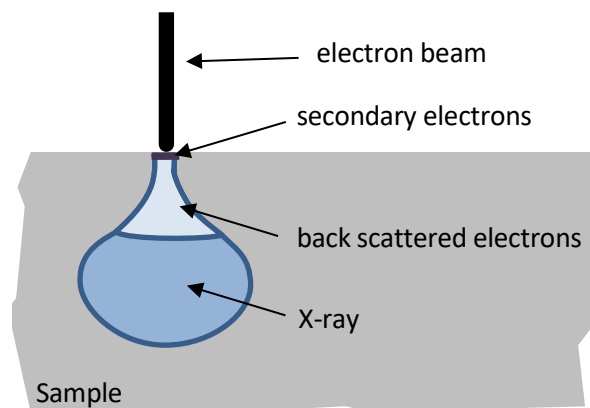


Figure 26: Schematic drawing of the interaction volume generated when an electron beam strikes the sample surface and the generated electrons

size of the interaction volume can be controlled with the accelerating voltage of the electron beam, it cannot be neglected. Consequently, the measured signal is always the result of the summarised information of the stimulated interaction volume, which reduces the available resolution, particularly for material contrast images. However, the possibility to further mill the sample while continuously analysing the cutting edge allows reconstructing a 3D model of the sample analysed. This significantly increases the depth information achieved.

Finally, the continuous implementation of innovative concepts is constantly improving the possibilities as well as the measurable level of detail of electron microscopy systems.

### 5.6.1.2 Preparing and analysing a sample lamella

The creation of a cross section with a FIB reveals the defect from one side. An additional exposure of the defect from the opposing side can be achieved with an additional FIB material removing step. This leaves a thin lamella of the specimen that contains the defect. Further information on sample preparation with a FIB for TEM analysis can be found in [38]. The thin sample lamella can be transferred into a transmission electron microscopy system using a parallel electron beam that is projected onto the thin sample lamella. The formation of the image is achieved by the interaction of the electrons with the sample as the beam is transmitted through the specimen. With this measurement technique, the entire image is measured at once. However, using a convergent electron beam instead of a parallel electron beam modifies the TEM into a scanning TEM (STEM). A selection of advantages of STEM measurements over TEM measurements are briefly presented here. However, a more detailed description of the TEM measurement possibilities and limitations can be found in [39, 40]. Figure 27 shows the imaging principle of TEM and STEM. A STEM uses various detectors with collection angles that may be adjusted depending on which electrons the user wants to capture. The dark field image uses scattered electrons for its imaging whereas the unscattered (transmitted) electrons are blanked and vice versa for the bright field

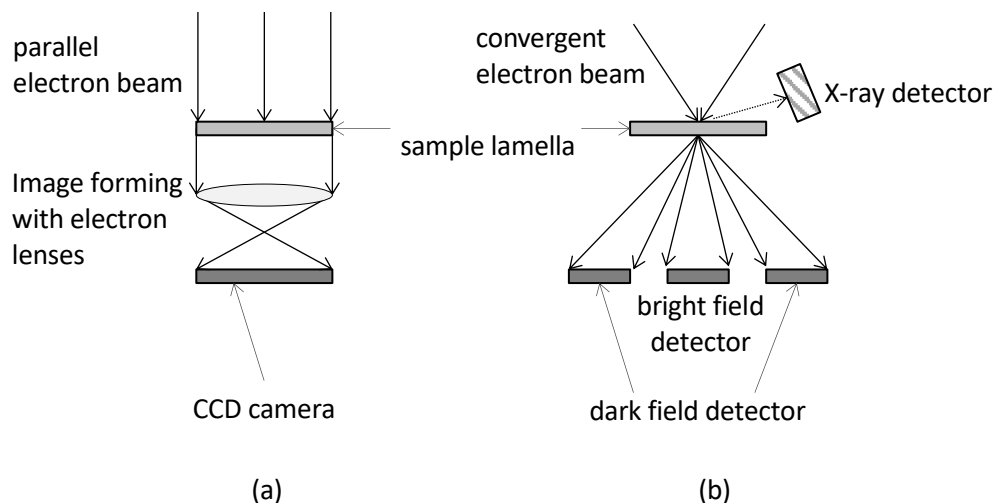


**Figure 27: Schematic drawing of image acquisition in transmission electron microscopy (a) TEM: The entire image is acquired at once; (b) scanning TEM: pointwise measurement of the image enables the use of different detectors to specify the evaluated signal**

## 5. Experimental methods and experiments

imaging. As the scattering is strongly related to the atomic number ( $Z$ ) of the interacting atoms, the dark field and particularly its derivative of the high-angle annular dark-field (HAADF) imaging creates a  $Z$ -contrast image.

### 5.6.1.3 Energy dispersive x-ray spectroscopy

The elemental distribution of a sample can be acquired using the analytical technique of energy dispersive x-ray spectroscopy (EDX). The interaction of the electron beam with the sample atoms can result in an excitation of x-rays. The x-ray energy is material-specific and well known. The excited elements can thus be determined by measuring the energy spectra of the excited x-rays. The spectroscopic and pointwise mapping of the chemical sample composition is essential in order to reconstruct the morphology of defects consisting of different materials. The time consuming STEM - EDX measurement offers the best available spatial resolution for element mapping. However, depending on the sample area as well as the measured elemental concentration, a single measurement can take several hours.

Most commercial scanning electron microscopes (SEM) and STEM systems can optionally be equipped with an EDX detector. Whereas the EDX measurement principle is the same for SEM and STEM systems, the feasible spatial EDX resolution is higher on STEM-EDX measurements. This is mainly due to the fact that STEM samples are thin lamellae, where the interaction volume shown in Figure 26 is limited to the thickness of the sample lamella.

## 6 Results

### 6.1 Electrical characterisation

The development of failure analysis methods for time-dependent signals of low intensity requires characterising the electrical degradation behaviour of the analysed samples. As stated in chapter 5.1 a ramped voltage stress (RVS) analysis provides basic information about the behaviour of sample degradation with short turnaround times.

#### 6.1.1 Ramped voltage stress

Figure 28 shows RVS measurements of the investigated metal insulator semiconductor (MIS) test structures with varying structure sizes. A set of at least 10 measurements for each structure size analysed is summarised in a characteristic I-V curve of the sample size with error bars. The height of the error bars indicates the sample variation. All I-V curves can be divided into three characteristic regions. The lower voltage levels result in leakage currents below 10fA, which vanish in the measurement noise. With increasing stress voltage, the leakage current gradually increases and becomes measurable. The gradually increasing leakage current with continuing stress is the region of soft breakdown (SBD). The following hard breakdown (HBD) can be identified by the nearly vertical current slope, which begins with a 10nA leakage current regardless of the sample size. The critical voltage for driving the structure in HBD decreases with increasing structure size. The structure size correlates with the number of defects included in the test structure. The measurable SBD ranges from 10fA to 10 nA and is divided into two regions with different exponential slopes. Whereas the first region with the higher slope dominates the SBD region with increasing structure size. According to [4], the different slopes are caused by a change of the conduction

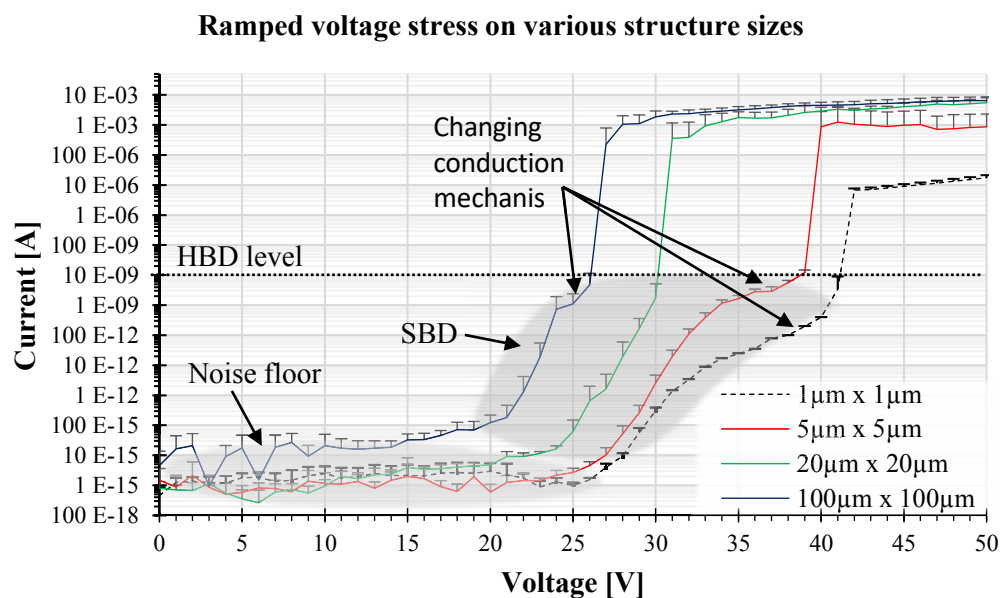


Figure 28: Ramped voltage stress measurements performed on different BEOL MIS test structure sizes. Error bars indicate the sample variation.

## 6. Results

mechanism of the leakage current. However, this study focuses on the development of failure analysis methods and physical analysis of SBD defects rather than on the modelling of defect development based on electrical measurements. Accordingly, it is important to ensure that the conduction mechanism used to develop SBD defect localisation techniques is representative of SBD development under normal operating conditions. Furthermore, predictable degradation is beneficial for the development of dedicated SBD defect localisation techniques. As can be seen from the length of the error bars in Figure 28, the sample variation also increases with increasing structure size. For the development of SBD defect localisation techniques, it is convenient to be able to predict the degradation process of the test sample. Therefore, the low sample variation is preferably used for structure sizes equal or smaller  $5\mu\text{m} \times 5\mu\text{m}$ . The smallest structure size available ( $1\mu\text{m} \times 1\mu\text{m}$ ) shows a limitation of the HBD current to a few ten  $\mu\text{A}$ , which is two orders of magnitude lower than other sample sizes. A current density analysis discussed in chapter 6.1.6.2 shows that the  $1\mu\text{m} \times 1\mu\text{m}$  structures do not fit into a scheme with the other structure sizes. Consequently, further experiments to develop methods for SBD defect failure localisation are performed on test structure sizes of  $2\mu\text{m} \times 2\mu\text{m}$  and  $5\mu\text{m} \times 5\mu\text{m}$ . These structure sizes have been proven to offer reproducible degradation characteristics and are large enough to be easily optically resolved with the available hardware. However, the rapid degradation of the structures during RVS is not suitable for comparable localisation techniques for slow failure.

### 6.1.2 Constant voltage stress

From the RVS measurements shown in Figure 28, a suitable range of operating points for CVS measurements on  $2\mu\text{m} \times 2\mu\text{m}$  and  $5\mu\text{m} \times 5\mu\text{m}$  structures can be identified as 25V - 30V. According to Figure 28, the leakage current for this voltage range ascended just above the measurement noise level, but remains inside the first region of the SBD. This guarantees that the conduction mechanism has not changed yet and the turnaround time is not extended unnecessarily. As can be seen from the black graphs in Figure 29, constant voltage stress levels higher than 30V in accordance with the RVS measurements, result in an inadequate degradation behaviour. The higher initial leakage current compared to CVS measurements with lower stress levels shows that an initial degradation has occurred. Consequently, the structures are quickly driven into HBD. The upper range of the suitable stress levels identified in Figure 28 are voltages from 28V to 30V. This voltage range is represented in Figure 29 with red curves. At these stress levels, the initial leakage current level is reduced, so no initial degradation has occurred. Instead, the leakage current remains at a constant low current level. Such behaviour is typical for the defect nucleation phase of low  $k$  dielectrics under CVS. This phase is followed by the SBD or defect growth region, which is characterised by an exponential growth of the leakage current. The focus of this thesis is the development of methods that can localise defects within the SBD phase. However, an extended SBD region is desirable for the development of these failure localisation techniques to expand the experimental timeframe that enables the SBD detection capabilities of different localisation techniques to be investigated.

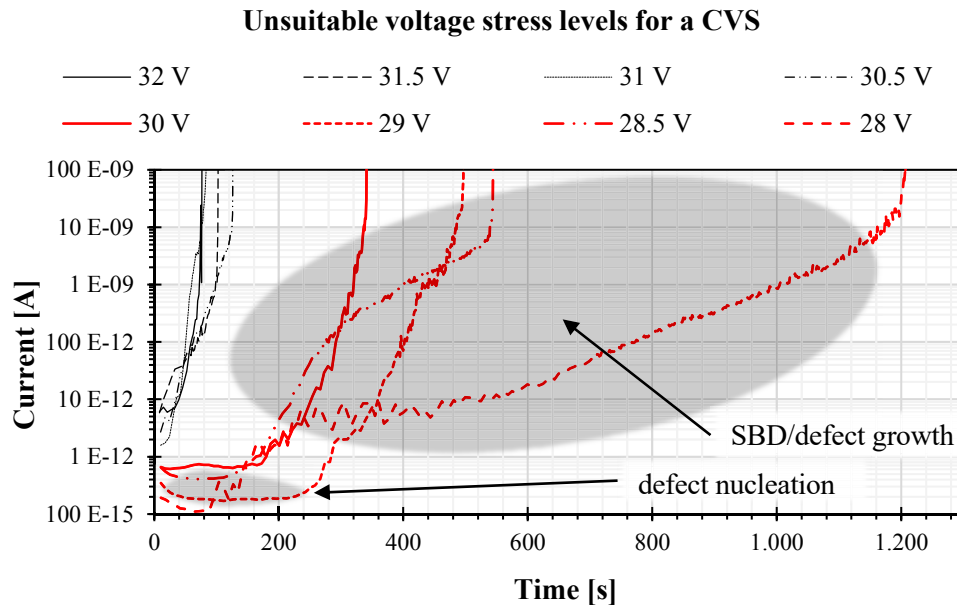


Figure 29: Constant voltage stress measurements on dielectric test structures.

It can be seen in Figure 30 that a further reduced stress level further slows down the degradation process. Thus, the identification of a phase with a negative slope of the leakage current at the beginning of each curve can be identified. This is a characteristic behaviour for a trap charging phase, which is well known from the literature of low  $k$  dielectric degradation. The defect nucleation phase as well as the phase of the SBD are expanded due to the reduced stress level. Various measurements with similar stress levels show that the time until hard breakdown spreads more with a reduced stress level.

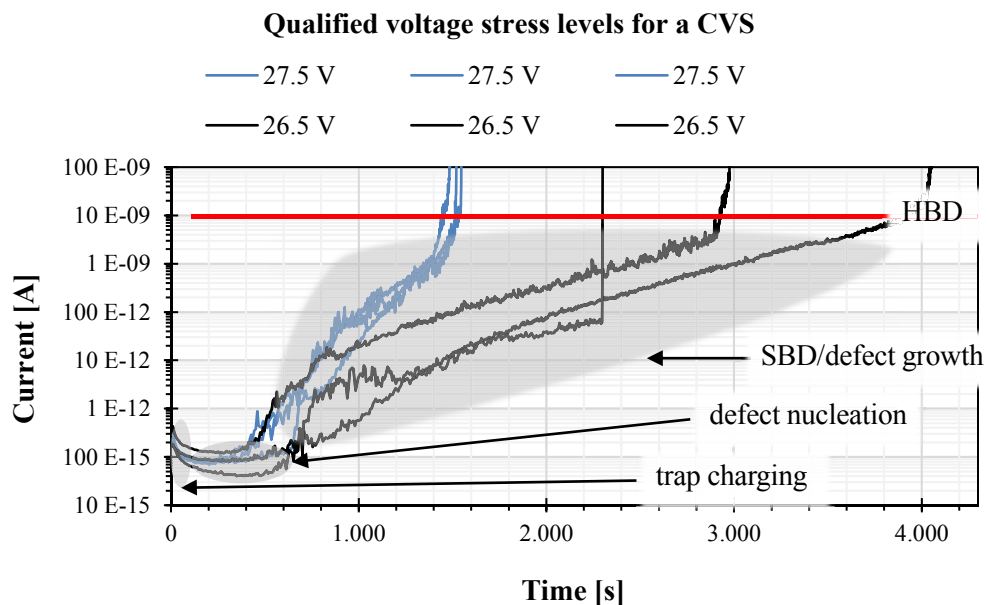


Figure 30: Constant voltage degradation with a reduced voltage stress level to allow an identification of four degradation phases

## 6. Results

Concluding, a voltage stress level less than 28V shows the four classic degradation domains of low k dielectric degradation for the utilised test structures. Starting with a trap charging phase in which material defects within the structure are charged. This reduces the measured leakage current. The next phase is the defect nucleation phase in which the common percolation model states that the defect path builds up slowly, not affecting the leakage current in a measurable range. However, by using an integrated charge sensor instead of measurement tools based on integration and amplification, the measurement sensitivity can be increased significantly. This way it has been shown on other low k materials that the leakage current is not constant during the nucleation phase, but also increases with constant stress [41]. After the nucleation phase, the SBD phase arises, which is characterised by a steady increasing in leakage current. This steady increase in leakage current provides a good opportunity to demonstrate conceptual experiments on SBD localisation techniques. A constantly increasing intensity of the signal response of failure analysis techniques is expected from the constantly increasing leakage current. If the timeframe of failure localisation measurement is chosen wisely, it is possible to cover a wide range of signal intensities with one measurement. As shown in chapter 6.2.1, this type of CVS measurement was used to discover a first ever SBD detection with failure analysis methods. Even though a proof of concept of SBD detection was demonstrated on CVS measurements. The continuous degradation prevents the determination of the degradation level of the detected defect. An accurate determination of the detected defect level is essential not only for the examination of the SBD detection limits of the evaluated failure analysis methods, but also for the quantitative evaluation of planned physical analysis of SBD defects. For this reason, the degradation must be better controlled. The following chapters deal with the development of electrical stress methods that correspond to this purpose.

### 6.1.3 Failure Analysis Stress Methods – Constant-Voltage-Stress with Current-Compliance

In the field of back-end-of-line (BEOL) reliability, electrical characterisation methods aim to extract a lifetime model and other device or material parameters. However, the development and evaluation of failure analysis methods for the localisation of the SBD defects require different stress methods. These methods require better control of the defect degradation. A correlation between the soft breakdown current of BEOL test structures and the injected charge was presented in [42]. This relation is also known from high k material analysis as presented in [43]. However, as the leakage current is formally linked to the flowing charge by  $I = dQ/dt$ , it is possible to calculate the injected charge from an I-t diagram. In order to control the degradation of a stressed low k dielectric it seems promising to limit the charge flow. This chapter evaluates a combination of a constant voltage stress with a current compliance to control the degradation. Figure 31 shows a series of constant voltage stress measurements with a 27.5V stress and a current compliance that varies from 100pA to 1nA for the various samples measured. During the phase of the active current compliance, the stress type changes from CVS to constant current stress (CCS). The current compliances that have been removed after the test structures remained in varying time intervals of 400s to 1900s under CCS. This changes the stress type back to a CVS. It can be seen that the SBD current continuously increases after the current compliances have been removed, which confirms that the structure is still in SBD condition. Without additional current compliance and the same CVS level of 27.5V, the

time to HBD can be estimated to  $\sim 1500$ s (Figure 30). As shown in Figure 31, current compliance can significantly extend the time to HBD by slowing down the degradation. However, the increased SBD current after removal of the current compliance indicates a further degradation during the constant current phase. Whereas no quantitative formulation has been found that describes the relation between the time spent on current compliance and further degradation during this phase, it can be said that limiting the current slows down the degradation.

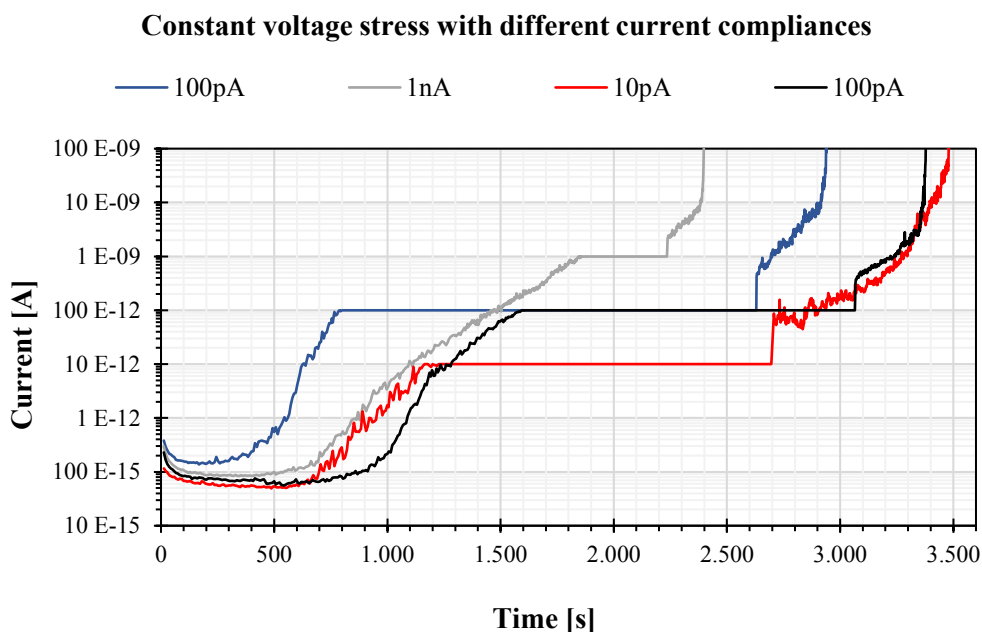


**Figure 31: A series of constant voltage stress measurements with varying levels of current compliance**

A possibility to gain more insight into the sample degradation during the current compliance phase is an analysis of the charge that has been transported through the sample. Figure 32 shows the integration of the charge that has flown through the sample and the corresponding CVS graphs. The defect nucleation phase ends with an accumulated charge of approximately 100pC. During the following SBD phase, the charge accumulates exponentially. Due to the current compliance, the exponential accumulation of charge is reduced to linear growth. On a logarithmic scale, a linearly increasing current can be considered constant when viewed in a short period of time. Thus, the degradation of the structure can be considered as stopped on a short time scale. The removal of the current compliance resumes the exponential charge accumulation, or exponential degradation, respectively. The identification of the HBD is obviously visible as a gap in the C-t diagram.

6. Results

**Constant voltage stress with different current compliances**

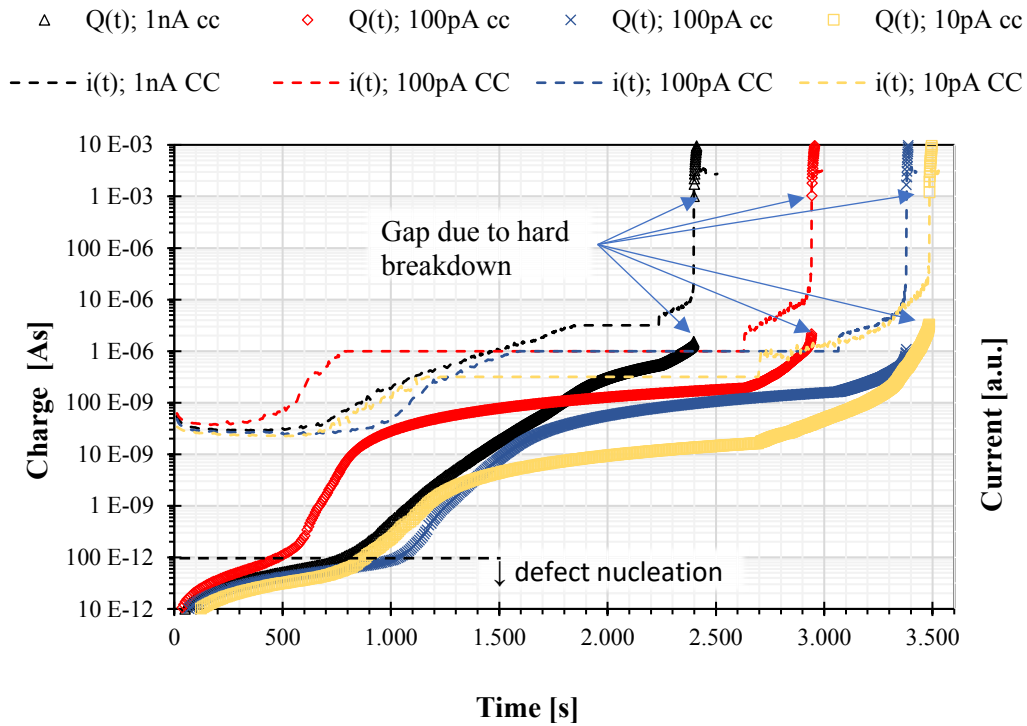


Figure 32: Injected charge during constant voltage stress measurements with current compliance; the related constant voltage stress measurements are marked with dashed lines

Implementing a current compliance into a CVS measurement allows control of degradation. This enables a dedicated analysis of specified states of degradation. The possibility to significantly slow down degradation during this time is a further step in the development of SBD defect localisation techniques. The initial CVS phase ensures a defect development that is based on common sense BEOL stress methods. The following phase of a constant current freezes the degradation at the predefined value and creates an appropriate time window for failure analysis.

#### 6.1.4 Failure Analysis Stress Methods – Ramped-Voltage-Stress with Current-Compliance

The CVS with current compliance method, which is described in the previous chapter, is a suitable technique to effectively control the degradation of dielectric test structures. However, depending on the initial voltage stress level and the current compliance chosen it may take a significant amount of time for the leakage current to increase to the level of the current compliance. A RVS gradually increases the stress voltage, forcing the test structure to degrade faster than a low voltage CVS. Thus, a RVS combined with a current compliance prevents the voltage from rising above a predefined degree of degradation and converts the applied stress mode into a constant current stress. The influence of a temporary change in the stress type into a constant current stress was evaluated in chapter 6.1.3. Figure 33 shows a RVS measurement with a current compliance of 100pA. After only 100s the voltage increased to 32V and the leakage current reached the current compliance of 100pA. This shortens the preceded degradation phase by 8 to 16 times compared to CVS measurements with similar current compliances as shown in Figure 31. However, several reasons indicate that the defect morphology for RVS-generated defects differs from CVS-created defects. First, no defect nucleation phase can be identified during a RVS measurement. Second, the voltage level required to bring the leakage current into current compliance is higher compared to a RVS. A RVS measurement therefore requires 32V to reach a current compliance of 100pA. In chapter 6.1.2 it was shown that a stress voltage of 32V led to initial degradation during CVS measurements. Furthermore, the voltage to maintain the leakage current does not drop significantly during the current compliance. Third, Figure 28 in chapter 6.1.1 shows two different defect mechanisms, identified by two different leakage current slopes during the SBD phase of a RVS measurement. A voltage stress of about 32V is on the verge of changing the degradation mechanism for the analysed  $2\mu\text{m} \times 2\mu\text{m}$  structures. Concluding, the RVS with current compliance measurements is not suitable for creating defects that are used to analyse the intrinsic degradation behaviour. On the other hand, the short turnaround times for the development and improvement of failure localisation techniques enable generating defects of dedicated degradation levels at a reasonable time. The additional current compliance prevents further degradation, thus allowing to focus on the development of failure localisation techniques.

**Ramped voltage stress with current compliance**

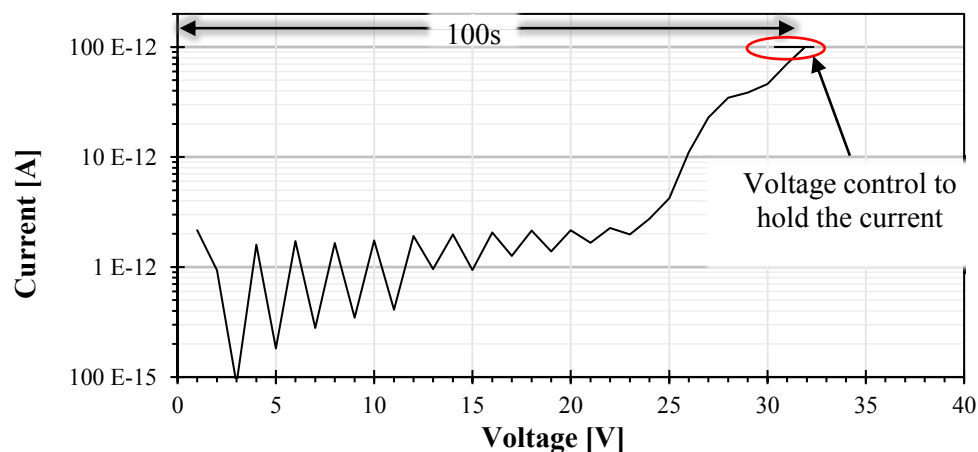


**Figure 33: Ramped voltage stress with a current compliance set to 100pA**

## 6. Results

### 6.1.5 Quantifying the level of degradation

The previous chapters have shown that the limitation of the current is an effective way to control the degradation of dielectric test structures. However, analysis of the injected charge, has also shown that the degradation is continuous during current compliance. Consequently, the determination of the actual level of degradation via the leakage current is no longer suitable. Even though a further degradation is drastically reduced during a constant current stress, it is shown in Figure 32 that the degradation is still progressing. This further degradation can be monitored by measuring the voltage drop across the DUT. The sample resistance can be used to standardise the degradation monitoring during and before the current compliance. Ohm's law links the leakage current, the voltage and the DUT resistance. The graph of resistance over time of the previously shown RVS with current compliance measurement is shown in Figure 34. During the current compliance phase, it is possible to monitor the ongoing degradation. This allows determining the degradation state during the entire measurement. In consensus with the previous results, degradation continues during current compliance, but can be approximated as frozen compared to the non-limited exponentially increasing degradation. Precise monitoring of the degradation level is now possible at any time.

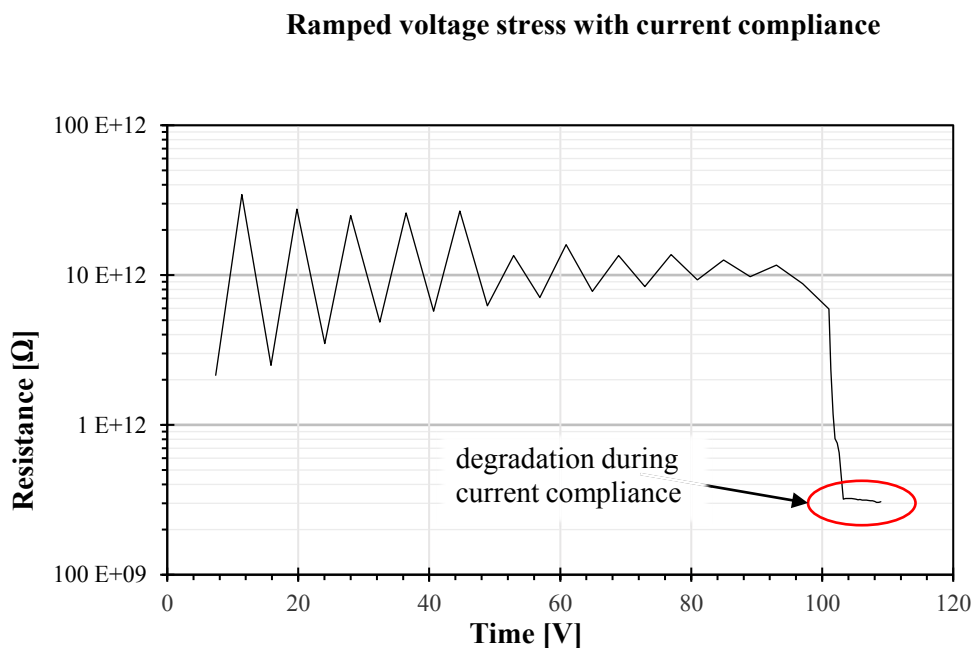


Figure 34: Resistance over time of a ramped voltage stress with a current compliance.

### 6.1.6 Additional results

The chapters 6.1.1 to 6.1.5 have outlined a way to develop specialised electrical stress methods for the development of SBD defect localisation techniques. The following two sub-chapters will present additional effects that have been observed in the electrical characterisation of the analysed structures. However, these effects cannot contribute to the development of failure analysis methods.

### 6.1.6.1 Peculiarities on larger structure sizes

In chapter 6.1.1, it has been shown with RVS measurements that the increased sample variation on larger structure sizes results in a decreased predictability and decreased reproducibility of the degradation procedure. Figure 35 shows a series of CVS measurements on  $100\mu\text{m} \times 100\mu\text{m}$  samples. In a similar approach as described in chapter 6.1.2, a stress voltage of 21.5V can be identified as a suitable CVS level. The defect development is slow enough to display all four characteristic defect regions, the trap-charging phase, the defect nucleation phase, the SBD phase and the HBD. In addition, all four of the graphs shown feature a kind of regeneration effect, which reduces the leakage current during the transition from SBD to HBD. This effect immediately pushes the leakage current down by several orders of magnitude. After the leakage current remains low for a while, a spontaneous HBD finally breaks the structure. Whereas it would be possible to moderate this effect using a current compliance, it is not clear what this regeneration effect is. A possible causality that has been discussed is a kind of self-healing effect. The high thermal energy released during the first HBD attempt melts the developing defective and conductive path, encapsulating the defective area. This effect has only been observed on structures equal or larger than  $100\mu\text{m} \times 100\mu\text{m}$ . Compared to the smaller  $2\mu\text{m} \times 2\mu\text{m}$  structures, the capacity of the  $100\mu\text{m} \times 100\mu\text{m}$  samples is 2500 times larger. During the HBD the charge accumulated on the capacitors is discharged with a current pulse that cannot be measured with a measurement setup based on sampling and holding. Thus, the larger structures provide a larger discharging current, which compared to the smaller  $2\mu\text{m} \times 2\mu\text{m}$  structures is up to 2500 times higher. This could provide additional energy to create a local and time restricted hotspot, which can melt the surrounding material and remove the

**Self-healing effect during constant voltage stress**

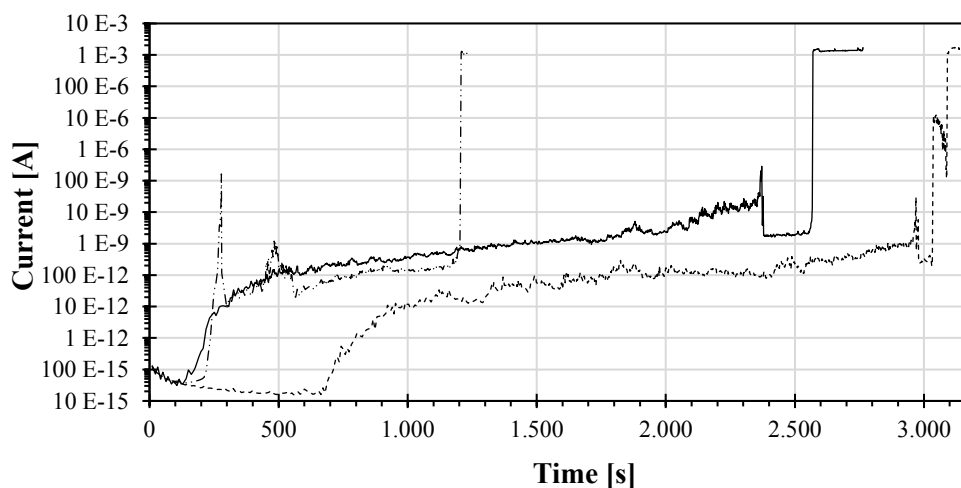


**Figure 35: Selected constant voltage stress measurements with self-healing effect of  $100\mu\text{m} \times 100\mu\text{m}$  back end of line test structures.**

defective path. However, this is only one possibility for this effect. A thorough understanding of the effect origins would require a separate study that cannot be provided in the context of this thesis. The uncertainty of the defect reasons and their effects during a controlled degradation makes this structure size unsuitable for the development of SBD failure

## 6. Results

localisation techniques. On the other hand, this effect shows the necessity of localisations techniques that can detect SBD defects.

### 6.1.6.2 Current density and electrical field strength

A common way to investigate generalised area-independent parameters is to evaluate the current density instead of the absolute measured current. This chapter discusses the possibility of using the current density for the research that was performed for this thesis. Figure 36 shows the same RVS measurements that have been discussed in chapter 6.1.1, but have been rescaled to their corresponding current densities according to their sample sizes. The four structure sizes analysed show a clear trend. The differences in the  $J - V$  characteristics among the different structure sizes indicate that area-dependent effects are involved in the degradation. As the structure size increases, the initial current density decreases, as does the HBD current density. The current density in HBD is affected by the current compliance and is therefore not discussed further here. During the defect nucleation phase, the current density differences are reduced with increasing structure size. The previous chapter has shown a self-healing effect that only occurs on larger structure sizes. So obviously, there is an area dependency on the degradation characteristics. However, with some exceptions, the sensitivity of most failure analysis methods does not depend on the current density of the device. It depends on the current density within the defect, thus the defect size and the absolute current matter. As there is no indication of what size of defect is to be expected, the absolute values of the currents and the device resistance are used to characterise the detection sensitivity limits of the analysed failure analysis methods.

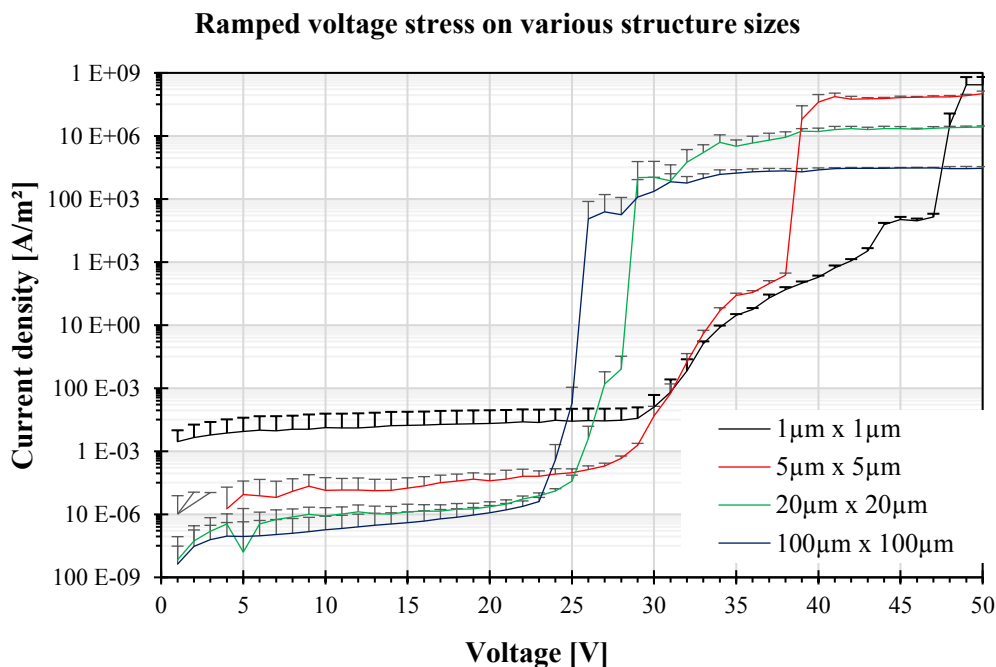


Figure 36: Current density of ramped voltage stress measurements performed on different BEOL MIS test structure sizes. Error bars indicate the sample variation.

## 6.2 Photon emission microscopy

The following chapters present photon emission microscopy (PEM) results which were obtained during the development of SBD defect localisation techniques. Two different photon emission detectors are evaluated, the silicon-CCD (Si-CCD) and the Indium-Gallium-Arsenide (InGaAs) detector. Both are assessed for measurements from the chip front side as well as from the chip back side. The necessity to use the specially developed stress methods from chapters 6.1 is clarified.

### 6.2.1 Si-CCD detector

A first impression of PEM results from the analysed back end of line (BEOL) metal insulator semiconductor (MIS) test structures can be obtained by analysing a HBD defect. Figure 37 shows an overlay from a HBD photon emission signal and the corresponding reflective image. Both image types have been measured with a Si-CCD, whereas Figure 37a shows a measurement from the front side and Figure 37b shows a measurement from the back side. For the measurement from the chips back, the bulk silicon was thinned to  $70\mu\text{m}$ . The photon emission from the HBD defect can be identified in both measurements. Even though no elaborated sample preparation is required for measurements from the front, photon emission measurements on the front generally suffer from shadowing effects. The metal on the front blocks photons that are emitted from underneath the metal layers. Here the front electrode is made of copper and aluminium. Thus, a defect localisation with front side photon emission microscopy is not possible. As described in chapter 5.2.3, the measured signal intensity for measurements from the back with a Si-CCD strongly depends on the remaining bulk silicon thickness. Recently, back side analysis with visible light required an extreme thinning of the bulk silicon to a few  $\mu\text{m}$  [44]. It turned out that the extreme thinning of the bulk silicon is a time-consuming and risky process, especially without specific tools. However, samples with a remaining bulk thickness of more than a few  $\mu\text{m}$  suffer from

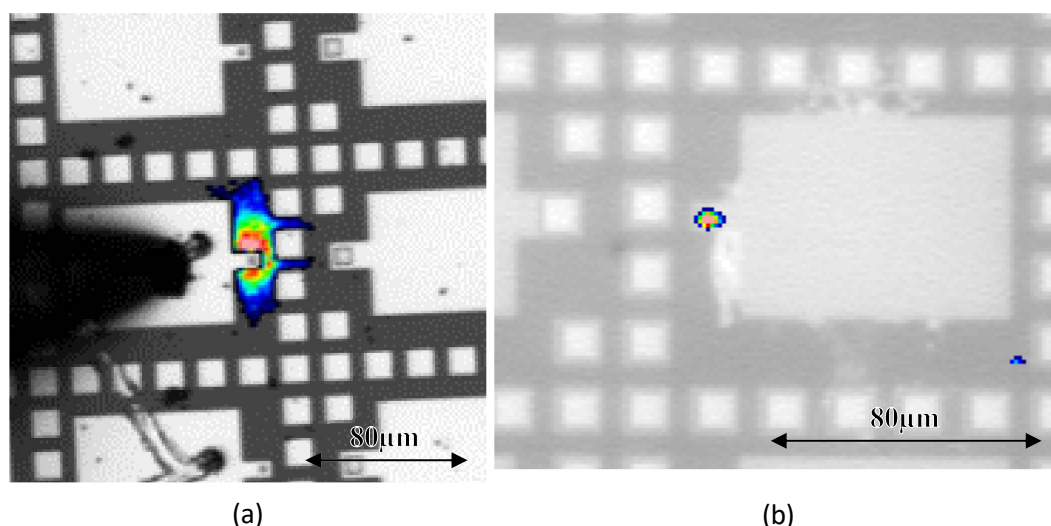
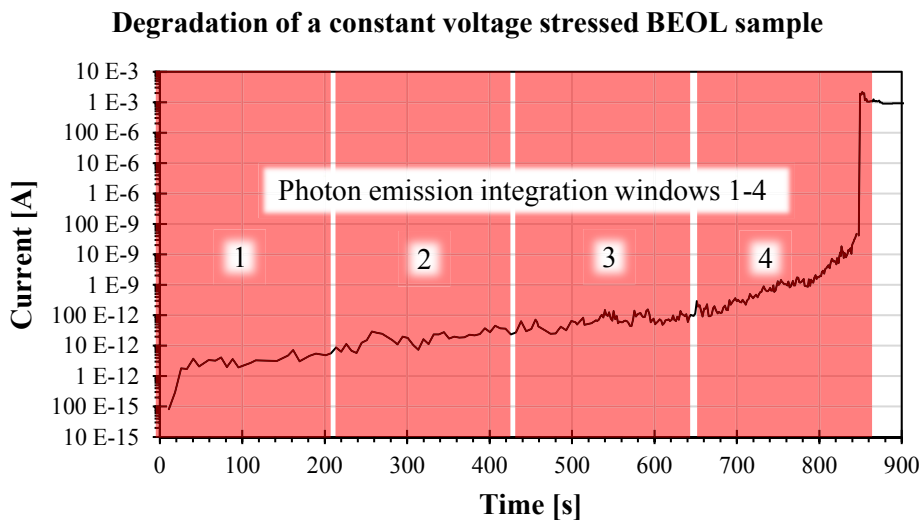


Figure 37: Superimposed photon emission signal and reflection image of a dielectric hard breakdown measured with a Si-CCD from the (a) front and (b) back

## 6. Results

significant signal absorption. The expected photon emission intensity during SBD measurements is lower than with analysed HBD defects. For this reason, back side measurements with a Si-CCD detector are postponed. Nonetheless, the detection of a HBD defect is the common application for defect localisation in dielectrics.

In the case of photon emission measurements with a Si-CCD, especially in the case of measurements on electrically weak signals, extended integration times enable an increase in the sensitivity of detection. In a first attempt to detect a SBD defect, subsequent photon emission measurements with an integration time of 210s have been performed during a constant voltage stress (CVS) measurement with a stress level of 28V. Figure 38 shows the degradation curve and the different integration windows. Unfortunately, the system used does not allow live reading of the integrated photon emission signal. It is therefore necessary to wait until the predefined integration window has finished or has been stopped manually in order to evaluate the photon emission image. The integration windows one to three did not show any photon emission results. During the fourth signal integration, the structure changed into HBD. Even though the signal integration occurred only a few seconds after the HBD, the orders of magnitude higher current generates an extraordinary number of photons and it is impossible to draw any conclusion about the SBD. The result of the photon emission from the fourth integration window can be seen in Figure 37a. Even if no SBD defect was detected with this measurement, it can be learned from the photon emission integration window three that a 210s signal integration in a current range from 20pA to 100pA and below does not show a SBD photon emission.



**Figure 38: Leakage current of a dielectric test structure under constant voltage stress of 29V; Different windows for photon emission integration are marked**

An I-t curve of a 26.5V CVS stressed structure with its integration times for photon emission can be seen in Figure 39. As described in 6.1.2, due to the reduced stress level, the time to HBD increases and thus the time to analyse the SBD is extended, allowing a further extension of the photon signal integration time. A flexible integration time is used for this measurement in order to address the varying signal intensities. The first measurement used an integration time of 1922s and covers a current range from 100fA to 500pA. With an integration time of 372s, the second photon emission integration window covered a leakage current range from 800pA to 3nA. With the following integration window number three,

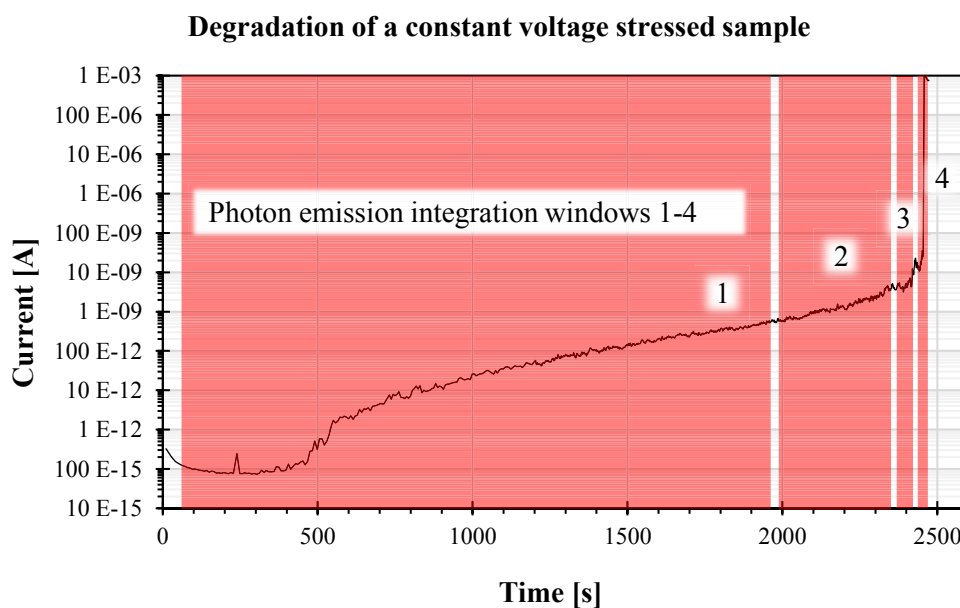


**Figure 39: Leakage current of a 26.5V stressed low k MIS test structure; Adaptive photon emission measurement integration time windows are marked**

the leakage current during the 48s integration reaches 10nA, which was previously identified as the critical level to bring the structure into HBD. A final 21s photon emission measurement during HBD can be used as a guaranteed defect localisation. All four photon emission measurements as well as a reflective image of the measured structure are shown in Figure 40. Interestingly, all four measurements show a visible photon emission spot. Even though the signal from integration window one is by far the weakest signal, despite the integration time being more than five times higher compared to integration window two. It shows that a detection of a photon emission from a leakage current lower than 500pA is possible. The difference in intensity between HBD photon emission and SBD photon emission becomes clearer when the measurement results from Figure 40b-d are compared with Figure 40e. During HBD, the detector saturates with a comparably short integration time of 21s, thus creating a blooming effect, which outshines the structures top metal and allows to identify the boundaries of the contact pad within the photon emission image.

## 6. Results

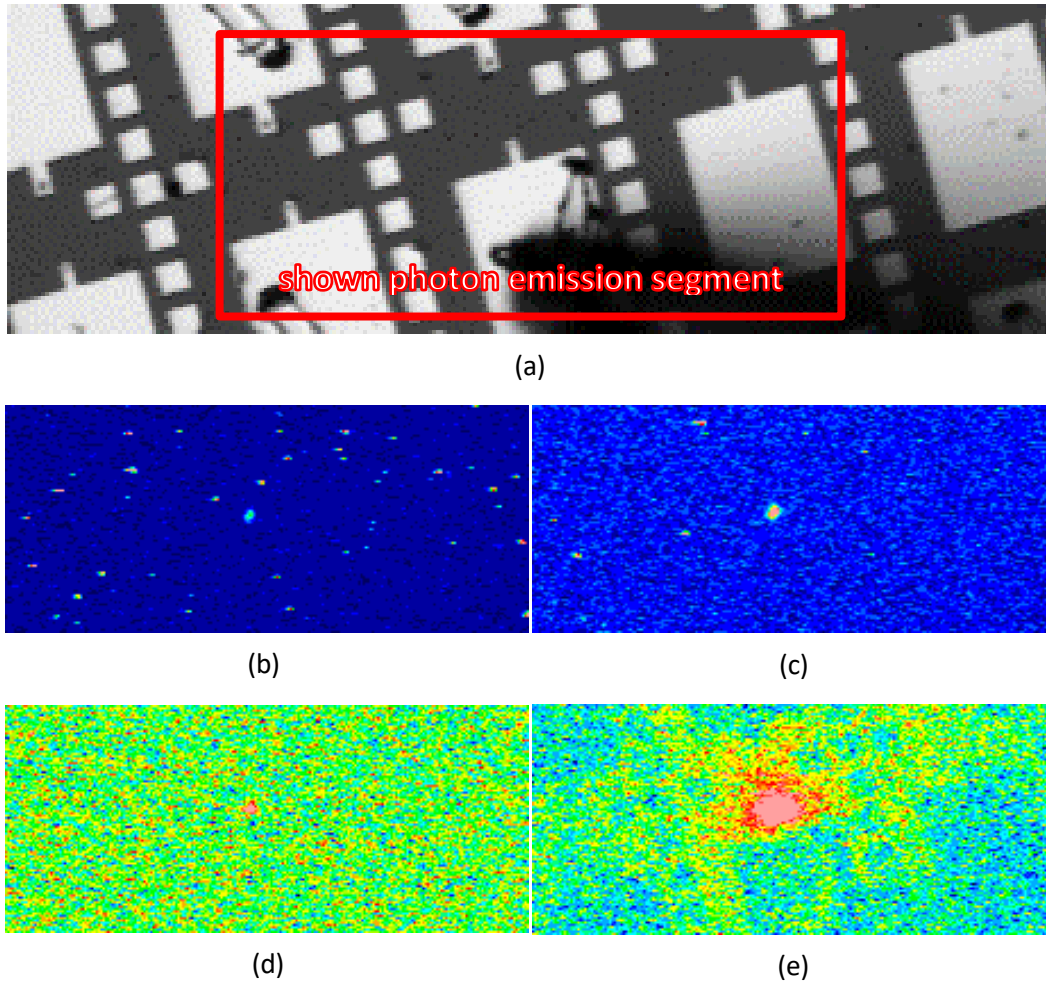


**Figure 40: Results of the photon emission measurement of a 26.5V constant voltage stressed low k MIS test structure; (a) laser scanning microscope reflection image; (b-e) photon emission results from integration windows 1-4**

Measuring a photon emission signal from a low k dielectric test structure in SBD condition is an important achievement in the development of SBD defect localisation techniques. The shown measurement proves that a SBD leakage current lower than 500pA emits measurable photon emission. However, the method presented has its weaknesses. First, the detection of the SBD cannot be planned systematically as the HBD can occur at any time. Second, due to the ongoing degradation of the measured structure during the CVS, the level of degradation cannot be determined exactly. Finally, measurements from the front suffer from shadowing effects, which always leave uncertainty in terms of localisation. The first two points have already been addressed in chapters 6.1.3 and 6.1.5 and can be solved using specialised stress methods. The previously discussed limitation to front measurements with a Si-CCD prevents an exact defect localisation. Instead, a proof of concept of a photon emission from a SBD defect is achieved and can be transferred to future experiments, especially with the InGaAs detector.

### 6.2.2 InGaAs detector

Photon emission from a low k MIS test structure in SBD condition has been successfully detected with a Si-CCD. In this context, the need of a degradation control was clarified. A combination of a constant voltage stress with a current compliance was presented in 6.1.3. This method allows to significantly slow down the further degradation.

The spectral sensitivity of an InGaAs detector allows measurements to be performed from the chip back side without complicated bulk silicon thinning. Hence there is no advantage for measuring from the front with an InGaAs detector compared to measuring from the back. Results obtained with the InGaAs detector will only be presented and discussed using back side analysis. The monitored leakage current of a sample that was exposed to constant voltage stress with a 1nA current compliance and a subsequent 100nA current compliance can be seen in Figure 41. Additionally, the resistance of the sample to monitor the level of degradation at a particular point in time is shown. Several attempts of measurements with varying measurement parameters during the 1nA current compliance phase did not show any photon emission. Even though the degradation control is functional due to the current compliance, extended integration times are not possible with an InGaAs detector. The material characteristics of an InGaAs detector generate significantly more detector noise compared to a Si-CCD. For the system used, it has been found that the maximum integration time is limited to 100s, in a combination of five frames with a 20s integration each. Further increased measurement times reduced the remaining dynamic range because the internally generated noise will saturate the detector. The noise characteristics of the two different detectors were discussed in chapter 5.2.3. The test structure was brought into HBD with the following current compliance of 100nA. The increased current by two orders of magnitude allowed measuring a photon emission signal. Figure 42 shows an overlay of the measured photon emission signal and the reflection image of the measured structure. The advantages of back side measurements are immediately noteworthy as the defect position can be determined within the test structure. However, a leakage current of 100nA is already a HBD

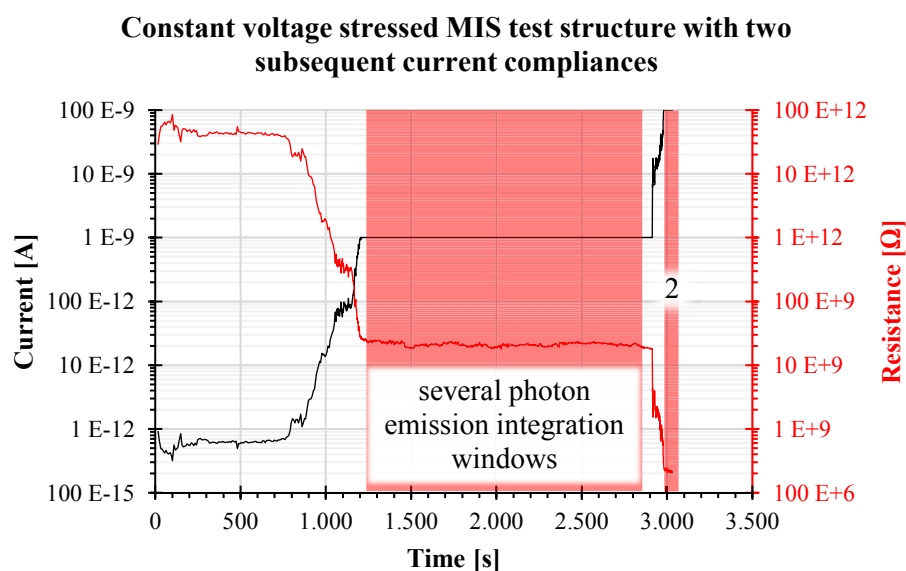


**Figure 41: Degradation curve of a constant voltage stresses low k MIS test structure with two subsequent current compliances of 1nA and 100nA. Red curve shows the sample resistance. Red shaded areas mark regions of photon emission measurements.**

## 6. Results

and orders of magnitude higher compared to the leakage current at which photon emission has been detected using a Si-CCD.

### 6.2.2.1 Solid Immersion Lens improvements

In contrast to measurements with a Si-CCD, the detection sensitivity from an InGaAs detector cannot be improved with exceptionally long integration times. This leaves the detection sensitivity of an InGaAs detector for the detection of HBD defects only. Consequentially, means to improve the measurement setup must be found. As described in chapter 5.2.5, a solid immersion lens (SIL) increased the effective numerical aperture of the measurement system. The SIL was mainly developed to increase the optical resolution of a system [45]. Figure 42 shows that the optical resolution is good enough to resolve the analysed structures even without a SIL. Moreover, the increased numerical aperture due to a SIL also increases the amount of photons collected at a given time, thus increasing the sensitivity. The effect of a SIL on sensitivity can be seen in Figure 43. Photon emission from two devices with a similar defect condition is measured with and without a SIL in order to estimate the growth in sensitivity due to the increased numerical aperture. Both DUTs feature a leakage current of 100nA with a device resistance of 210M $\Omega$  and 240M $\Omega$ . The defect measured without a SIL (Figure 43a) can be localised optically without further effort. However, an x-z view of the measured data, shown in Figure 43b and demonstrating the signal intensity, is of the same order of magnitude as the noise. Figure 43c shows a comparable defect that is measured with a SIL. The x-z view of the measured data can be seen in Figure 43d, the signal intensity has increased significantly. Calculating the signal-to-noise ratio (SNR) from both defects enables the signal gain to be quantified based on a SIL. Without a SIL, the SNR calculates to 19.7dB, whereas with a SIL it rises to 34.7dB. This leads

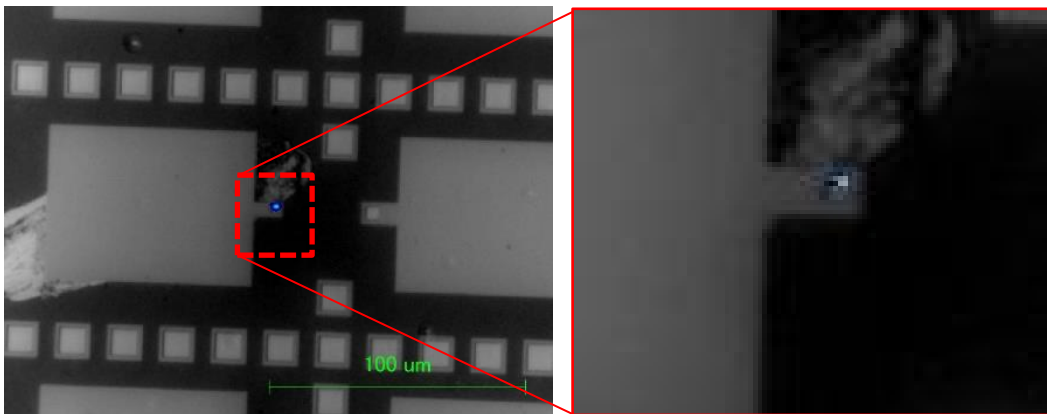
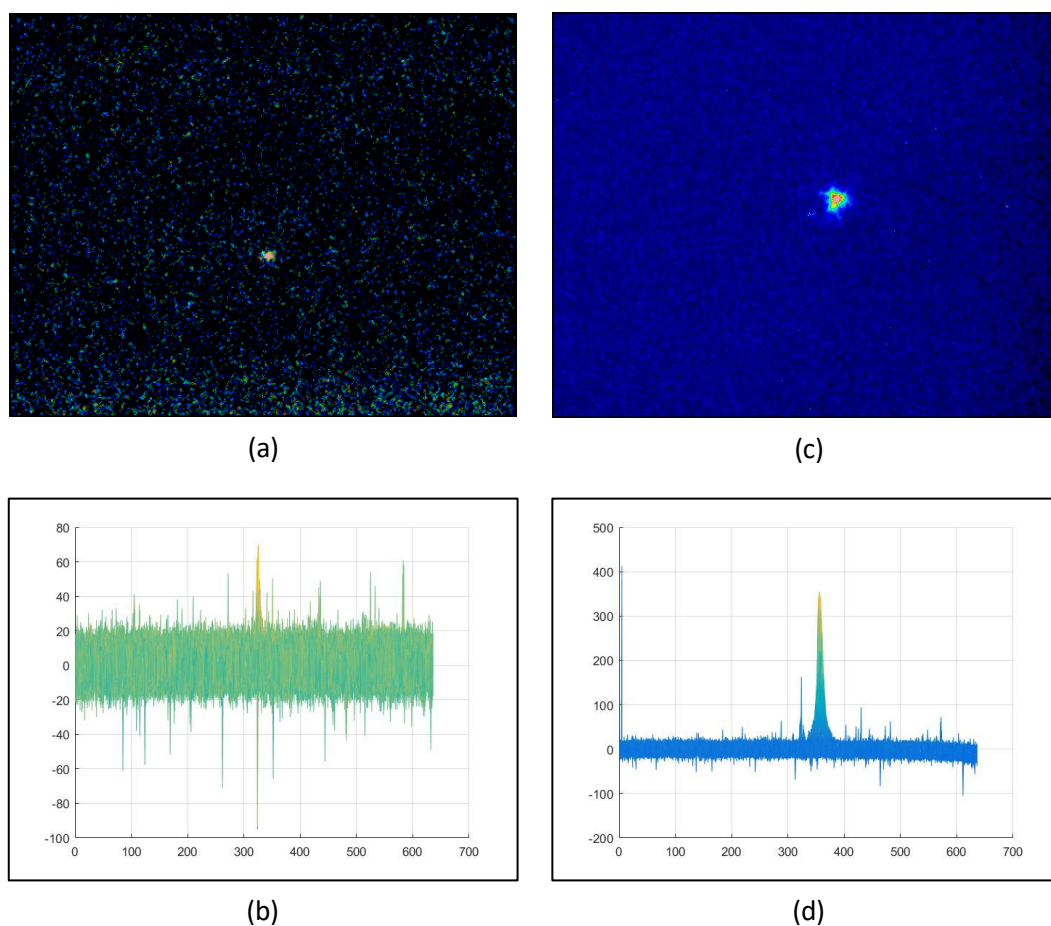


Figure 42: Back side photon emission measurement of a 100nA leakage current using an InGaAs detector;  
Defect localisation is possible within the 2 $\mu$ m x 2 $\mu$ m test structure

to a 5.6 times increased signal amplitude, due to the SIL. Consequently, the sensitivity of a photon emission measurement can be improved by using a SIL. This allows to reduce the current level of the DUT, or the level of degradation respectively. The advanced degradation method presented in 6.1.3, made it easy to vary the level of degradation by making it more convenient to study the maximum possible sensitivity of an adjusted measurement setup. A gradual reduction in current compliance by one order of magnitude per step enables the sensitivity gain due to the SIL to be analysed.

Figure 44 shows a generic degradation curve of a sample stressed with 28V constant voltage with a current compliance of 100pA. The optimised photon emission measurement with 5 frames and 20s integration each started immediately when the structure reached the current compliance. The measured photon emission results are shown in Figure 45. A clear emission spot can be identified in Figure 45a, which shows the measured photon emission. However, the defect localisation with an overlay from the emission image and the corresponding InGaAs reflection image is difficult. As can be seen in Figure 45b, the InGaAs



**Figure 43: Comparison of the measured photon emission intensity**  
**(a) without solid immersion lens, 100s (5 frames with 20s each) integration**  
**100nA leakage current 210M $\Omega$  sample resistance**  
**(b) x-z data plot of emission measurement without SIL**  
**(c) with solid immersion lens, 100s (5 frames with 20s each) integration**  
**100nA leakage current 240M $\Omega$  sample resistance**  
**(d) x-z data plot of emission measurement with SIL**

## 6. Results

reflection image suffers from noise when using a SIL. The distorted image quality remains in contrast to previously shown InGaAs reflection images, for example Figure 42. The light source used to illuminate the DUT for the reflection image acquisition has a broad light spectrum and an omnidirectional light distribution. Due to the SIL and the resulting change in the optical path, these two light source characteristics result in an immense distortion of the reflection signal. On the other hand, the laser scanning microscope integrated in the measurement setup can capture reflection images with a monochromatic light source. The adjustment of the InGaAs detector and the laser allows superimposing a photon emission image with a reflection image from a laser scanning microscope. As shown in Figure 45c, this significantly improves the image quality and enables the defect to be located.

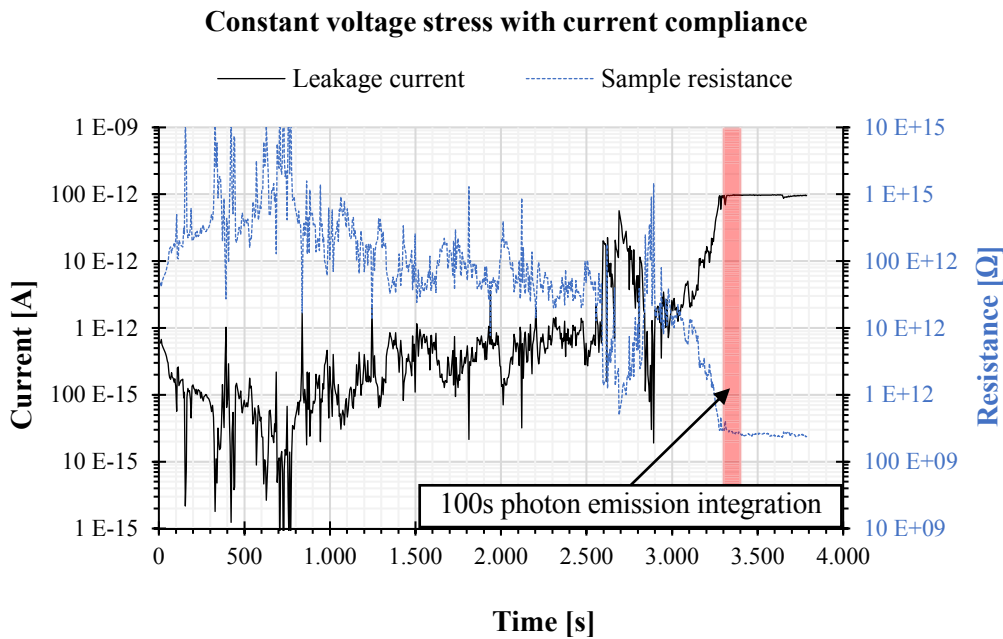


**Figure 44: Leakage current and sample resistance of a  $2\mu\text{m} \times 2\mu\text{m}$  low k MIS test structure under 28V constant current stress with a 100pA current compliance.**

The development of a method for the detection and localisation of a SBD defect with a sample resistance of  $250\text{G}\Omega$  from a leakage current of 100pA is one of the key findings of this research. The use of an InGaAs detector in combination with a SIL, a current compliance and optimised measurement conditions allow the localisation of SBD defects on a regular basis. Using this method, multiple 100pA leakage current defects from structures with several  $100\text{G}\Omega$  sample resistance have been localised. In chapter 6.5, two of these defects are also subject to a physical analysis verifying the position of the localised defect.

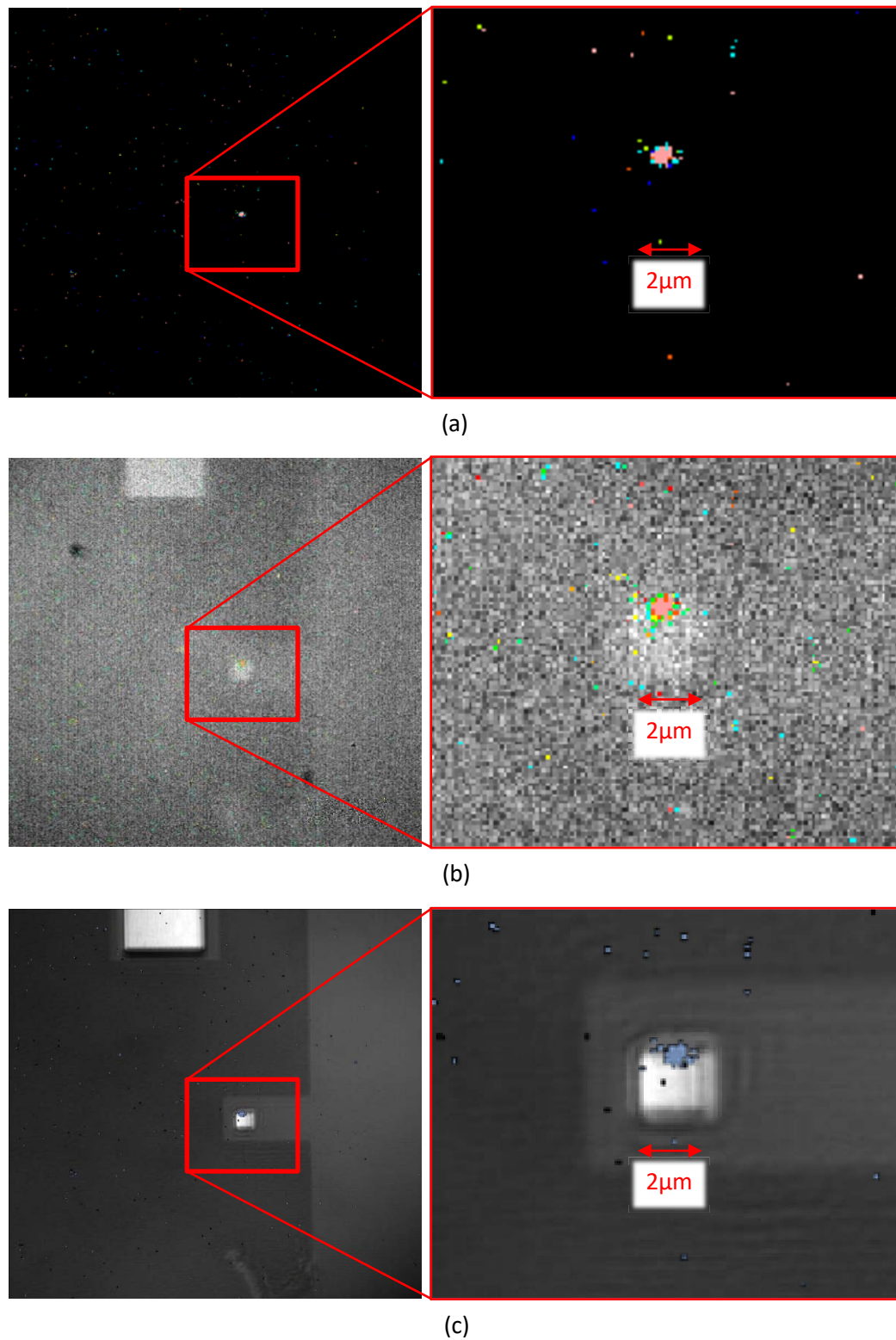


Figure 45: Photon emission measurement on a 250GΩ sample with a leakage current of 100pA (a) emission image (b) emission image, superimposed with the InGaAs reflection image (c) emission image, superimposed with the laser scanning microscope reflection image

## 6. Results

### 6.2.2.2 Additional results

As an alternative stress method with short turnaround times, a ramped voltage stress (RVS) with a current compliance was described in chapter 6.1.4. Figure 46 shows an I-V curve of a RVS with a current compliance of 100pA. A voltage of 32V is required to reach current compliance. Compared to CVS measurements, this method applied an increased voltage to the sample. The measurement of the photon emission started as soon as the current compliance was reached. As the intensity of the photon emission is related to the current and voltage, the increased voltage suggests a stronger photon emission signal compared to a photon emission signal measured from a CVS generated 100pA leakage current defect. This expectation is confirmed by the photon emission measurement shown in Figure 47. The defect was measured using a SIL and optimised photon emission measurement conditions. When comparing the signature of the photon emission defect with the photon emission shown in Figure 45, it can be seen that the higher voltage level caused a more widespread but also more intense photon emission signal. Shown and discussed later, physical analysis will support this result. However, defect generation only took 115s compared to more than 3000s for a CVS with current compliance generated defect.

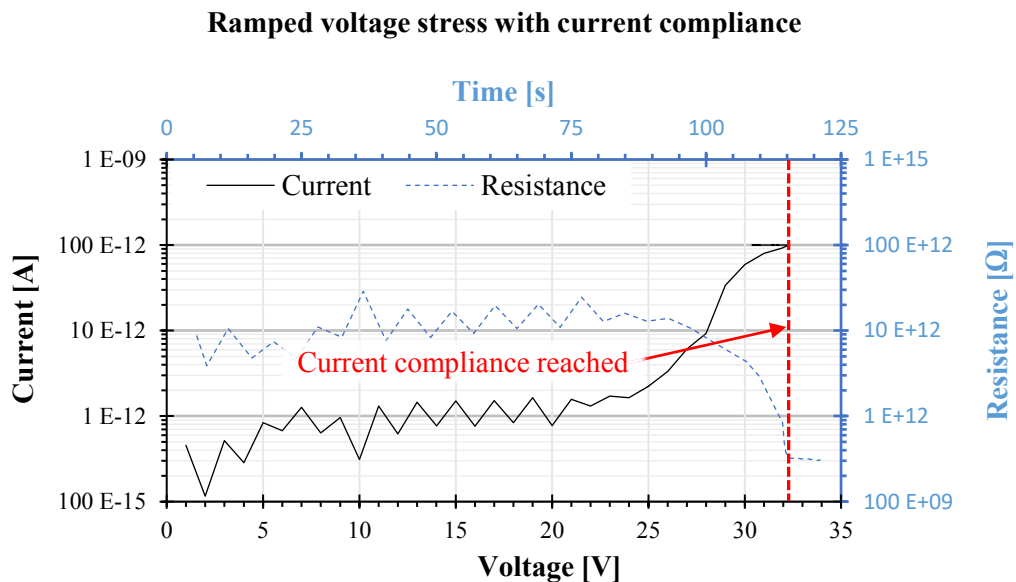


Figure 46: Degradation curve of a low k MIS test structure under a ramped voltage stress with a current compliance of 100pA; I-V curve shown on the primary axes shown in black; R-t curve shown in blue on the secondary axes (dashed)

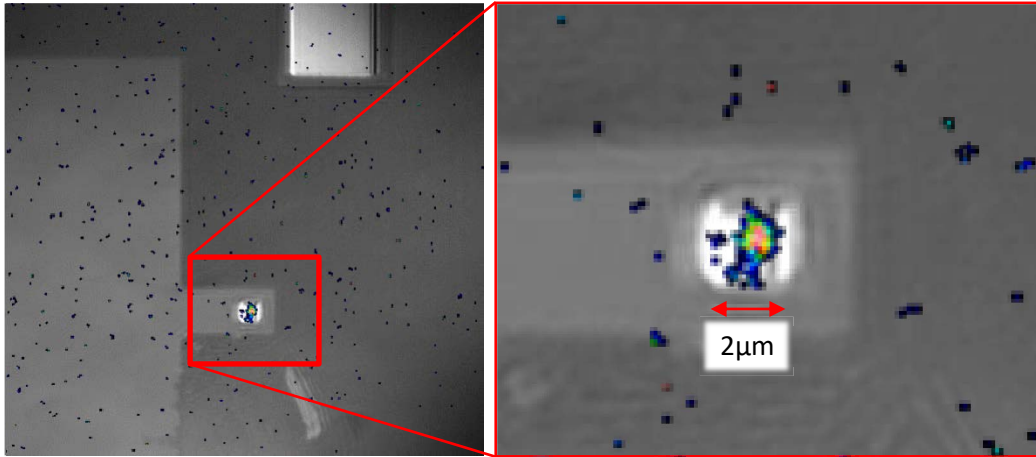


Figure 47: Superimposed reflection image of the laser scanning microscope and photon emission image from a 100pA leakage current defect; a ramped voltage stress with current compliance was used to create the defect

#### 6.2.2.2.1 Pre-stress method

Another series of tests evaluated a combination of a RVS with current compliance and a subsequent constant voltage stress with current compliance. The aim is to shorten the defect nucleation phase but not to apply any extraordinary voltage that potentially generates additional defects. A current compliance of 10pA at the initial RVS applies a pre-stress to the sample. This pre-stress is one order of magnitude below the regular localisable leakage current of 100pA. A subsequent CVS with current compliance is intended to further degrade the structure in a controlled manner. Figure 48 shows two pre-stress degradation I-V curves. Sample A reached the 10pA current compliance at a stress voltage of 35V, sample B reached the 10pA current compliance at 25V. According to chapter 6.1.1, sample A shows

#### Ramped voltage stress with 10pA current compliance; Sample A

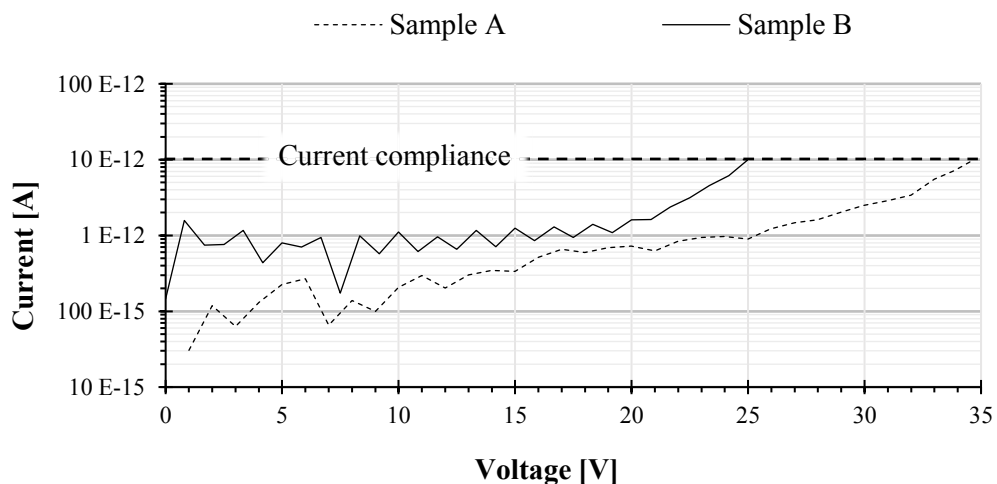
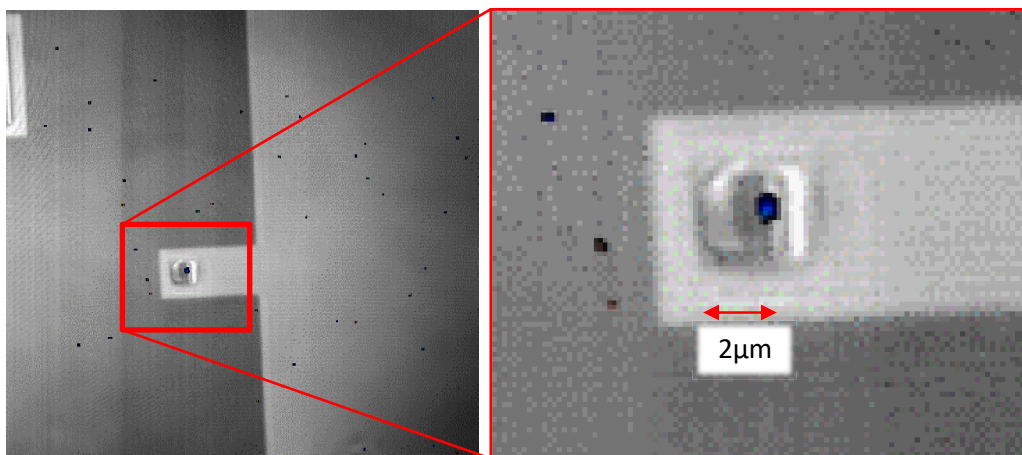


Figure 48: Pre-stress degradation with a ramped voltage stress and a 10pA current compliance of sample A and sample B

## 6. Results

the expected degradation behaviour. Sample B shows an increased leakage current level as well as a faster degradation, resulting in an applied voltage of 25V to reach the current compliance of 25V. Concluding, sample B is a non-representative sample. However, the earlier degradation allows to perform a subsequent CVS without additional damage due to an increased voltage stress of more than 30V. Chapter 6.1.2 showed that a voltage stress above 30V changes the degradation behaviour.

In order to further improve the sensitivity of the photon emission microscopy, both samples have been evaluated with photon emission microscopy. The measurement of the 100s photon emission integration was performed during the phase of the 10pA constant leakage current. Sample A shows a faint photon emission signal, which is shown in Figure 49. Even though the signal nearly vanishes in the measurement noise, chapter 6.5 will show that this faint signal correctly located the defect.



**Figure 49: Superimposition of a photon emission image with the reflection image of a laser scanning microscope; the photon emission was measured from a leakage current of 10pA**

The photon emission measurement for sample B did not show any detectable photon emission. Even though sample A and sample B feature a leakage current of 10pA, the 10V higher voltage of sample A makes the difference in measuring a photon emission signal. This result is backed up by the previous results, which showed an increased photon emission intensity from a 100pA leakage current defect generated with a RVS compared to a 100pA leakage current defect generated with a CVS. Consequentially, as tempting as the reduced turnaround time of a RVS is, with a limitation to less than 30V, a correctly chosen CVS is often the better choice. In the case of sample B, however, an additional initial leakage current resulted in the voltage being lower than expected to reach current compliance. Thus, the applied voltage was limited to 25V and additional defects were generated due to extraordinary high voltage levels. A subsequent 25V CVS was used to further degrade the sample to a leakage current of 100pA. The I-t curve can be seen in Figure 50. The degradation continued in a similar manner to that of the other constant voltage stressed samples shown. The resulting photon emission image with the laser scanning microscope overlay can be seen in Figure 51. The defect is sharply contoured and no systematic differences to other CVS generated defects, e.g. as shown in Figure 45, can be identified.

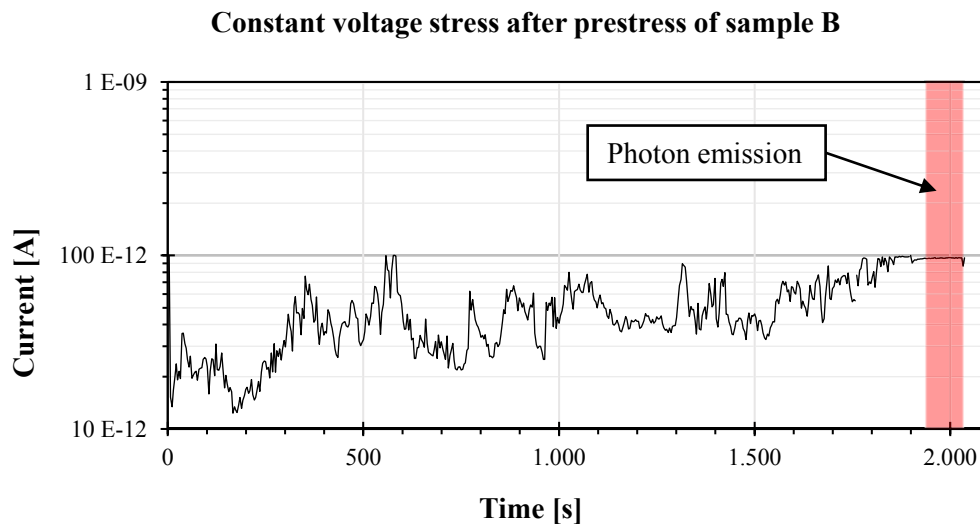


**Figure 50: Subsequent constant voltage stress with a 25V stress level and a 100pA current compliance. Stress was applied after a pre-stress**

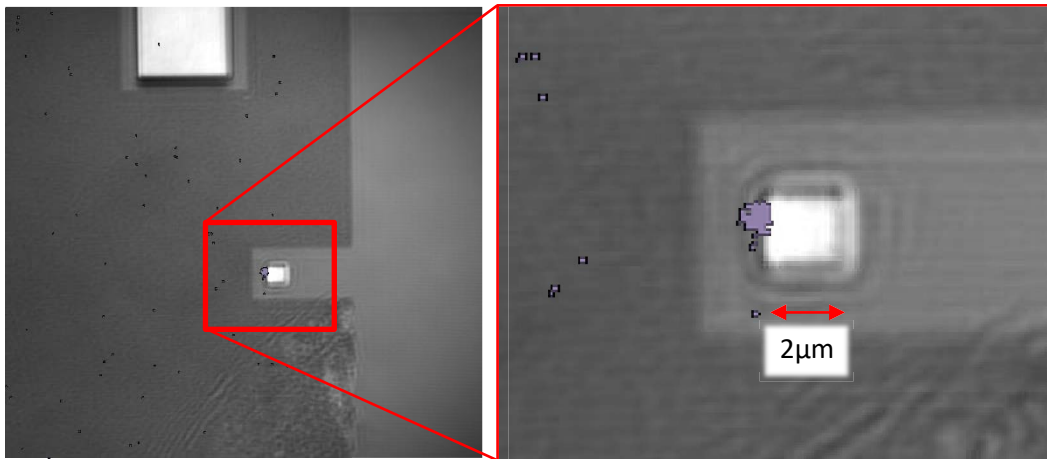


**Figure 51: Photon emission image from a 100pA leakage current from a 25V constant voltage stress following a pre-stress**

## 6. Results

### 6.2.2.3 *Detection limits*

CVS generated SBD defects, which can be considered representative of defects that occur under normal operation conditions, can reliably be located with photon emission. The minimally reliable SBD defect localisation is possible from a leakage current of 100pA. The sample resistance from these defects is  $\sim 250\text{G}\Omega$ . However, it must be differentiated between the minimum detectable level of degradation and the minimum reliable detectable level of degradation. Various parameters that are difficult to control can affect the detection sensitivity. The sensitivity of photon emission microscopy measurements is strongly related to an optimised optical path, e.g. correct focus. Correct focusing on the origin of the photon emission within a 3D structure requires the prediction of the z-position of the photon emission. Depending on the possible thickness of the material analysed and the depth of field of the objective used, it can be challenging to set the correct focal plane. It is possible to use the high-resolution laser scanning microscopy image to support the focusing process. However, it has been found that the focus level of the laser and the focus level of the InGaAs detector differ. Furthermore, often the focus level of the photon emission differs from that of the lasers and the InGaAs reflection image. As long as the photon emission is within the depth of field of the objective used, the intensity of the photon emission is not significantly reduced. On the other hand, the use of a SIL significantly reduces the depth of field. Furthermore, the InGaAs detector reflection image in combination with a SIL suffers from increased distortion due to the broad spectra of the illuminating light source. This problem aggravates the identification of the correct focus plane. Finally, using a SIL requires thinning the bulk silicon to match the fixed SIL geometry. A variation of the bulk silicon results in a variation of the optical path that emitted photons must take on their way to the detector. This varies the image quality as well as the detection sensitivity. All these positions influence the sensitivity of the photon emission measurement, and they can vary from measurement to measurement and from sample to sample.

An SBD defect with a 100pA leakage current and no overvoltage has been identified as the lowest order of magnitude of degradation that can be reliably located. However, for this thesis, steps of improvement are considered in full orders of magnitudes only. Thus, a localised non-overstressed defect with a leakage current of 50pA is not discussed in detail. Finally, it has been shown that a 10pA leakage current can be detected with a 10V increased voltage. Without a doubt, the detection of a non-overstressed 10pA leakage current can be archived with further improvements in the optical path, e.g. sample preparation and a dedicated study of the influence of the focus level on the sensitivity. Anyway, these topics are out of scope of this thesis.

### 6.3 Spectral photon emission

The previous chapters have dealt with localisations of soft breakdown (SBD) defects with a sample resistance of several  $100\text{G}\Omega$  using photon emission microscopy (PEM). This defect localisation was possible due to the specially developed electrical stress methods presented and the improved procedure for photon emission measurement. As a first approach to obtain more insight into SBD degradation without a destructive physical analysis, spectral photon emission microscopy (SPEM) can provide information about the characteristics of the photon emission source. Several samples with different levels of degradation both in SBD condition and in HBD condition have been analysed with SPEM. A prism is used to extract the spectral information from the photon emission, as described in chapter 5.3. A solid immersion lens is used for all SPEM measurements.

The spectral evaluation of different SBD levels enables a better understanding of the SBD degradation process. However, only considering spectral evaluations of HBD defects and SBD defects enables the potential of SPEM measurements to be understood in the context of low  $k$  dielectric degradation.

#### 6.3.1 Hard breakdown spectra

Spectral analyses of HBD defects with varying current levels give a first impression of the spectral device characteristics. Figure 52 shows two spectral photo emission measurements from a single HBD defect, which were generated with a constant voltage stress (CVS) with a subsequent step-wise increase in current compliance. The initial current compliance was set to  $50\text{nA}$  (Figure 52a) and the highest current compliance was set to  $50\mu\text{A}$  (Figure 52b). Both spectra show a clear x-component as well as a y-component. Chapter 5.3 described that a photon emission with a non-point source is the reason for such a characteristic. In order to realise a point source such as photon emission, a lower magnification is beneficial. However, the demand for high sensitivity requires a SIL, which is usually accompanied by an increased magnification. Even though a SIL is not necessary for the analysis of HBD defects, it was decided to use the SIL for all levels of degradation for better comparability

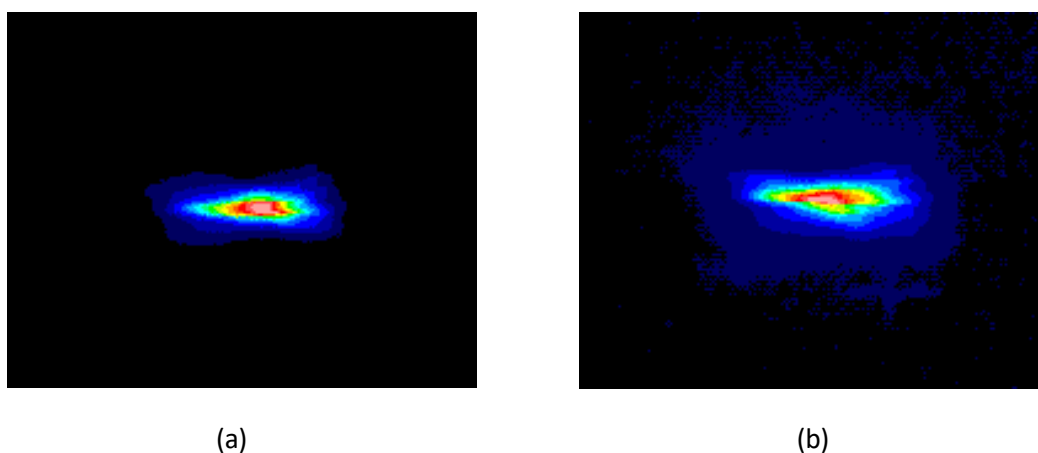
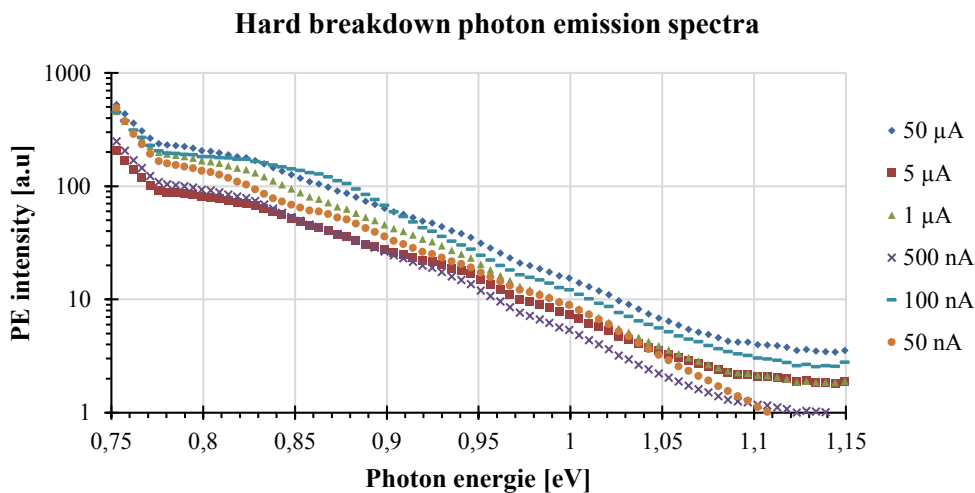


Figure 52: Spectral photon emissions from a hard breakdown with varying current compliances. Initial current compliance of (a)  $50\text{nA}$  and the endpoint current compliance of (b)  $50\mu\text{A}$  are shown.

## 6. Results

of the spectral results from HBD defects and SBD defects. Furthermore, in order to extract the spectra from the spectral measurement, the spectral that contains the maximum plus two lines above and below is arithmetically averaged and evaluated, as described in 5.3.2. However, any remaining uncertainty caused by the distortion of the y-dimensional expanse of the spectra cannot be eliminated.

The extracted spectra from the HBD SPEM measurement shown in Figure 52 as well as all analysed intermediate levels of current compliances are shown in Figure 53. The full set of spectral measurements is linked to the following current compliances: 50 nA, 100 nA, 500 nA, 1  $\mu$ A, 5  $\mu$ A and 50  $\mu$ A.



**Figure 53: Photon emission spectra of a hard breakdown with stepwise increasing current compliance**

All spectra show a continuous exponential relation between photon energy and measured photon emission intensity. This is typical of photon emission that is caused by an electrical field rather than an electron hole recombination process [12]. The parameter electron temperature represents the kinetic energy that the electrons absorb by passing an electrical field and that can be extracted from the exponential slope of a photon emission spectrum related to an electrical field. Thus, the comparison of the electron temperature of different spectra allows to compare the kinetic energy absorbed by the electrons. The extraction of this parameter is described in chapter 5.3.3. The electron temperature is extracted for the individual measurements on the entire set of the HBD defect that subsequently further degrades. Table 1 shows the extracted electron temperatures. Despite the orders of

Current compliance	50 nA	100 nA	500 nA	1 $\mu$ A	5 $\mu$ A	50 $\mu$ A
Electron temperature	702 K	720 K	686 K	720 K	858 K	795 K

**Table 1: Electron temperatures extracted of a set of subsequently increasing current compliances of a single sample**

magnitude differing current levels, the slope of the different spectra does not vary significantly. No gradient can be identified between the measured electron temperature and the applied current compliance or the level of degradation. This means that the characteristics of the photon emission source do not change significantly during the analysed measurements. On the other hand, as will be described in chapter 6.5 (Results of the Physical analysis) different current levels during a HBD show different defect morphologies.

Spectral analysis of different degradation levels of a HBD gives a first insight into the characteristics of the photon emission source. However, the focus of this work is on the development and evaluation of SBD defect analysis techniques.

### **6.3.2 Soft breakdown spectra**

Obviously, a sample that has been analysed in HBD condition cannot be used for subsequent analyses on SBD defects. A second set of spectral measurements is thus carried out on a single sample stressed with a CVS with subsequent increasing current compliances. This time the set of current compliances consists of the following current levels: 100pA, 500pA, 1nA, 5nA, 10nA. The extracted spectra are shown in Figure 54. All spectra have been normalised to one at a photon energy of 0.85eV. Additionally, the linear fittings are shown that have been used to extract the electron temperatures from the different spectra. All SBD spectra show an exponential relation between photon energy and measured photon emission intensity. This indicates electrons accelerated by an electrical field, which generate photons due to impact ionisation [12]. Contrary to the HBD spectra, the exponential slope depends on the current compliance, or the level of degradation, respectively. As degradation progresses, the slope of the spectrum becomes steeper; thus the electron temperature decreases. Therefore, a clear relation between the exponential slope and the level of degradation can be identified.

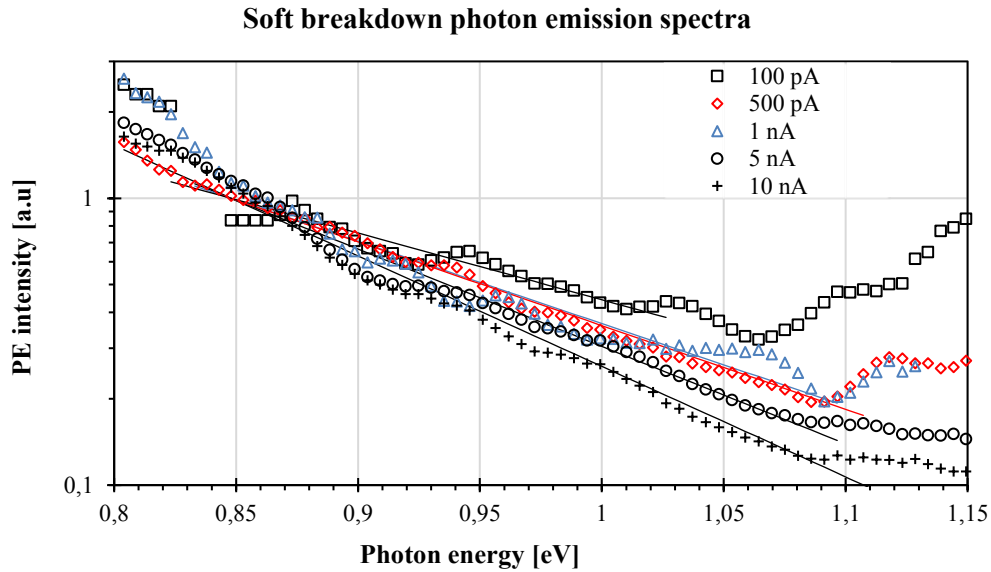


**Figure 54: Photon emission spectra of a soft breakdown with gradually increasing current compliance; Spectra are normalised at 0.85 eV**

The reduced current levels result in decreasing signal to noise ratio. Hence, it is inevitable to characterise the quality of the measured spectra. The logarithmically plotted spectral data are supposed to fit a linear regression. The goodness of fit of linear regression can be qualified by the coefficient of determination. Furthermore, it is necessary to adjust the range of the photon energy used to adjust the linear regression to meet the reducing signal to noise ratio with decreasing current levels. For this thesis it has been chosen that the coefficient of determination must be 0.95 or higher. This means that 95% of the data variance can be explained using linear regression.

Table 2 summarises the current compliance level, the photon energy range used to fit the linear regression, the coefficient of determination as well as the extracted parameter electron temperature. With a current compliance of 5nA and 10nA, the spectral data can be extracted from the entire spectral range from 0.83eV to 1.10eV. In order to maintain a coefficient of determination higher than 0.95 for the spectral data measured during the current compliance of 500pA and 1nA, it is necessary to reduce the fitting range of the photon energy. Finally, the spectrum of the 100pA current compliance does only show a coefficient of determination of 0.84, even though the fitting range has been reduced to 0.84eV - 1.03eV. This is to be expected as the minimum reliable localisable level of degradation was previously identified for defects with a leakage current of 100pA. During a SPEM measurement, the emitted power is spatially distributed and thus the sensitivity is expected to decrease. However, the extraction of a spectrum is technically possible when the photon emission spot is localised. Figure 55 shows the spectral measurements of different leakage currents. The spectrum of the 100pA leakage current is rarely identifiable. As the intensity of the spectrum does show an amplitude similar to that of the noise, the identification is only possible since a cluster of pixels of higher intensity is visible. The 500pA leakage current generates a much better signal to noise ratio, even though some surrounding noise pixels are still of the same order of magnitude. With an increase in the leakage current to 1nA, the surrounding noise is significantly suppressed as the signal to noise ratio is further increased. Concluding, it can be said that the measurement of a

spectrum of a 100pA leakage current is technically possible, but the data are subject to an increased failure tolerance. This achievement does go hand in hand with the findings presented in chapter 6.2.2.3. A defect generated by a 100pA leakage current was identified as the lowest reliable localisable defect, if only full orders of magnitude were taken into account. However, a defect of 50pA leakage current is localised without electrical overvoltage, and with electrical overvoltage a localisation of a 10pA leakage current defect was possible.

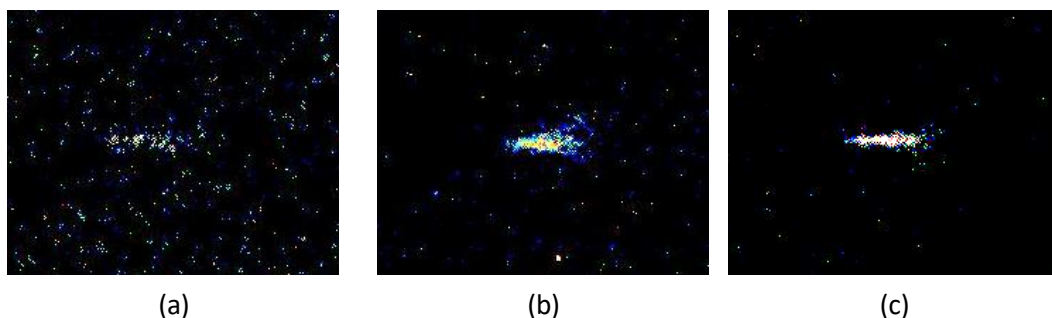


Figure 55: Measured spectral data from different leakage currents (a) 100pA; (b) 500pA; (c) 1nA

Current compliance	100 pA	500 pA	1 nA	5 nA	10 nA
Electron temperature	2165 K	1629 K	1558 K	1484 K	1258 K
Fitted photon energy range	0.84eV – 1.03eV	0.84eV – 1.07eV	0.84eV – 1.04eV	0.83eV – 1.10eV	0.83eV – 1.10eV
Coefficient of determination	0.8452	0.9961	0.9551	0.9779	0.9891

Table 2: Soft breakdown electron temperatures at different current levels

### 6.3.3 Degradation characterisation with SPEM

The spectral characteristics of different SBD and HBD levels of degradation separately considered were discussed in the previous chapters.

In a next step, a full set of spectral measurements is performed on four different samples, starting with a 100pA current compliance and a stepwise increasing current compliance up to 50 $\mu$ A. Thus, a complete picture of the change in electron temperature as degradation progresses is measured. Figure 56 shows the electron temperature plotted against the logarithmic leakage current as well as the logarithmic resistance. All samples shown have been stressed with a CVS and a stepwise increase in current compliance. The full degradation cycle of one sample is projected in one graph. The graphs of all four analysed

## 6. Results

samples can be divided into two regions. For leakage currents less than 50nA, the electron temperature decreases with ongoing degradation. This region allows to fit a linear trend that can be extrapolated to the second region of the graphs. The second region for leakage current higher than 50nA is characterised by a constant electron temperature. All four samples show this characteristic, however "SPEM sample 0" features significantly higher electron temperatures in the first region. An increased electron temperature means that the kinetic energy absorbed between a scattering process is increased. As the applied electrical stress is comparable for all four SPEM samples, the cause must be device-related. First, the dielectric layer can be thinned locally due to manufacturing variations. With a constantly applied voltage, the electrical field strength is increased. Second, and more likely, the sample being analysed contains no or less extrinsic defects. Thus, the defect density is reduced. Whereas both variations are caused by manufacturing variation, control of a layer thickness is likely to be handled well by imec. However, the process control of a porous low k dielectric deposition is still challenging.

The electron temperature is a monitor for changes in the photon emission source, or the electrical field characteristics, respectively. Considering the development of the electron temperature in relation to the level of degradation of a complete degradation cycle, it can be observed that the source of the photon emission does not change if the level of degradation is higher than a leakage current of 50nA.

The physical cause of a SBD defect is assumed to be a morphological change within the dielectric material. In low levels of degradation, a major part of the electrical field will be consumed by this dielectric. Changes within the dielectric will be directly transferred into

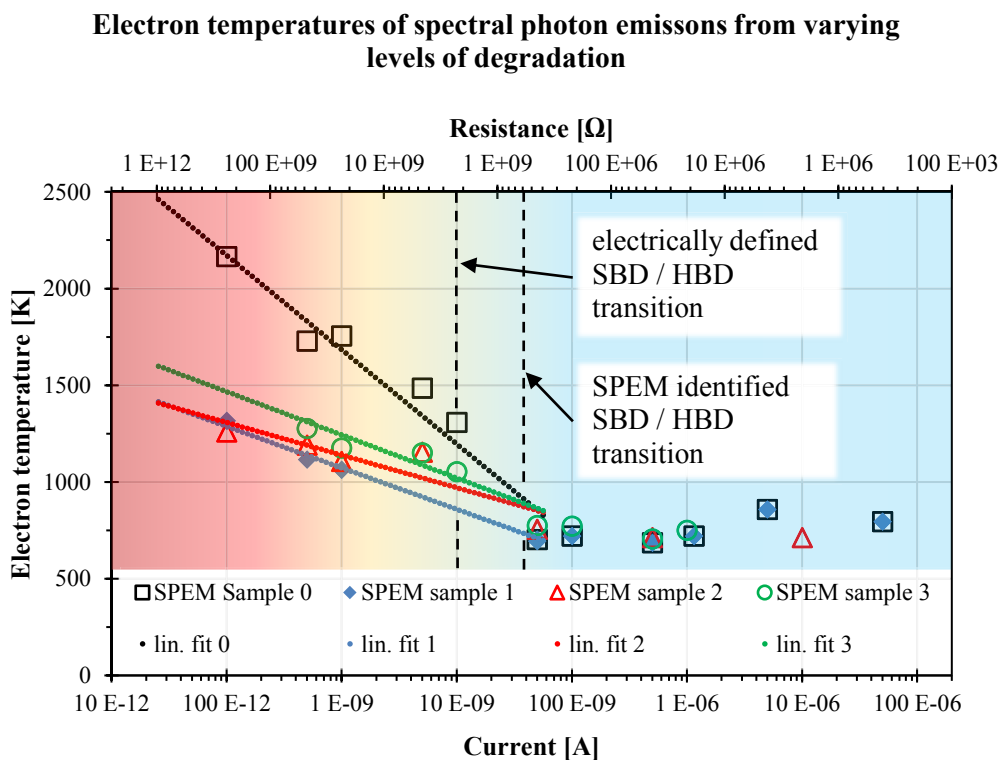


**Figure 56: Extracted parameter electron temperature from three different samples with gradually increasing levels of degradation; Linear regression for each sample soft breakdown region**

changes in the kinetic properties of the electrons that generate the photon emission, to the electron temperature, respectively. A physical analysis presented later will show that different levels of HBD degradation result in morphological changes within the bulk silicon underneath the defect area only. Under this condition, the field properties and thus the electron temperatures are constant.

From the electrical characterisation in chapter 6.1, the transition from SBD into HBD was identified at a leakage current of 10nA. With the support of spectral photon emission analysis and the extraction of the electron temperature, it can be shown that the definition of the SBD / HBD transition can be specified. Depending on the definition of a SBD, SPEM enables the definition of the SBD by means of a range bound electron temperature. With spectral photon emission analysis, it is possible to not only differentiate the HBD region from the SBD region, but also to identify changing characteristics of the photon emission source during the SBD.

#### 6.4 Optical beam induced resistance change

Optical beam induced resistance change (OBIRCH) is a contactless failure isolation technique. The measurement principles are described in chapter 5.5. The development of metal insulator semiconductor devices for back end of line test structures by imec enables to make use of the infrared transparent back. This allows local heat injection to be applied through the back of the chip, directly onto the low k dielectric layer. This local heat injection generates local resistance changes. The use of a constant current source to track the resistance change is evaluated.

The previous chapters have shown that using a constant current source allows reliable degradation control. In order to measure the thermal induced voltage alteration (TIVA), the voltage drop at the device under test (DUT) is measured using a voltage amplifier in AC coupling mode. The voltage amplifier used is the SR560, which is presented in chapter 4.3. The initial experiments have been performed on samples that were brought into hard breakdown (HBD) using a ramp voltage stress without current compliance. Later, different constant current levels have been applied to the HBD defect. Figure 57a shows an OBIRCH image of a HBD defect with a subsequently applied constant current stress of  $1\mu\text{A}$ . The defect can be localised by superimposing the corresponding laser reflection image shown in Figure 57b. No filtering and an amplification factor of 10 were used in order to measure the shown OBIRCH signal. Next, the same defect was measured with an applied current stress of  $1\text{pA}$ . The image acquisition time was set to 8s, and the measured OBIRCH signal is shown in Figure 57c. Signal filtering with a bandpass from 10kHz to 100kHz and an amplification factor of 1000 was used to measure this signal. The measured signal from this  $1\text{pA}$  current is significantly weaker and less sharply localised compared to the signal generated by the  $1\mu\text{A}$  current. Defect localisation can, however, be performed with the superimposed reflection image shown in Figure 57d. Even though the defects shown are localised on a HBD sample, the defect localisation from a  $1\text{pA}$  current is encouraging for further localisation experiments on soft breakdown defects.

A constant voltage stress (CVS) with a current compliance is used for a controlled soft breakdown (SBD) degradation, as described in chapter 6.1.3. A SBD defect has been generated with a current compliance of  $1\text{nA}$  and a corresponding sample resistance of  $20\text{G}\Omega$ . Figure 58a shows a measured OBIRCH signal from this defect. The image was measured with a bandpass filter from 10kHz to 100kHz and an amplification factor of 20,000. Compared to the analysed HBD sample shown in Figure 57, the optical magnification used to measure the SBD defect was reduced. This acts as pixel binning: combining the signals of multiple pixels from a higher magnification to one super-pixel at lower magnification increases the sensitivity at the expense of optical resolution. This technique is well known from digital photography in order to increase the pixel information. Although pixel binning is software-based in digital photography, for OBIRCH the laser spot is assumed to be much larger than the actual defect. Thus, a reduced magnification keeps the input stimuli constant, but the signal readout matrix summarises a larger physical area into one pixel. This can be considered as hardware-based pixel binning. However, the change in magnification would have required an adjustment of the bandpass frequencies, which has not been carried out in the measurement shown in Figure 58. Whereas the detection of the defect is distinct, a localisation is not possible. A signal tail, such as that shown in Figure 58a, is clear evidence of improper signal filtering. This problem has not been addressed any further, since no further achievements have been expected from this type of measurement.

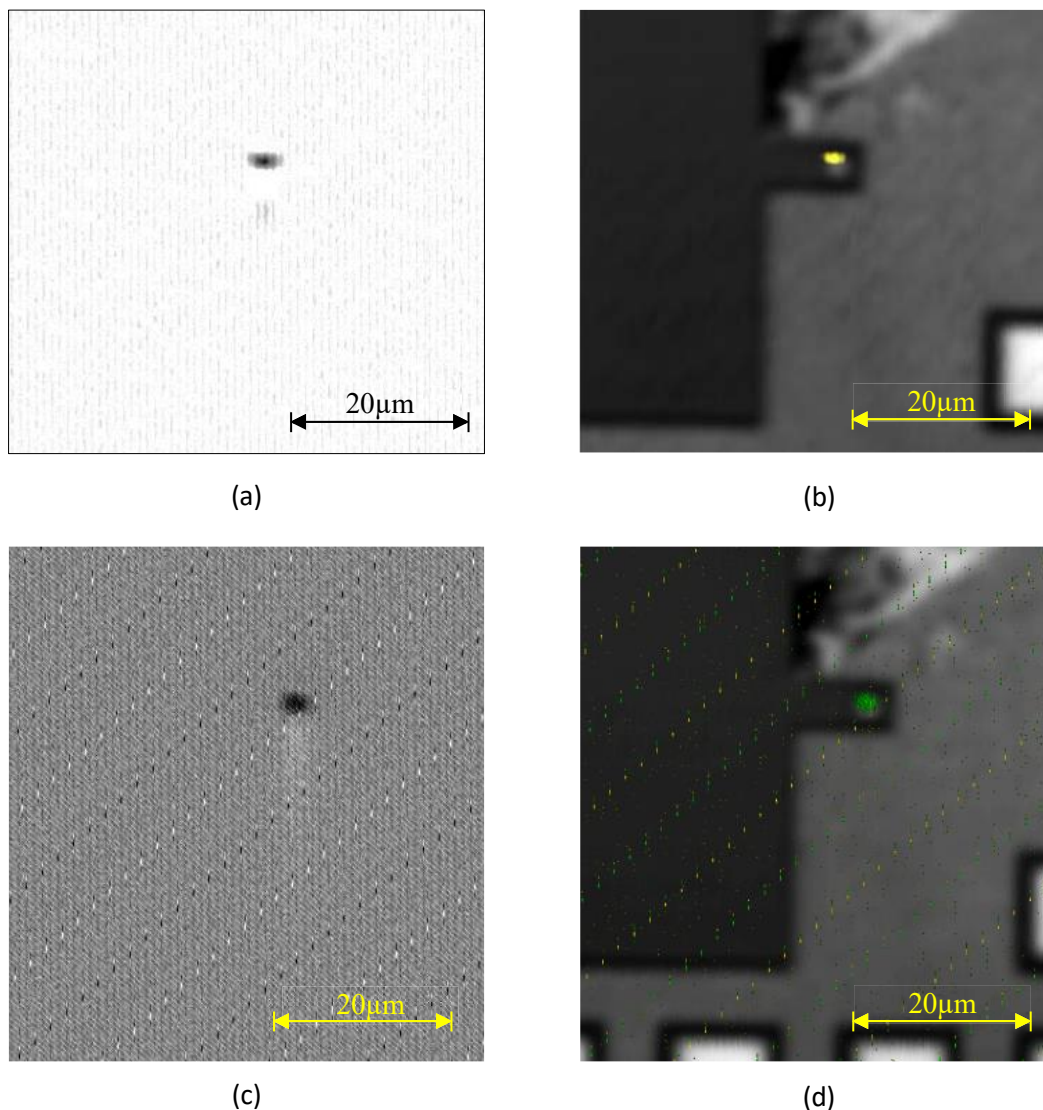


**Figure 57: Optical beam induced resistance changes measurement on a structure in hard breakdown with the following varying currents: (a) Signal from a  $1\mu\text{A}$  current and (b) the associated laser reflection image overlay; (c) Signal from a  $1\text{pA}$  current and (d) the associated laser reflection image overlay**

The detection of a  $20\text{G}\Omega$  soft breakdown defect with OBIRCH is a result worth mentioning, as it proves the concept of a SBD defect detection using thermal laser based techniques. Despite the detection of a  $1\text{pA}$  current from a HBD defect, the lowest detectable SBD level of degradation was due to a leakage current of  $1\text{nA}$ . As the available hardware limits further improvements, thermal laser based experiments have been postponed at this point. The experimental setup of the measurements is shown in chapter 5.5. A voltage amplifier is connected in parallel to the DUT and the current source is connected in series with these two. This setup is required in order to measure the correct voltage drop across the DUT. For a SBD defect with a  $1\text{nA}$  leakage current and lower, the corresponding DUT resistance is  $20\text{G}\Omega$  and higher. On the other hand, the input resistance of the voltage amplifier is constant at  $100\text{M}\Omega$ . A DUT of  $20\text{G}\Omega$  thus changes the overall resistance of the parallel circuit of DUT and voltage amplifier by  $0.497512\%$ . Consequentially, a beam induced change in resistance, changes only  $0.497512\%$  of the overall resistance. For a  $20\text{G}\Omega$  DUT, the amplitude of a thermal laser based voltage alteration is reduced by a factor of 500 due to

## 6. Results

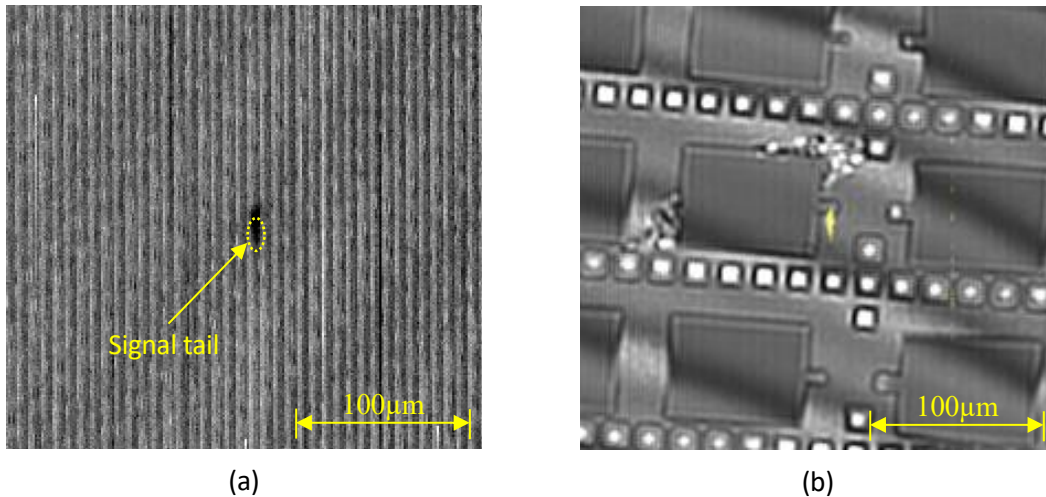


**Figure 58: Soft breakdown defect detection with (a) optical beam induced resistance change and (b) the corresponding reflectance image overlay of a  $20\text{G}\Omega$  sample with a  $1\text{nA}$  leakage current**

the use of the SR560 voltage amplifier. This factor rises with further increasing sample resistance, or decreasing level of degradation, respectively. In addition to this essential offset amplification, there is the amplification required to visualise the induced change in resistance. Whereas optical and thermal simulation of the DUT would be necessary to calculate the induced temperature and resistance change, the resistance change is likely to be a fraction of DUT resistance. However, according to Equation 6 a sample with a high ohmic resistance does also generate a high OBIRCH signal.

This leads directly to the limits of thermal laser stimulation techniques when used for SBD defect localisation in high ohmic test structures. A proof of concept of SBD defect detection has been shown. The upper resistance level of detectable defects is limited by the input resistance of the voltage amplifier. With the setup available, a detection of a  $1\text{nA}$  leakage current from a  $20\text{G}\Omega$  DUT was the lowest level of degradation that could be detected. Thus, the detection limit is one order of magnitude lower than that of photon emission microscopy shown in chapter 6.2.2. Furthermore, the influence of the induced thermal energy on the defect development has not been evaluated. On the other hand, as a proof of concept of a SBD detection has been presented, a specially designed voltage amplifier with increased input resistance has the potential to unlock a detection sensitivity that is increased by orders of magnitude. Optical resolution can be improved by using a solid immersion lens.

Finally, with the hardware available, photon emission has proven to be more sensitive than resistance change measurements induced by optical beams. However, a proof of concept and a requirement for further improvements for a SBD defect localisation with OBIRCH is shown.

## 6.5 Physical analysis

Physical analysis of semiconductor devices and test structures is time and cost intensive and is therefore performed on individual devices. This is in contrast to the reliability characterisation, in which numerous devices are electrically stressed and evaluated. The conclusions drawn from reliability characterisations can be traced back to statistical evaluation. In order to conclude characteristics for a structure type with the help of physical analysis, it is essential to guarantee that the analysed samples are representative of the type of analysed structures. Thus, a preliminary electrical characterisation, as presented and discussed in chapter 6.1, is inevitable. There it has been shown that the  $2\mu\text{m} \times 2\mu\text{m}$  structures provide a good electrical reproducibility under a ramped voltage stress (RVS). In addition, with the correct chosen constant voltage stress (CVS) levels, all important characteristic degradation phases of a low  $k$  dielectric can be identified. This chapter will show and discuss the morphological characteristics of representative soft breakdown (SBD) and hard breakdown (HBD) defects created using different electrical stress methods.

The ultra-sensitive localisation methods developed in the framework of this thesis enable the localisation of SBD defects. That permits precise sample preparation for the physical analysis on SBD defects. Sample preparation as well as state of the art defect analysis require specialised tools. These tools can be found at the Fraunhofer IMWS, where the physical analysis shown have been prepared and analysed.

Localisation of a HBD defect within the back end of line (BEOL) is commonly used to localise failures in fully processed integrated circuits. However, a HBD in the BEOL is usually accompanied by a thermal destruction of a larger area around the actual defect. Such a defect within a classically designed metal insulator metal (MIM) BEOL test structure is shown in Figure 59a-b. Figure 59a shows a scanning electron microscopy (SEM) image inclined by  $36^\circ$  from above of the defect and the surrounding area. Figure 59b shows a cross section of this defect. A more detailed description of the preparation of a cross section can be found in chapter 5.6.1.1. The electrical overstress that caused the HBD destroyed the entire test structure and the surrounding volume, including adjacent parts of the probe pad. The extent of destruction becomes clearer when comparing the HBD defect shown with an unstressed sample as shown in Figure 59c-d. A defect characterisation from the HBD shown is no longer possible. The extremely destructive character removed any evidence of the test structure. Electrically, these HBDs result in a high ohmic open or a low ohmic short circuit depending on the redeposition of the remaining materials. It is therefore obviously not possible to derive results about a SBD defect from analysing such a HBD defect. This makes the localisation of a SBD defect inevitable for the physical analysis of SBD defects. But it was not without reason, that the SBD defect localisation was not possible for a long time. MIM structures are literally the worst-case scenario for performing contactless fault isolation for failures occurring in the insulating material. MIM Structures encapsulate the low  $k$  dielectric optically and electrically from the front as well as from the back. The development of metal insulator semiconductor (MIS) test structures by imec enabled SBD localisation as was shown in chapters 6.2 and 6.4.

## 6. Results

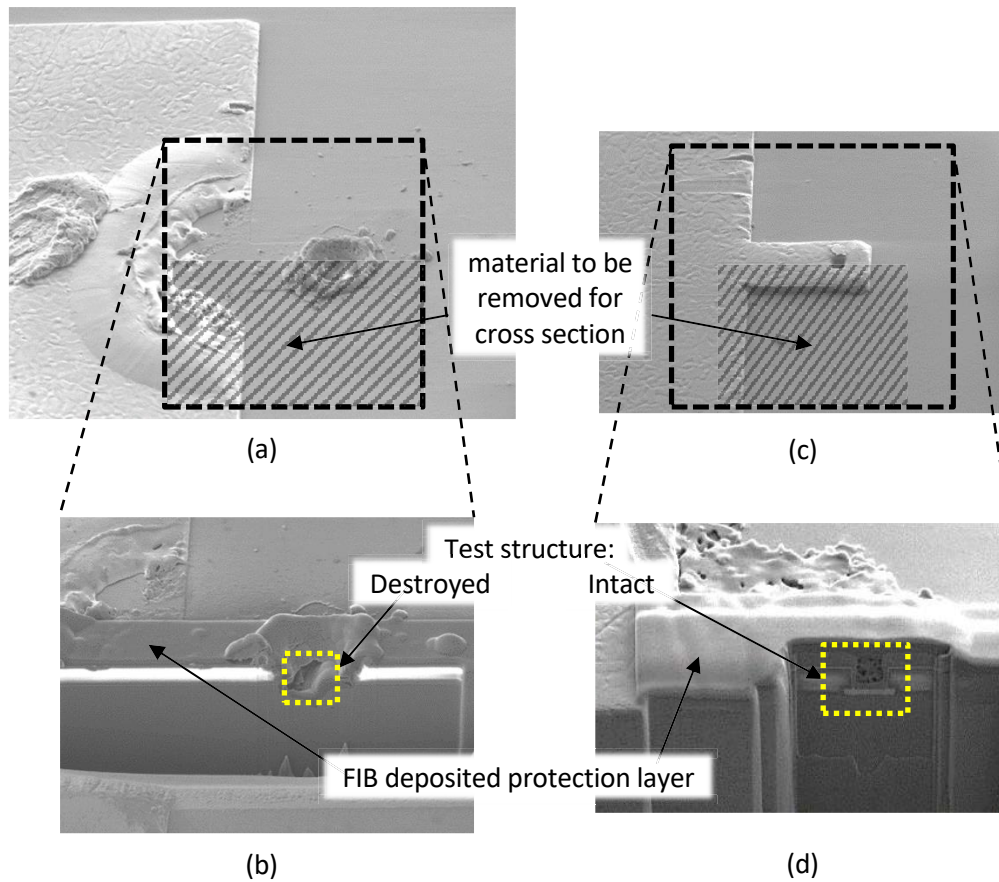
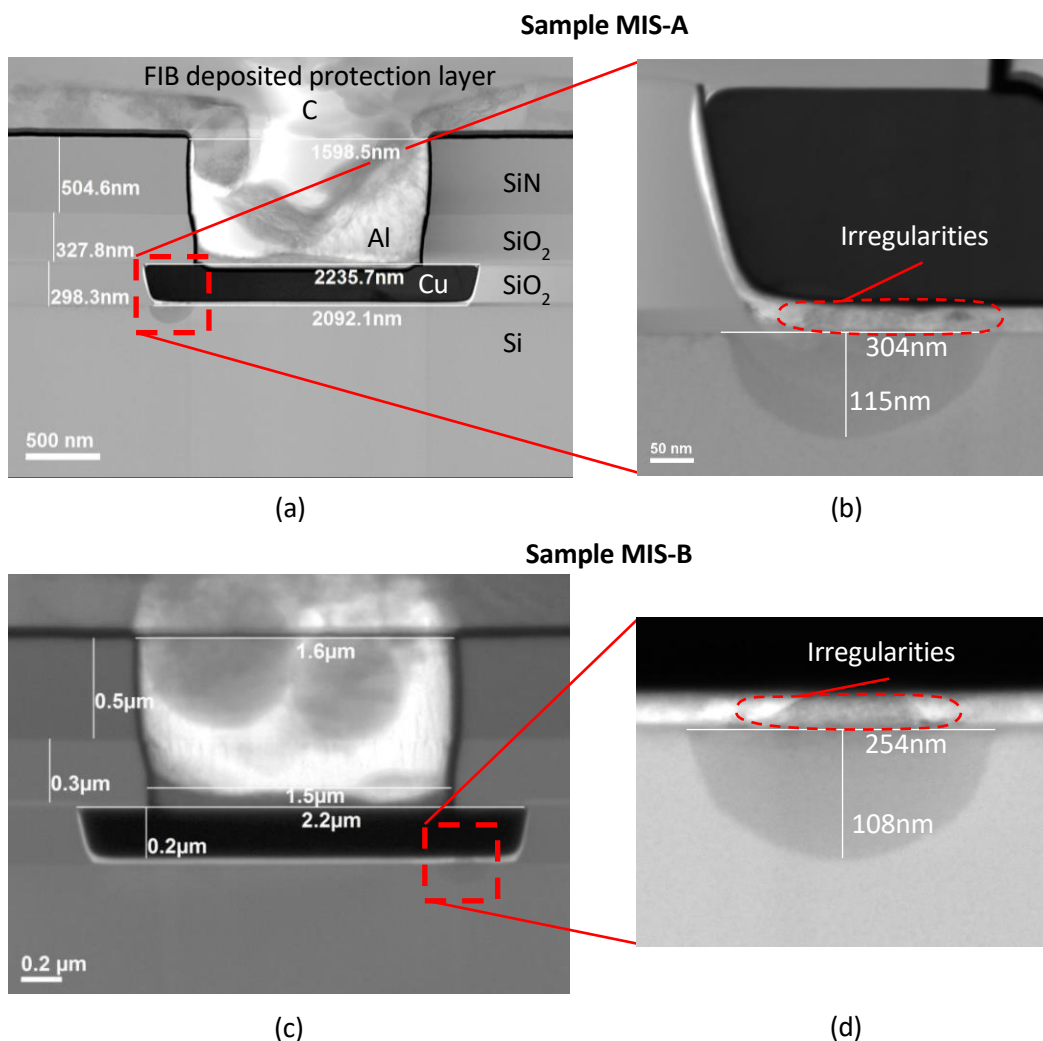


Figure 59: Electron images of: (a) a hard breakdown from a metal-insulator-metal (MIM) test structure; (b) a corresponding cross section image of a MIM hard breakdown; (c) an unstressed MIM test structure; (d) a corresponding cross section image of an unstressed MIM test structure

### 6.5.1 Soft breakdown defects

#### 6.5.1.1 250GΩ / 260GΩ constant voltage stress generated defects

A reproducibly localised degradation level of a soft breakdown defect features a leakage current of 100pA with a sample resistance of  $\sim 250$  GΩ. The localisation has been performed with photon emission microscopy as presented in chapter 6.2.2. Figure 60 shows physical analysis of two soft breakdown defects. The defects shown have a sample resistance of 260GΩ and 250GΩ. An initial transmission electron microscopy (TEM) analysis has been performed on a 1.3μm sample lamella. The bright field scanning TEM image shown in Figure 60 allows identifying a distinct defect area on both defects. The optical analysis of the defect identifies a hemispherical shape within the silicon. With a diameter of 254nm and 304nm and a defect height of 108nm and 115nm, both defects show a similar defect size. The low k dielectric layer above the hemispherical shape show some irregularities that cannot be identified with this analysis. However, the dielectric as well as the copper layer seem to be less affected by morphological changes than the bulk silicon underneath. Further information about the defect morphology can be achieved by thinning



**Figure 60:** Bright field scanning transmission electron microscopy image of a  $1.3\mu\text{m}$  TEM lamella; (a)&(b) from sample MIS-A, a  $250\text{G}\Omega$  soft breakdown defect; (c)&(d) from sample MIS-B, a  $260\text{G}\Omega$  soft breakdown defect

the sample lamellae even more. This increases the visible information of the analysed sample, but on the other hand reduces the depth information. Unfortunately, the defect of sample MIS-A was not centred within the  $1.3\mu\text{m}$  lamella, thus has disappeared during a further thinning step. In any case, the defect of sample MIS-B has been successfully thinned to a remaining lamella thickness of  $100\text{nm}$ . A bright field scanning TEM image as well as a high-angle annular dark field TEM image of this  $100\text{nm}$  lamella is shown in Figure 61. The bright field image of the thinned lamella reveals additional optical details of the defect. Thus, the irregularities identified earlier within the dielectric layer are sharpened and distinct morphological changes can be identified. The Tantalum-Nitride/Tantalum (TaN/Ta) diffusion barrier, in a bright field image visible as a black line that separates the dielectric from the copper layer, is missing locally. The high-angle annular dark field (HAADF) TEM image shown in Figure 61c allows the visualisation of a better material contrast of the defect area. This technique is sensitive to variations in the atomic number, generating a Z-contrast image. Dense materials appear bright in a HAADF image, thus it can be seen that the very dense diffusion barrier is slightly brighter than the copper layer and the porous low k dielectric is comparatively dark. However, a bright area can be identified within the defect area of the low k dielectric. This bright area is likely caused by copper diffusing into the low

## 6. Results

k dielectric layer as well as the silicon underneath. Additionally, the Z-image reveals a clustering of black areas within the low k dielectric layer, indicating an inhomogeneous dielectric. Finally, the smooth appearance of the silicon within the defect hemisphere compared to the roughness of the crystalline bulk silicon is typical for amorphous silicon. The local amorphization of the silicon requires a high energy density, which may result from the leakage current.

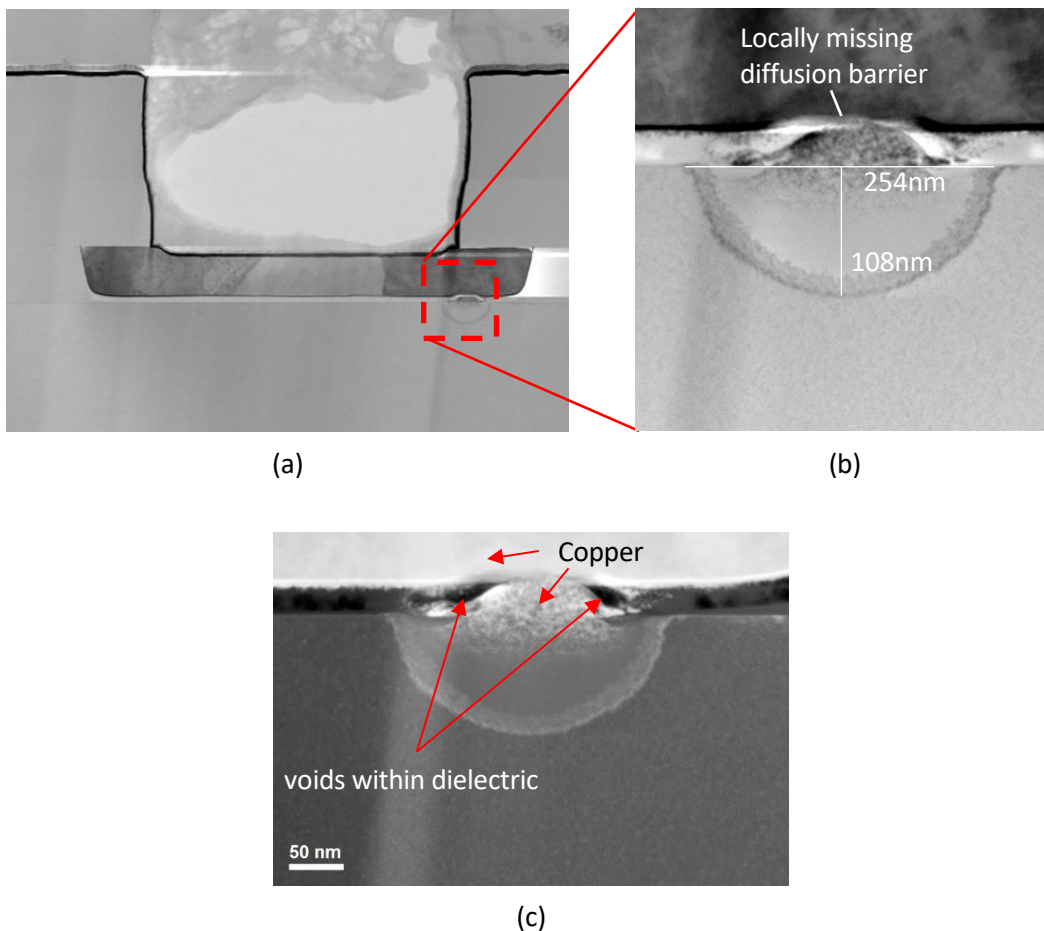


**Figure 61: 100nm TEM lamella from sample MIS-B, a 260G $\Omega$  soft breakdown defect (a) & (b) bright field scanning transmission electron microscopy image; (c) high-angle annular dark field image transmission electron microscopy image**

A spatially resolved elemental analysis of the 100nm thick lamella of sample MIS-B provides further insight into the defect morphology. The scanning energy dispersive x-ray (EDX) analysis is used to measure the elemental distribution within and around the defective area. A mapping of silicon, copper tantalum, and the low k dielectric covers all important layers of the defect. Whereas silicon, copper and the tantalum diffusion barrier can be localised directly with the corresponding elements, the low k dielectric is a chemical compound consisting of silicon, carbon, oxygen and hydrogen. The mapping of the dielectric necessarily requires the detection of multiple elements. The detection of silicon is already used to map the bulk material; this would lead to unnecessary signal overlaps. The low proton number of hydrogen makes it difficult to detect this element with energy dispersive x-ray analysis. In order to map the low k dielectric, oxygen and carbon are used. Figure 62 shows the

elemental mapping of silicon, copper, oxygen, carbon, tantalum and a combined image that contains the different elements. The defect analysis starts with the analysis of the diffusion barrier, shown in Figure 62e. A locally thinned tantalum layer can be identified in the middle of the defect region. Underneath this thinned area, a faint tantalum signal can be measured, spreading out into the low k dielectric. Similar to the tantalum, the copper signal of the defect shows the same conical spreading into the low k dielectric and is shown in Figure 62b. In the region of the thinned tantalum layer, copper spreads into the low k dielectric. The thinned diffusion barrier allowed copper to diffuse downwards. This material movement also transported the tantalum into the dielectric layer. The carbon signal shown in Figure 62d reveals a bright area directly next to the conically spread-out copper and tantalum as well as a carbon signal in the lower part of the dielectric layer. However, these areas were revealed as voids in Figure 61. The low proton number of carbon can result in a false positive detection of the element when analysing voids. Consequently, the mapping of oxygen must support the localisation of the low k dielectric. The oxygen signal shown in Figure 62c indicates that only a fraction of the dielectric layer in the centre of the defect region is intact. The oxygen signal is frayed at the transition to the defect region. Overall, it is likely that the chemical bonds of the low k dielectric have been broken inside the defective area. A mapping of silicon is shown in Figure 62a, a different signal intensity can be seen from the bulk silicon and the defect hemisphere, previously identified as amorphous silicon. This indicates a different crystal structure or different lamella thickness in both areas. However, a spherically reduced lamella thickness is unlikely, and the effect of a reduced lamella thickness can be observed on the left side of the hemispherical defect. A sample lamella is polished top down with a focused ion beam and the process may cause such a vertically separated lamella thickness to occur. Furthermore, a faint signal can be measured at the position of the dielectric layer, detecting the silicon content from the dielectric chemical compound. A comparably strong silicon signal can be measured at the position of the tantalum diffusion barrier, but without a physical reason of an increased silicon content at this location. At 1.709keV, the spectral M-line of Tantalum is located close to the spectral K line of Silicon (1.740keV). This minor energetic difference cannot be resolved by EDX.

Concluding, a combination of an optical bright field image, a Z-contrast image generated by a high-angle annular dark field measurement and a chemical analysis by means of energy dispersive x-ray analysis creates a detailed picture of the analysed  $260\text{G}\Omega$  defect. A defect with a diameter of 250nm has been analysed. From the results shown, it can be said that a thinned tantalum diffusion barrier started the degradation process. However, at this point the root cause of the thinned diffusion barrier cannot be identified.

## 6. Results

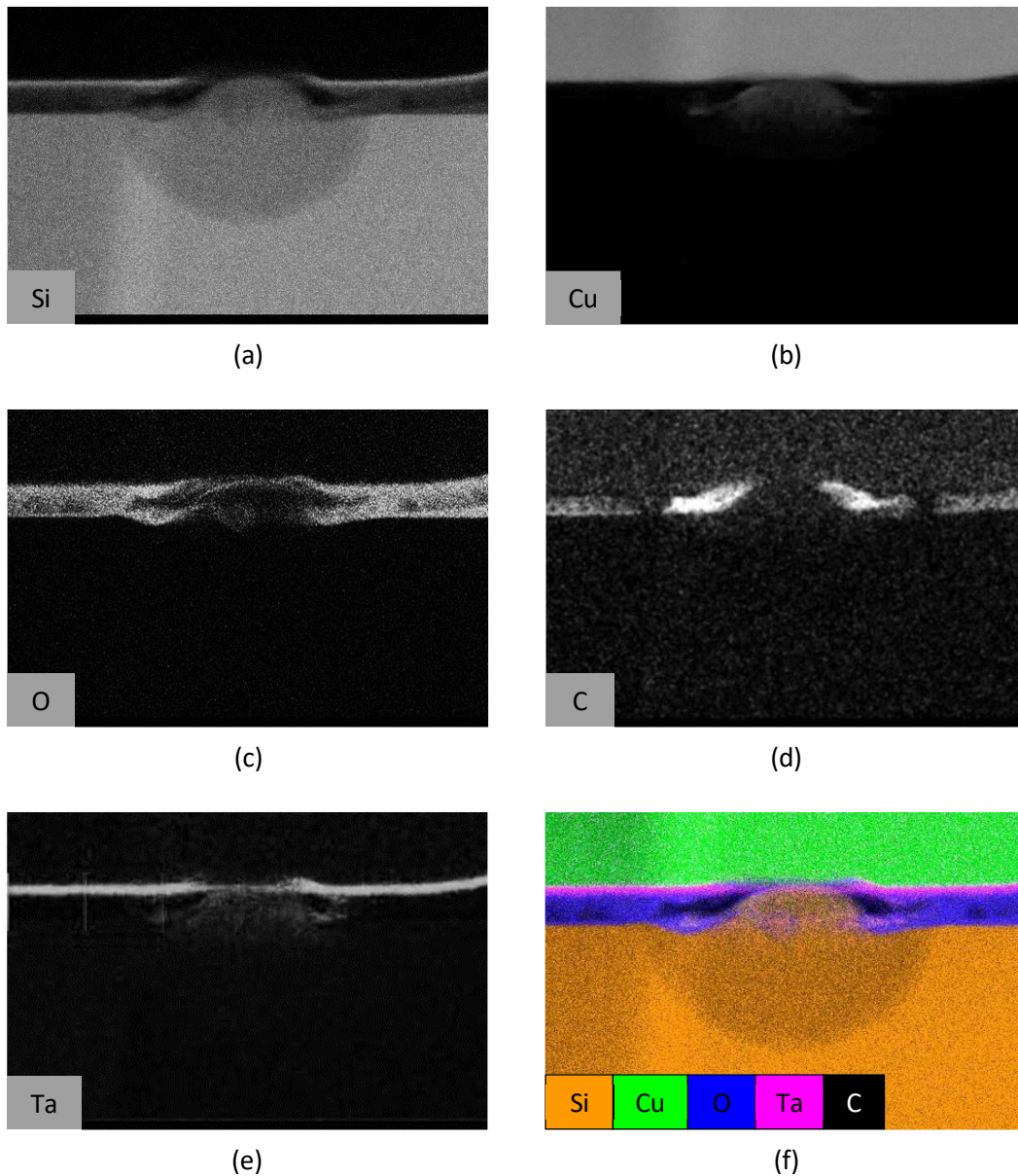


Figure 62: Elemental mapping with energy dispersive x-ray analysis of a 100nm lamella of soft breakdown sample MIS-B. Shown is (a)Silicon (b)Copper (c)Oxygen (d) Carbon (e)Tantalum (f)an overlay of all elements shown

### 6.5.1.2 307GΩ ramped voltage stress generated defect

The previous chapter has shown two defects that were generated with a constant voltage stress and a current compliance of 100pA. Both defects show a similar defect morphology and size and one of these defects was analysed in detail. During the development of SBD defect localisation techniques, a ramped voltage stress with a current compliance was evaluated electrically in chapter 6.1.4, and localised SBD defects were presented in chapter 6.2.2.2. A detailed physical and chemical analysis of a defect that was generated with a ramped voltage stress and a current compliance of 100pA is shown in Figure 63. In order to

perform the analysis, a 500nm thick sample lamella was prepared. An overview of the defect position as well as the defect itself can be seen on the high angle annular dark field images shown in Figure 63(a-b). The defect can be divided into two distinct defect shapes: first a hemispherical shape with a diameter of 277nm and a defect width of 129nm. The second part of the defect is a spherical cap with a defect height of 88nm and diameter of 416nm. The overall defect width is therefore about 540nm. A chemical analysis with energy dispersive x-ray analysis allows to map the different elements within the defect. Similar to the previously analysed defects, a mapping of silicon, copper, oxygen, carbon and tantalum represents all the important layers of the defect. However, compared to the chemical analysis shown in chapter 6.5.1.1, the signal intensity as well as the resolution are slightly reduced due to the thicker sample lamella and the increased measurement area, or defect area respectively. The hemispherical part of the defect shows the same defect dimensions as the defects generated by a constant voltage stress. Detailed elemental mapping also supports the similarity of hemispherical defects. No tantalum signal can be measured in the middle upper part of the hemispherical defect. A lack of massive copper diffusion in this area indicates that the tantalum layer is still intact, but extremely thinned and not measurable anymore with the reduced sensitivity. Furthermore, silicon migration through the area of the locally thinned tantalum can be measured. The localisation of the low k dielectric layer with the mapping of oxygen and carbon is only partially possible this time. What can be seen is a locally extremely weak oxygen signal in the region of silicon migration; whereas the carbon signal is too noisy to draw any conclusions from it. However, compared to the 100pA leakage current defect generated by CVS, the high angle annular dark field image shows some copper impurities in the upper part of the hemispherical defect region. These impurities have not been recorded by chemical analysis but later analysis with a higher resolution have identified this type of impurities as copper.

Overall, the hemispherical part of the defect generated by ramped voltage stress and the defect generated by constant voltage stress previously presented show a similar characteristic. However, the additional spherical cap-shaped part of the defect reveals a completely different defect morphology. First, the tantalum diffusion barrier is mostly intact in this region but bended downwards into the dielectric layer, as is the copper layer. A direct comparison of the oxygen signal from the intact part of the dielectric layer and the spherical cap shows that the dielectric layer is mostly intact in the defect region but is thinned and bended downwards. This thinned area is filled with silicon, which pushes upwards into the low k dielectric.

## 6. Results

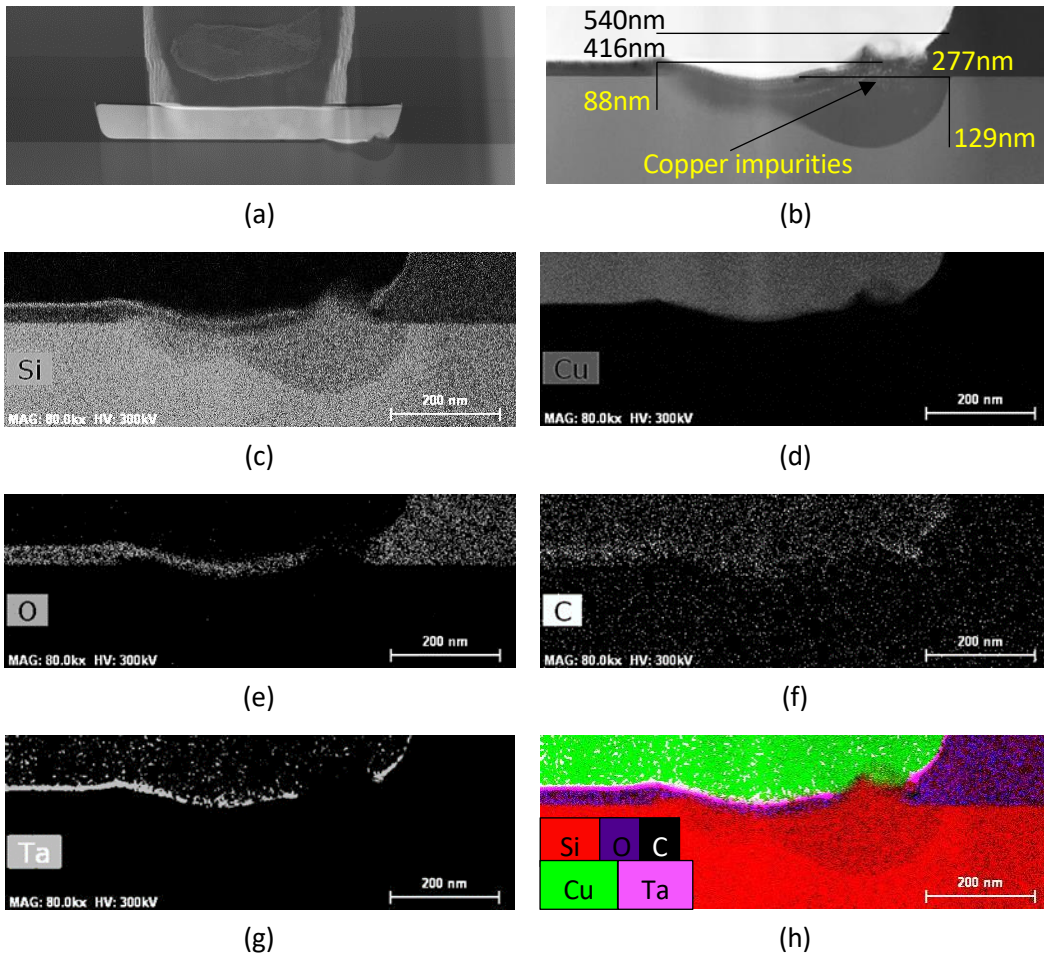


**Figure 63: Energy dispersive x-ray analysis of a defect generated by ramped voltage stress with a current compliance of 100pA**

Chapters 6.1.2 and 6.2.2.2 showed that an increased voltage stress above 30V generates an additional initial leakage current. As shown in 6.1.4, this voltage stress level is exceeded by a ramped voltage stress and a current compliance of 100pA. However, a defect with a 100pA leakage current that was generated with a constant voltage stress and a defect with a 100pA leakage current that was generated with a ramped voltage stress show similar hemispherical defect shapes. In addition, the overvoltage that occurs at the ramped voltage stress generates an additional spherical cap-shaped defect that acts as an additional defect path and thus adds an additional leakage current. However, this defect is not necessarily the defect that evolves into a hard breakdown.

Concluding, a ramped voltage stress generates a completely different defect morphology compared to a defect generated by constant voltage stress. Whereas it is possible to identify similar parts from both defects, it should be carefully evaluated which material or device parameters can be extracted from a ramped voltage stress measurement. For the analysis of a soft breakdown defect, it has been shown that this stress method is not suitable.

### 6.5.1.3 3.47TΩ ramped voltage stress generated defect

The previous chapter has shown that a ramped voltage stress (RVS) generated defect is not representative of defects from accelerate degradation experiments to determine the live time. However, a defect with a 10pA current compliance has only been localised by a RVS rather than a constant current stress (CVS). Physical analysis of such non-representative defects is of interest as the defect resistance is an order of magnitude higher than these localised and physically analysed representative defects. Furthermore, the previous chapter showed similarities between both types of defects.

Figure 64 shows a bright field transmission electron microscopy image of a 1.8 $\mu\text{m}$  thick sample lamella of a RVS generated defect with a current compliance of 10pA. The identification of two defect areas as typical for RVS generated defects is possible. The hemispherical part is 147nm high and 282nm wide. The spherical cap can be identified with a height of 78nm and a width of 242nm. A lamella thickness of 1.8 $\mu\text{m}$  offers a comparatively large interaction volume, which significantly reduces the level of detail of the image.

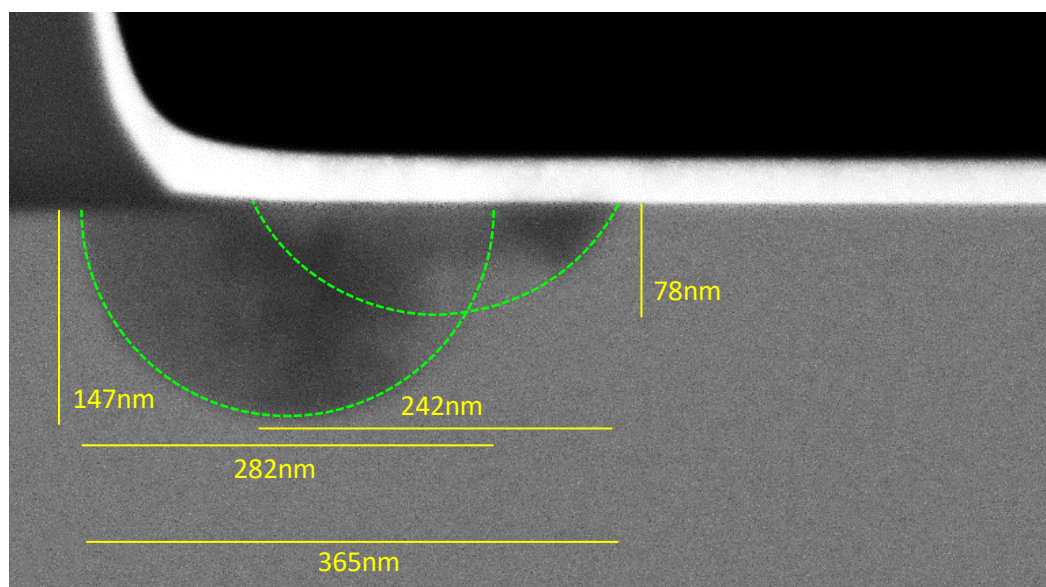
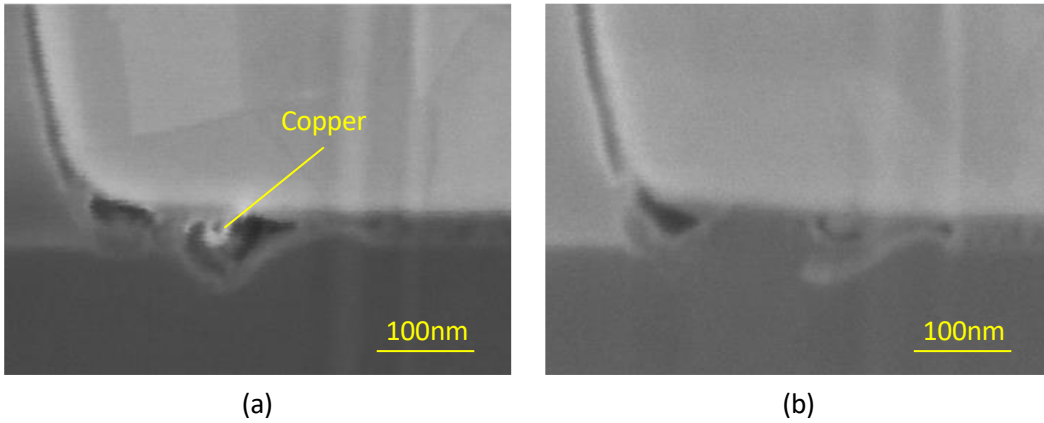


Figure 64: Bright field transmission electron microscopy image of a 1.8 $\mu\text{m}$  thick sample lamella from a defect generated by ramped voltage stress with a current compliance of 10pA

The sample lamella has been gradually thinned in order to reduce the interaction volume, or increase the level of details, respectively. An in-lens detector of the focused ion beam is used to monitor the defect during the thinning steps. These in-lens detectors show significantly fewer details compared to a transmission electron microscope. However, transferring the lamella into the TEM system after each thinning step is not practicable. Due to the thinning and the poorer quality of the FIBs in-lens detector, it can be challenging to identify the correct defect centre. Although a detailed chemical analysis of the defect has been performed on a sample lamella thinned up to 500nm, it has been found that the centre of the defect was removed during the thinning steps. Figure 65 shows two in-lens images from thinning steps number nine (Figure 65a) and eleven (Figure 65b).

## 6. Results

The defect height in the bulk silicon is higher in Figure 65a than in Figure 65b. Furthermore, Figure 65a shows copper diffusing downwards. In coherence with the other physically analysed defects shown, copper diffusion can be identified in the defect centre, supporting the assumption that thinning step nine showed the defect centre. However, this has been found after the sample was thinned, and thus a chemical analysis had been performed on a further thinned sample lamella.



**Figure 65: In-lens detector image at different sample lamella thinning steps (a) thinning step number nine; (b) thinning step number eleven**

Figure 66 shows the detailed chemical analysis of further thinned the sample lamella. The HAADF image reveals that the defect dimensions have shrunk compared to the analysis from the 1.8 $\mu\text{m}$  thick lamella. The tantalum and the copper layer are also fully intact. The previous physical analyses had shown that the defects spread conically from a locally thinned tantalum layer into the dielectric and the silicon.

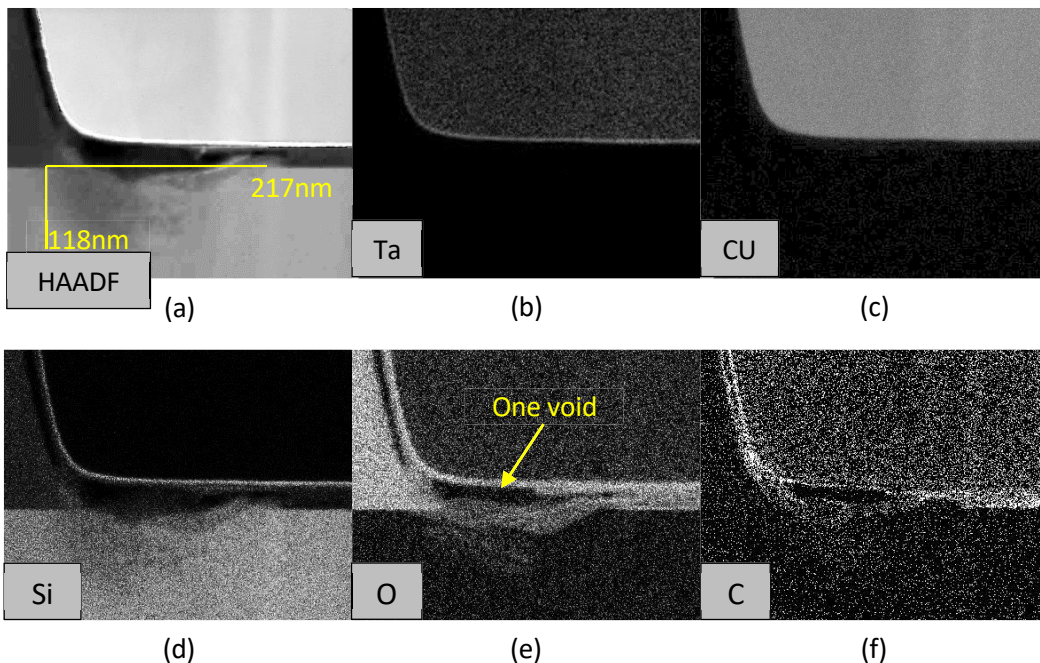


**Figure 66: Energy dispersive x-ray analysis of a 0.5 $\mu\text{m}$  thick sample lamella from a defect generated by ramped voltage stress with a current compliance of 10pA**

Even though the defect centre was removed during the preparation of the sample lamella, the information obtained from this non-centred detailed physical analysis is of high value as it increases the understanding of the 3D defect morphology of the analysed SBD defects. Despite no irregularities can be found inside the tantalum and copper layer, the silicon and low k dielectric layers show similarities to the hemispherical defect shapes discussed previously. This includes a void in the upper region of the low k dielectric layer and the fringed oxygen signal. This allows a 3D reconstruction of the defect morphology to be estimated, as shown in Figure 67. A locally thinned diffusion barrier enables copper to diffuse into the low k dielectric and further down into the silicon. Within the dielectric layer and around the copper diffusion, a ring of voids is developed.

Concluding, even though the ramped voltage stress has been previously identified as a non-suitable technique for generating representative soft breakdown defects, the analysis of the hemispherical part of these defects shows important morphological similarities to representative soft breakdown defects. The sample lamella analysed in this chapter provides additional depth information, which is caused in particular by thinning the sample beyond the defect centre. The voids found on either side of the defective tantalum layer in chapter 6.5.1.1 are joining each other in Figure 66. This leads to the conclusion that a circular void area within the dielectric layer surrounds the area below the region of the thinned tantalum.

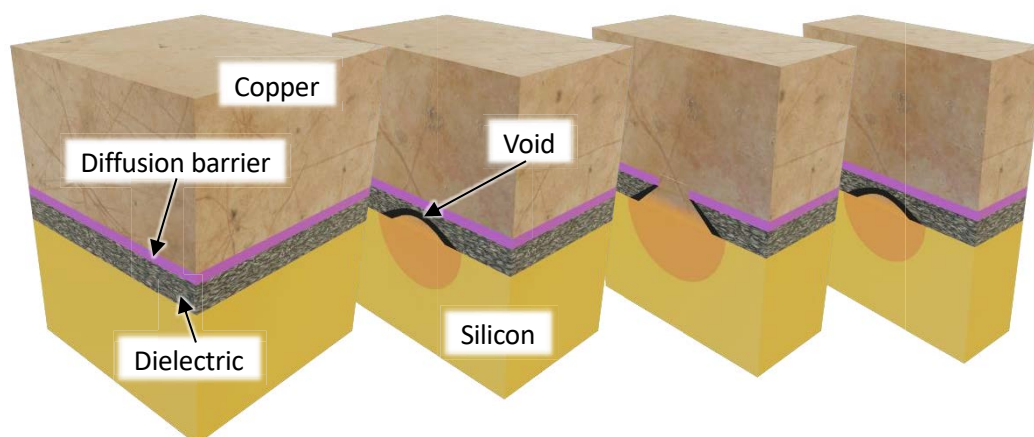


Figure 67: Estimated 3D model of a soft breakdown defect within a low k dielectric metal insulator semiconductor test structure

### 6.5.2 Hard breakdown defects

The detailed physical analysis of previously localised soft breakdown (SBD) defects on area test structures gave a first impression of the defect development. This was possible due to the development of low k dielectric metal insulator semiconductor (MIS) test structures by imec. Another advantage of this type of test structure is the hard breakdown (HBD) behaviour. Whereas classic dielectric test structures are designed as a material stack made of metal insulator metal (MIM), HBD behaviour is usually accompanied by massive destruction of a larger area around the defect. The HBD behaviour of the utilised MIS

## 6. Results

structures is far less destructive than that of similarly processed MIM test structures, which are shown in Figure 59.

The native oxide that separates the bulk silicon from the dielectric layer adds series resistance to the vertical current flow through the structure. During SBD condition, the additional resistance is negligible compared to the high resistance of the low k dielectric. During an HBD, however, the native oxide acts as an internal current compliance that limits the extent of destruction. As can be seen in chapter 6.1, the MIS HBD remains in the region of  $k\Omega$  instead of an electrical open or short circuit. This makes it possible to analyse different levels of degradation during a HBD.

### 6.5.2.1 $4k\Omega$ hard breakdown defect

Figure 68 shows a dark field image of a 500nm TEM lamella from a HBD defect that was generated with a constant voltage stress and a current compliance of 1mA. The remaining sample resistance is  $4k\Omega$ . The destructive character of this HBD defect is limited to an enclosed defect area rather than showing a massive destruction as a HBD of MIM structures (Figure 59). The test structure itself remains intact after the hard breakdown. However, significant morphological changes can be identified in the defect region. The structure shows a local degradation over several 100nm within the copper, low k dielectric and the silicon layer. The structural defects within the silicon can be classified in a hemisphere with a diameter of approximately 400nm and many crystal defects outside the hemisphere that run up to more than 750nm into the silicon. The SBD defects analysed previously had shown a silicon hemisphere as well, however, this time the hemisphere is filled with a filigree pattern.

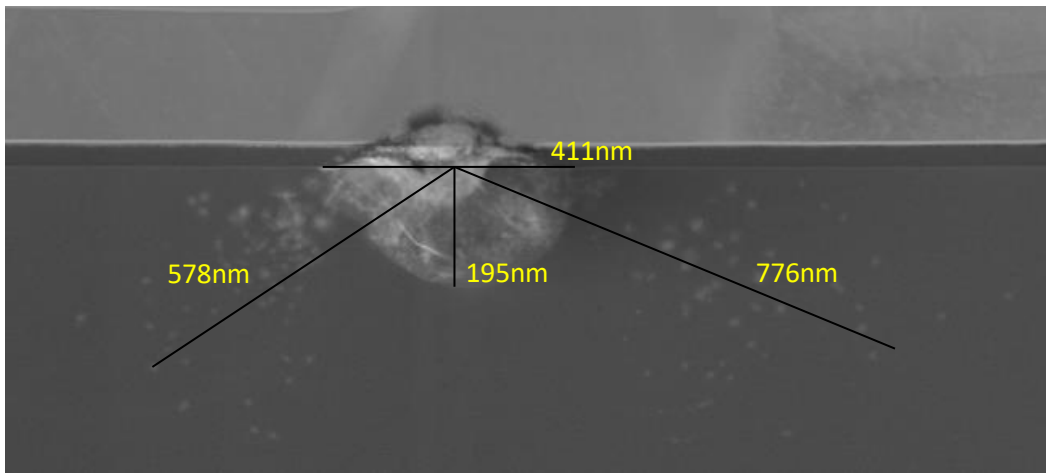


Figure 68: Dark field transmission electron microscopy image of a  $4k\Omega$  hard breakdown defect

A spatially resolved elemental analysis provides further insight into the defect morphology. Figure 69 shows a scanning energy dispersive x-ray mapping for silicon, copper, tantalum, oxygen and carbon as well as a Z-contrast (HAADF) image of the scanned area. The tantalum diffusion barrier is missing locally around the defect centre. Thus, a strong electro-thermal driven interdiffusion between copper and silicon can be observed. Mostly copper diffuses in silicon, hence the complete defect centre shows a massive copper concentration. The

filigree structuring inside the defective silicon hemisphere identified earlier can be verified as recrystallised copper. Additionally, Figure 69d shows a tantalum clustering in the middle of the defect. A clustering of silicon can be identified at the same origin. It has been discussed previously that silicon and tantalum share some peaks of their characteristic x-ray spectra. At this point it is impossible to reliably identify the material of the cluster formation in the defect centre. The defective silicon hemisphere still shows signs of amorphization between the massive copper structuring. The low k dielectric layer represented by the mapping of oxygen and carbon is tattered in the defect region but bends more into the

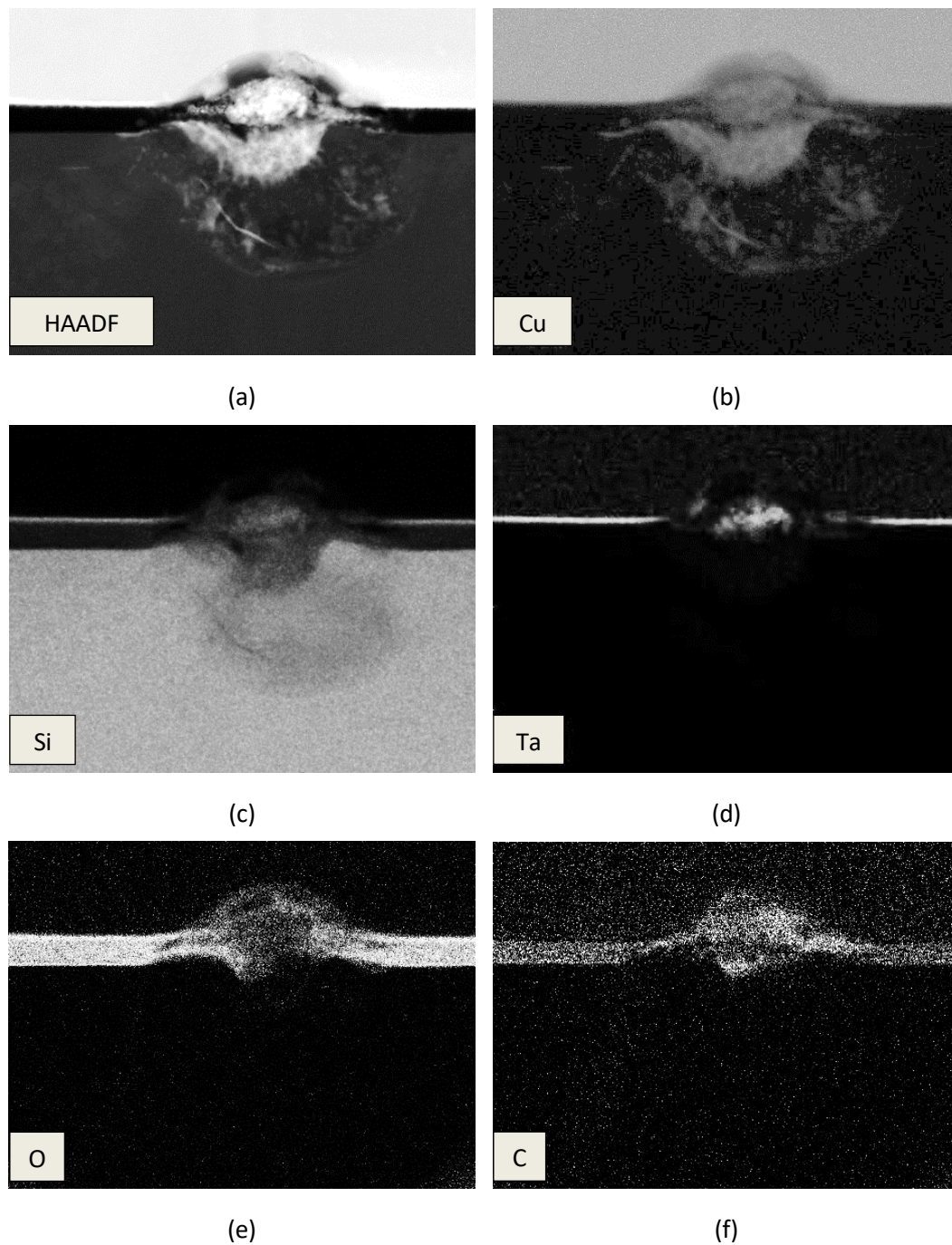


Figure 69: Energy dispersive x-ray analysis of a 4k $\Omega$  hard breakdown

## 6. Results

copper than into the silicon layer. Altogether, the copper layer is less affected than the silicon underneath. The massive recrystallised copper inside the silicon is likely the reason for the low ohmic leakage path. However, the massive copper diffusion is missing a low ohmic bottom electrode to create an electrical short. Thus, the internal series resistance limits the current, the destruction during the HBD, respectively. This gives the opportunity to analyse HBD defects with different levels of current compliances in detail. As will be shown later, the in-depth analysis of different HBD is required to develop a better understanding of the SBD defect morphology presented in the previous chapter 6.5.1.

### 6.5.2.2 312k $\Omega$ hard breakdown defect

Chapter 6.5.1 analysed SBD defects with defect resistances  $\sim 200\text{G}\Omega$ . Chapter 6.5.2.1 analysed a HBD defect with a defect resistance of a few k $\Omega$ . As an intermediate level of degradation, this chapter discusses a defect generated by constant voltage stress with a current compliance of  $1\mu\text{A}$ . According to the electrical characterisation as well as the results of spectral photon emission, the sample resistance of  $312\text{k}\Omega$  is classified as a HBD. Figure 70 shows an HAADF image of the defect. The defect combines morphological characteristics from the analysed SBD defects as well as from the previously analysed HBD defect. A hemispherical shape with a diameter of about  $400\text{nm}$  pointing into the substrate, and a filigree structuring of copper inside this hemisphere can be identified in both HBD defects. Compared to the analysed SBD defect, the dimension of the hemisphere is increased, but the part of the hemisphere that is not filled with filigree copper structuring is more similar to the amorphous silicon hemisphere from the analysed SBD. The intact tantalum and copper layers as well as a larger void that can be found inside the dielectric layer indicates that the centre of the defect has been removed during the preparation of the sample lamella. This effect has been discussed in chapter 6.5.1.3. At this point, a further chemical analysis has not been performed, as the different morphological characteristics of the defect shown in Figure 70 can be identified with the help of the previously chemically analysed defects.

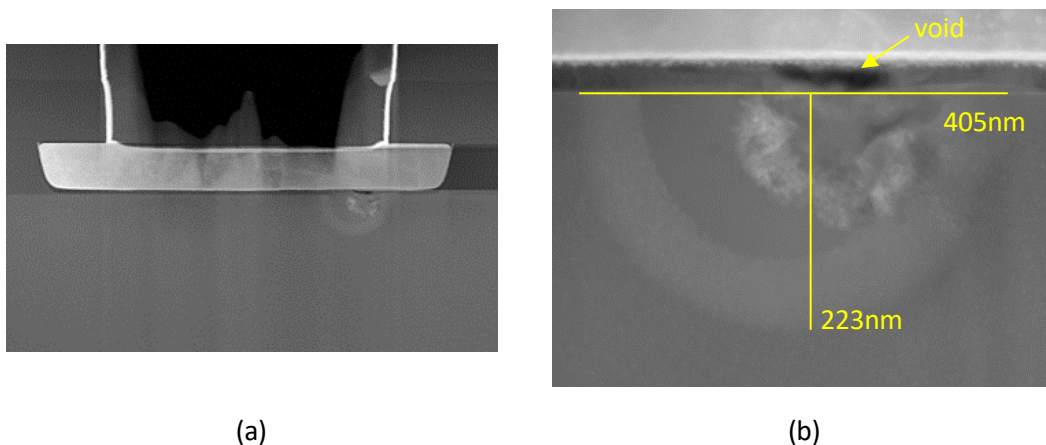
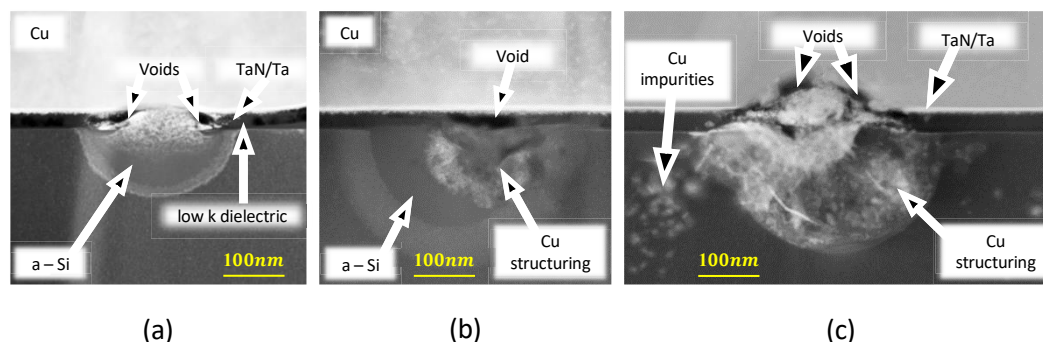


Figure 70: High angle annular dark field transmission electron microscopy image of a  $314\text{k}\Omega$  hard breakdown defect

### 6.5.3 Defect development

A detailed physical analysis of SBD defects with a defect resistance of  $\sim 200G\Omega$  was shown in chapter 6.5.1.1. With the additional physical analysis of two different HBD degradation levels shown in 6.5.2, it is possible to give a first impression of the defect development. Figure 71 shows HAADF images of the three different states of degradation. All three defects have been discussed in detail in the previous chapters. However, the defect growth becomes clearer with this summarising figure. A hypothesis of the defect development during SBD and HBD in MIS low k dielectric test structures is given below.

During the SBD development, a defective hemisphere expands inside the silicon substrate. The defect centre is characterised by a thinned tantalum diffusion barrier, from which the defect develops conically into the dielectric and silicon layer. The point of entry of the copper into the dielectric layer is joined by adjacent voids. Furthermore, this entry point is likely surrounded by a circle of voids. Such defects are linked by a locally increased electrical field strength as well a locally increased current density. These two can break the chemical bonds of the low k dielectric. This facilitates material transportation in the defect region and improves void growth [46]. The growth of the defect hemisphere as well as the thinning of the tantalum layer and the copper diffusion continue to progress during further SBD degradation. In HBD, the defect growth stops and a massive electrothermally driven copper-silicon diffusion starts. Thus, the defective hemisphere fills with copper, which recrystallizes as filigree structuring. At this point, the tantalum diffusion barrier must be missing locally to enable such a massive copper diffusion. Without a current compliance, this recrystallization process fills the defective hemisphere nearly immediately. With the help of a current compliance, intermediate levels of this recrystallization process can be analysed. So, a feasible defect development can be extracted from the physical analysis shown.



**Figure 71: HAADF images of different 100nm thick sample lamellae: (a) a 260kΩ soft breakdown defect; (b) a 312kΩ hard breakdown defect; (c) a 4kΩ hard breakdown defect**

Finally, the relatively large defect areas suggest a much lower sample resistance, especially during the SBD defect development. A possible hypothesis is based on the native oxide layer that isolates the silicon from the dielectric layer. Breuer [46] had discussed that chemical bonds can break during the high electrical field stress of a constant voltage stress. The native oxide thus provides additional oxygen that can be released during the defect development. This oxygen, as well as oxygen derived from broken bonds within the low k dielectric layer, can create a semi-isolating layer at the edge of the defect hemisphere. The increased current density at the defect can considerably heat up the defect volume. Thus, the oxygen can react with copper to create semi-isolating copper oxide or with silicon to create isolating silicon oxide. The oxidation of copper into copper dioxide requires temperatures from 300°C

## 6. Results

– 800°C and the oxidation of silicon 800°C – 1200°C. Figure 71c shows that copper impurities find their way out of the defect hemisphere at the silicon-dielectric interface rather than at the bottom of the defect. These copper impurities are electrothermally driven into the silicon so that they can be considered as a current flow map.

## 6.6 Thermal modelling

The physical analyses of soft breakdown (SBD) defects in low k dielectric test structures, which were discussed in detail in the previous chapters, gave a first impression of the defect development within the analysed MIS test structures. However, the same physical analyses showed morphological characteristics that are not straight forward explainable. Although it has been shown that the defect dimensions increase with an increasing level of degradation in SBD, the overall defect dimensions are large compared to the sample resistance. The chemical bonds of the low k layer can break due to the high electrical field [46]. A hypothesis explaining the high ohmic resistance of the defects was given earlier. It is stated that the free oxygen reacts with copper or silicon in order to build an insulating layer at the border of the defect hemisphere and thus build up a semi-insulating layer. The chemical reaction of copper and oxygen requires temperatures of 300°C – 800°C and the oxidation of silicon requires temperatures as high as 800°C – 1200°C. The hemispherical defect shape of amorphous silicon supports the occurrence of high temperatures. The transformation from crystalline silicon into amorphous silicon takes place during recrystallisation. The chemical analysis of the defect showed that the defect hemisphere contains copper. The liquidus temperature for an alloy of silicon and copper is reduced to that of the two individual materials. The silicon-copper phase diagram can be seen Figure 72 [47]. The minimum required liquidus temperature of 806.4°C is reached for a specific silicon atomic percent rate of 31.2.

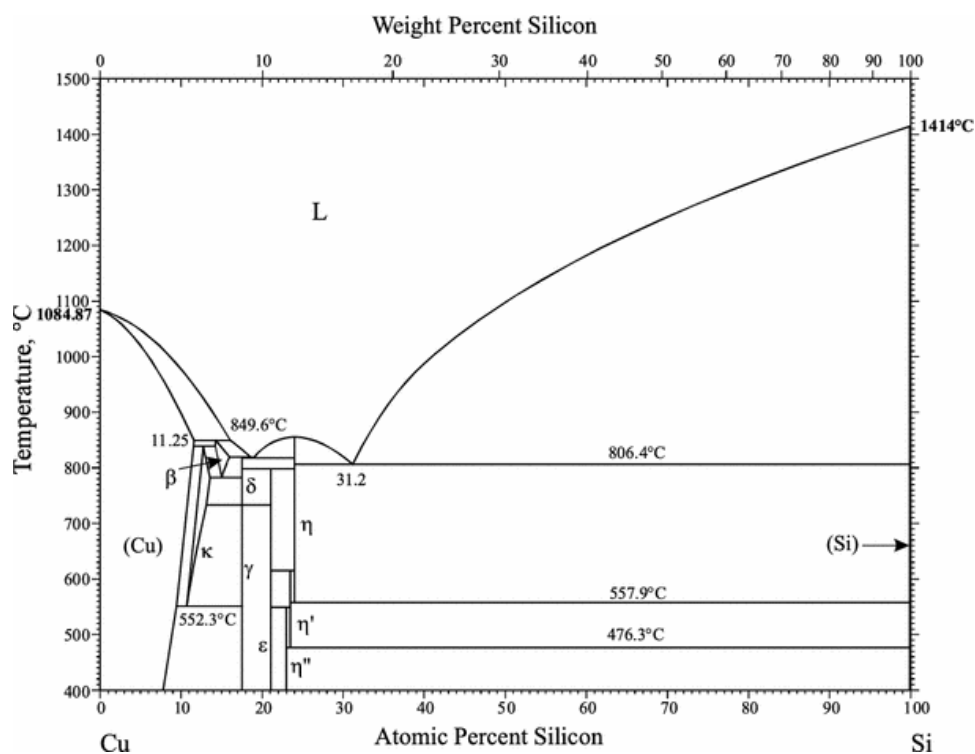


Figure 72: Silicon - Copper phase diagram

Even though chemical analyses of the SBD defects did not allow a relative elemental distribution to be specified, it was evident that the lower part of the amorphous defect hemisphere contains only a small amount of copper. The temperature that occurred was likely higher than 806.4°C.

## 6. Results

Nanoscale amorphization of silicon is discussed in [48]. The authors used a pulse femtosecond laser to locally melt crystalline silicon, the silicon recrystallising with an amorphous crystal structure. The power density applied was approximately  $\sim 1E17$   $\mu\text{W}/\mu\text{m}^3$ .

A thermal simulation of the physically analysed defects will enrich the understanding of the morphological results shown.

### 6.6.1 Defect modelling

ANSYS, a numerical solver program, is used to create a simplified 3D model of the analysed test structure. The model created consists of the layers and material parameters described in Table 3.

Layer / Material	Dimensions (width x depth x height)	Thermal Conductivity $\left[\frac{W}{m \cdot K}\right]$	Thermal capacitance $\left[\frac{J}{kg \cdot K}\right]$
Bulk silicon	700 $\mu\text{m}$ x 700 $\mu\text{m}$ x 100 $\mu\text{m}$	163	703
Low k dielectric	2 $\mu\text{m}$ x 2 $\mu\text{m}$ x 40nm	0.1	920
SiO <sub>2</sub>	700 $\mu\text{m}$ x 700 $\mu\text{m}$ x 490 $\mu\text{m}$	1.2	750
Copper	2 $\mu\text{m}$ x 2 $\mu\text{m}$ x 250 $\mu\text{m}$	400	385
Aluminium	450 $\mu\text{m}$ x 450 $\mu\text{m}$ x 350 $\mu\text{m}$	235	897

Table 3: Layer parameters used for the thermal model

At an early stage of degradation, it can be assumed that the externally applied voltage is consumed by the dielectric layer. Furthermore, as soon as a leakage path develops, the leakage current focuses on the path of the reduced resistance, or the defect, respectively. In order to simulate the power consumption of the system, an internal power source is implemented in the low k dielectric layer at the origin of the localised defect. The implementation of a circular defect in this small defect dimension cannot be realised, thus the defect is simulated as cuboid with a variable size.

In particular, the defect shown in Figure 61 was simulated. The power consumption of this defect was calculated from the corresponding i-t graph shown in Figure 44. The defect size was modelled with 200nm x 200nm. A cross section of the created model is shown in Figure 73.

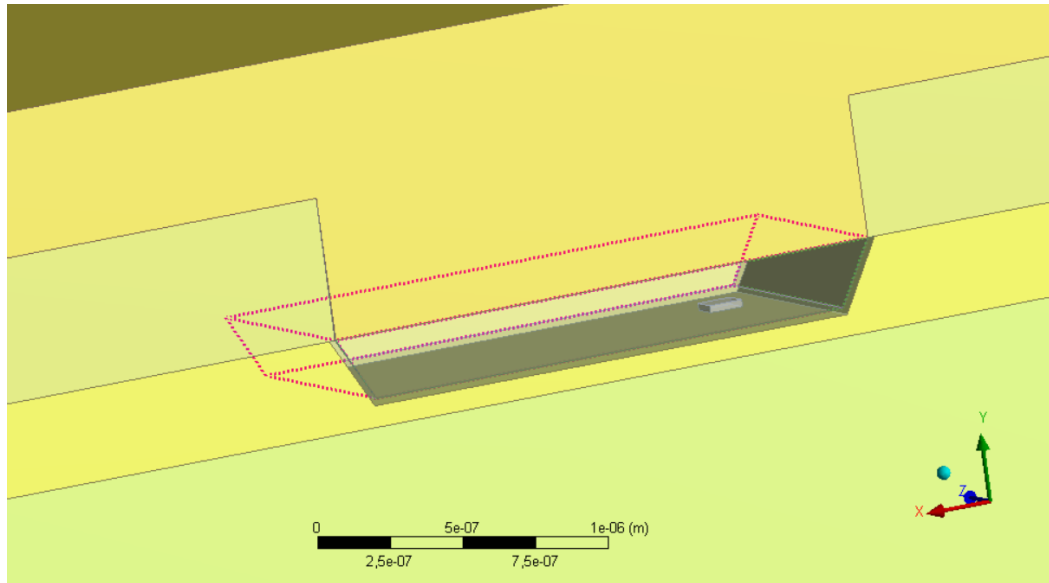


Figure 73: Cross section of the created 3D model used to simulate the thermal conditions during the soft breakdown defect development

### 6.6.2 Modelling results

A steady state analysis of the thermal conditions was performed with the parameters listed above. The power density of the simulated defect was calculated from the i-t degradation curve and was determined to be  $\sim 10^{12} \text{ W}\cdot\text{m}^{-3}$ . With this power density, the defect area heats up less than  $2^\circ\text{C}$ . The heat evacuation capability of the system exceeds the heat generation. An analysis of the heat flux has shown that the copper layer is transporting most of the heat. Due to the lower thermal conductivity of the aluminium layer on top of the copper, the copper / aluminium interface is subject of a discontinuity.

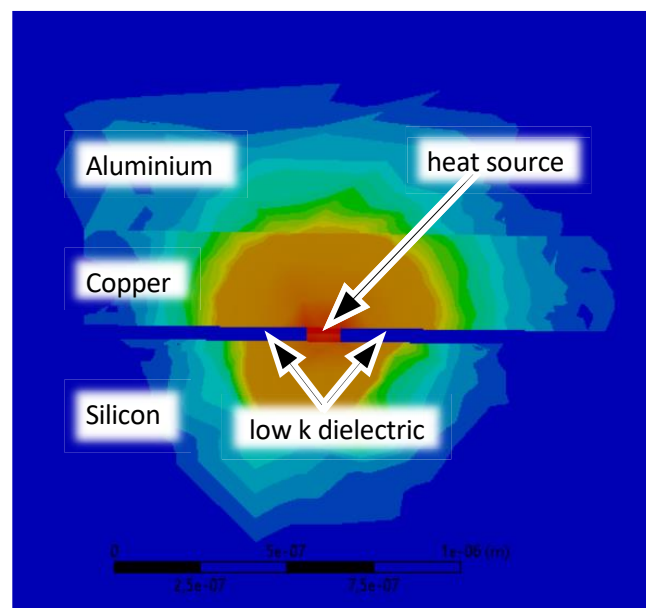
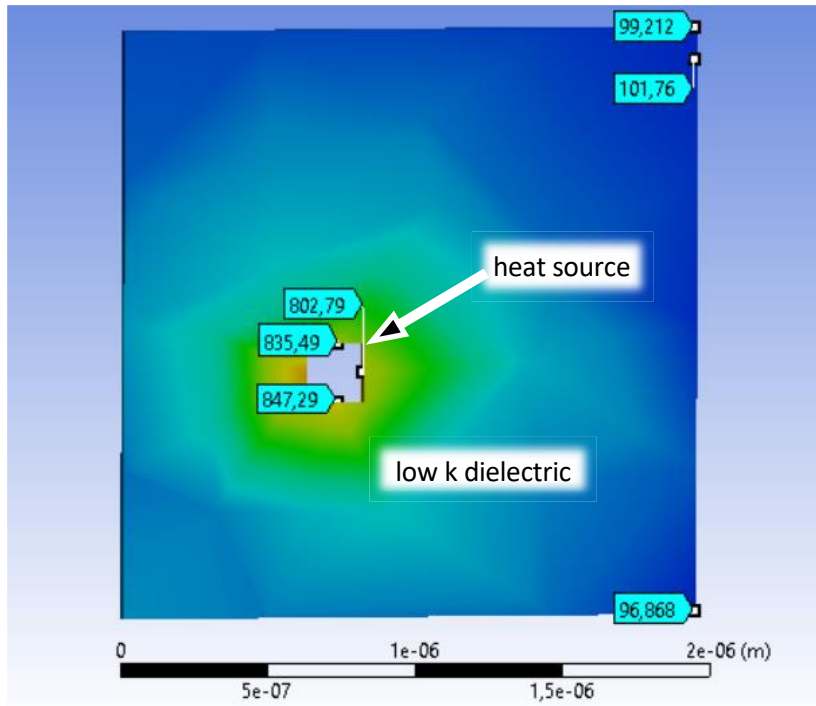


Figure 74: Cross section of the heat flux from the simulated test structure

## 6. Results

A variation of the simulated power density showed that there is a sweet spot for the power density applied. A simulated defect power density of  $5 \cdot 10^{13} \text{ W} \cdot \text{m}^{-3}$  results in a defect area heating less than  $2^\circ\text{C}$ . On the other hand, simulated power densities equal or larger than  $6 \cdot 10^{13} \text{ W} \cdot \text{m}^{-3}$  result in a significantly increased, but constant heat distribution of the defect area in relation to the simulated power density. The steady state analysis shows temperatures of  $847^\circ\text{C}$  within the simulated defect. A top view of temperature distribution on the low k dielectric can be seen in Figure 75. An internal defect temperature of  $847^\circ\text{C}$  would enable the chemical oxidation of copper and silicon as well as the local amorphization of a silicon-copper-alloy.



**Figure 75: Top view of the low k dielectric and its surface temperature distribution. Temperature distribution similar for applied power densities of  $6 \cdot 10^{13} \text{ W} \cdot \text{m}^{-3} - 1 \cdot 10^{15} \text{ W} \cdot \text{m}^{-3}$**

Even though the power density required to heat the structure differs by one order of magnitude from the power density calculated from i-t curve measured during the defect generation, the identification of a sweet spot for the power density is revealed.

Concluding, the defect development is likely based on local power density peaks. At this point, the modelling of the defect size is afflicted with uncertainty. Furthermore, the simplified 3D model used is also a significant source of errors.

A variation of the simulated defect size and thickness showed that an initial defect development at the silicon-dielectric interface leads to a reduced heat evacuation ability. An inhomogeneous electric field across the dielectric material could also create locally increased power densities. Finally, the generation of a locally oxidised insulation layer has a significant impact on the heat evacuation abilities. Even though it remains unclear at this point what could have triggered a local oxidation of copper or silicon, it can be said that such a process would result in an acceleration of heat accumulation.

Concluding, it has been shown that the thermal properties during a SBD defect generation can be modelled using numerical simulations. However, the simplified model used leaves uncertainties. A development of an accurate model would require a separate study.

## 6.7 Electro-optical frequency mapping

### 6.7.1 Measuring an electro-optical frequency mapping characteristic

The previous chapters have outlined the path to perform physical analyses of soft breakdown (SBD) defects. The results obtained have been discussed, and a subsequent numerical modelling of the defect has simulated the thermal conditions during the degradation. However, this chapter describes an alternative SBD characterisation technique, which also has the potential to localise these defects.

The measurement principle of electro-optical frequency mapping (EOFM) is described in chapter 5.4.1. A metal insulator semiconductor (MIS) structure is predestined for EOFM measurements. The voltage dependent modification of the charge carrier density at the silicon-insulator interface is well described in the literature, e.g. in [49]. A series of EOFM measurements with varying input amplitudes from a single non-stressed MIS structure is performed to analyse the voltage dependent EOFM response. In order to measure this series, the device under test (DUT) was stimulated with a square wave pulse with a duty cycle of 50%. A variation of the input amplitude from -10V to +10V in steps of 2V modified the bulk charge carrier density at the silicon-insulator interface. The result of the EOFM measurement series is shown in Figure 76. A dependency of the EOFM signal intensity to the applied voltage can be identified immediately.

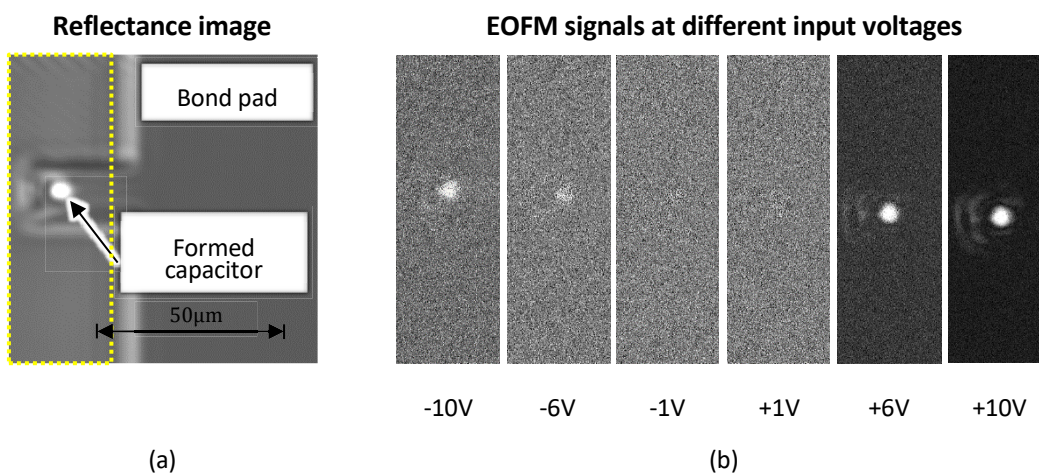
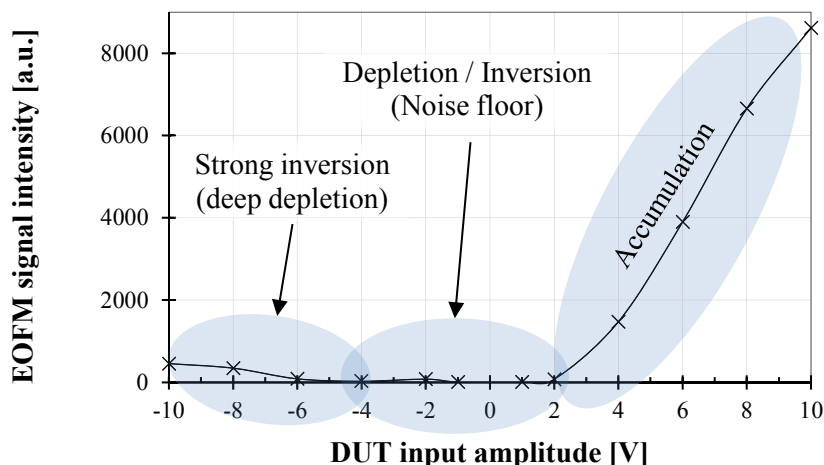


Figure 76: Selection of measurements from a complete EOFM characteristic measurement series from -10V to 10V

An extraction of an EOFM characteristic from this kind of measurement series was developed during the research carried out for this thesis. The EOFM characteristic is extracted by calculating the median value of the EOFM signal within the test structure region. The determined median value and the corresponding level of the applied device stimulation voltage generate a data point for the EOFM characteristic. The EOFM characteristic that is extracted from the measurement series presented in Figure 76, is shown in Figure 77. When analysing the forward-biased part of the extracted EOFM characteristic, a linear dependency between the EOFM signal intensity and the input amplitude can be observed. Thus, the signal intensity in forward-bias is higher compared to the signal intensity in negative voltages.



**Figure 77: Dependency of the EOFM signal intensity and the DUT stimulation voltage creates an EOFM characteristic**

Among other dependencies, EOFM is sensitive to changes in the optical properties of the analysed area of interest, especially the index of refraction [18]. Chapter 5.4.1.1 showed that the change of the index of refraction ( $\Delta n$ ) as well as the change of the absorption coefficient ( $\Delta\alpha$ ) of silicon are linearly dependent on the concentration of the free charge carrier ( $\Delta N_e; \Delta N_h$ ). The silicon free charge carrier concentration at the silicon insulator interface, within an MIS system, is adjustable by applying an external voltage. The voltage applied generates a silicon band bending ( $\Psi_{Si}$ ) which is linked directly to the free charge carrier concentration by Equation 8.

$$Q_{Si} = \pm \sqrt{2\epsilon_{Si}k_B T N_A \left[ \left( \exp\left(\frac{q\Psi_{Si}}{kT}\right) - \frac{q\Psi_{Si}}{k_B T} - 1 \right) + \frac{n_i^2}{N_A^2} \left( \exp\left(-\frac{q\Psi_{Si}}{kT}\right) + \frac{e\Psi_{Si}}{k_B T} - 1 \right) \right]}$$

**Equation 8: Charge carrier concentration in relation to the silicon band bending for an n-doped substrate**

Figure 78 shows the logarithmic concentration of the free charge carrier ( $Q_{Si}$ ) of a MIS system with an n-substrate in relation to the silicon band bending ( $\Psi_{Si}$ ). With accumulation and strong inversion, the concentration of the free charge carrier is exponentially related to the band bending. However, in terms of voltage, the band bending is “pinned” in these two regions. This can be seen in the capacitance voltage diagram of an MIS structure shown in Figure 79. In the event of accumulation and strong inversion, the capacitance of the MIS system can be approximated as a plate capacitor, its voltage independent capacity ( $C_{ox}$ ) being characterised by the insulating layer. In this region, any further applied voltage is consumed by the dielectric layer rather than by the silicon. This leads to a linear dependency between the applied voltage and the generated charge ( $Q_{Si} = C_{ox} \cdot V$ ). Furthermore, for the strong inversion one limitation must be considered: The strong inversion is an accumulation of minority carrier at the silicon insulator interface. In a MIS system, the time to accumulate minority carriers is limited by the intrinsic charge carrier generation rate, typically a few 100kHz. Whereas for a MIS system with adjacent diffusion regions, minority carriers are delivered with nearly no delay from these diffusions. This circumstance is well known from MIS capacitance characteristics, as shown in Figure 79. At high frequencies in reverse-bias, the MIS capacitance remains in deep depletion. Thus, the system can store

## 6. Results

less charge compared to the same system measured with the same voltage at lower frequencies. The influence of this effect on the free charge carrier band bending diagram is also shown in Figure 78.

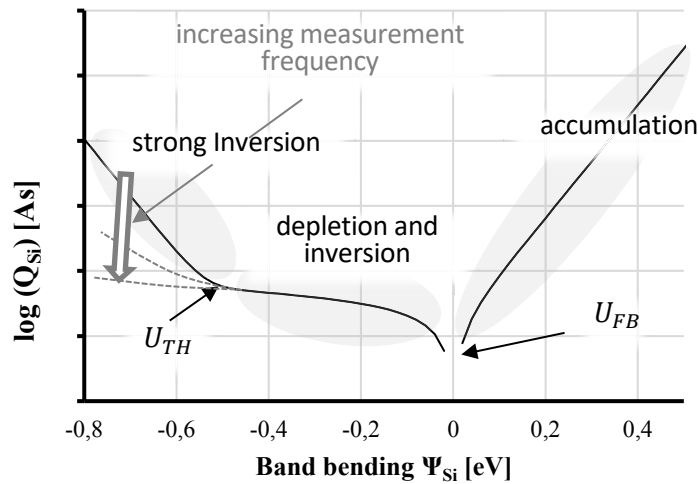


Figure 78: Free carrier density in a MIS system with n-substrate in relation to the silicon band bending

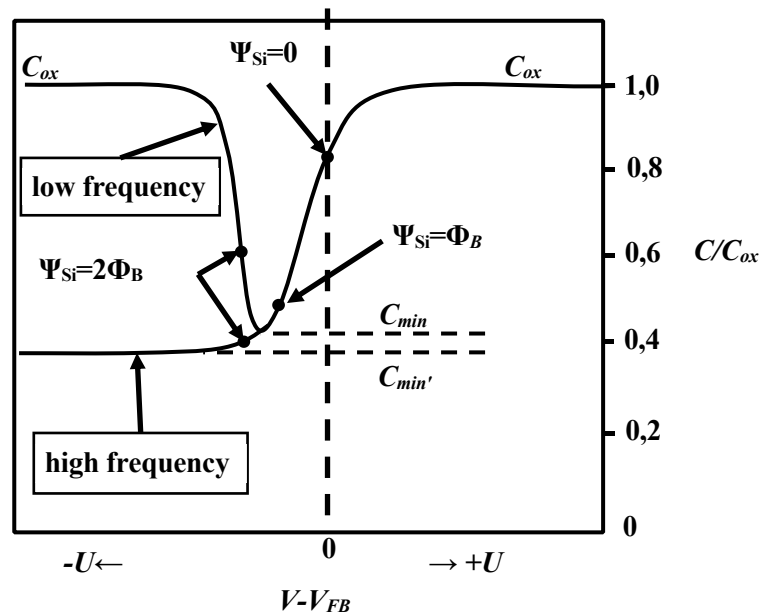


Figure 79: C-V characteristic of an MIS structure with n-substrate

Taking into account the limitations discussed, it is possible to understand the EOFM characteristic shown in Figure 77. The linear part of the forward bias shows the area of accumulations. This linear part of the curve is preceded by the depletion and inversion domain, in which the charge carrier concentration is determined by the doping concentration, and the electrically generated change in the charge carrier concentration is too small to measure a significant EOFM signal. The inversion is preceded by the strong inversion, featuring a linear relation between the applied voltage and the measured EOFM amplitude. However, due to the high measurement frequency of 1MHz, the absolute value of the slope is lower than that of the accumulation. Even though further experiments with

lower stimulation frequencies have not been performed in the framework of this thesis, it has been shown that EOFM is a capable method for device characterisation. In the case of MIS structures, the different operation modes can be identified. Furthermore, the theoretical fundamentals allow to identify the flat-band voltage ( $U_{FB}$ ) as well as the threshold voltage ( $U_{TH}$ ) from the transition points of the different operating modes. EOFM is not a technique commonly used for device characterisation. Thus, generating an EOFM characteristic as shown is an experimental approach to use this technique as a device characterisation tool. The presented utilisation of EOFM enables to identify the different operating modes of the MIS test structure. In the specific case of a degradation monitoring, the monitoring of the shifting  $U_{FB}$  with EOFM is presented in the next chapter.

### 6.7.2 Degradation monitoring with electro-optical frequency mapping

An EOFM characteristic of an unstressed low  $k$  dielectric MIS test structure has been discussed in the previous chapter. However, the main topic of this work is the localisation and characterisation of soft breakdown (SBD) defects. Thus, EOFM characteristics have been measured and analysed on four different levels of degradation in order to evaluate the influence of the degradation on the EOFM characteristic. A ramped voltage stress with a current compliance is used to degrade the structures. The advantages and the limitations of these stress procedure have been discussed in detail in chapter 6.1. At this point, a short turnaround time is desirable for proof of concept measurements.

Analysed were a non-stressed structure, a SBD defect with a leakage current of 100pA, a defect with a 10nA leakage current, which is on the transition from SBD to hard breakdown (HBD), and finally a HBD defect with a current of 1 $\mu$ A. Figure 80 illustrates the analysed degradation levels.

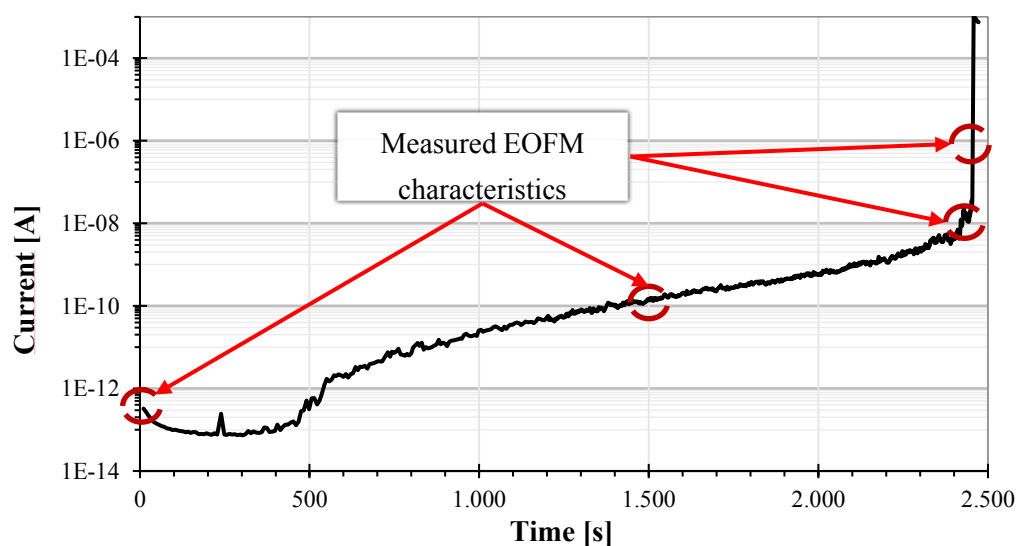


Figure 80: Levels of degradation analysed with EOFM characteristics

The corresponding EOFM characteristics can be seen in Figure 81. A clear modification in the EOFM characteristics can be observed with an increasing level of degradation. Under positive bias, an accumulation can be expected if the EOFM signal intensity is linearly

## 6. Results

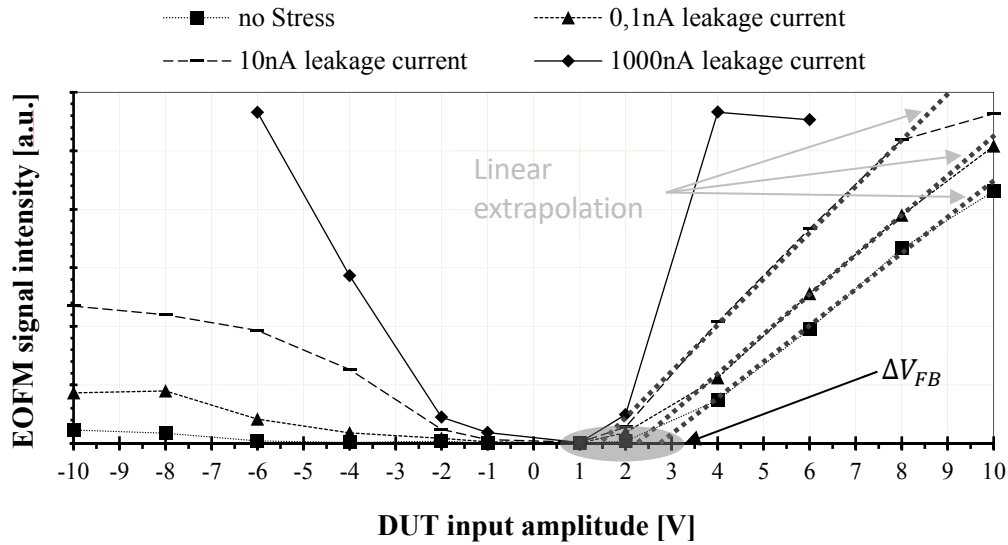


Figure 81: EOFM characteristics from different levels of degradation

related to the stimulation voltage. The transition from depletion to accumulation identifies the flat band voltage. In the curves shown, the exact determination of the transition point is blurred due to the noise floor discussed in the previous chapter. In any case, the linear extrapolation of the positive voltage domain allows the determination of the shift in the flat band voltage as degradation progresses. The flat band voltage shift for the different levels of degradation is summarised in Table 4. Despite the flat-band voltage shift during the HBD, a trend can be identified: The flat-band voltage is reduced with ongoing degradation. The significant morphological material changes during HBD, which has been discussed in chapter 6.5.2, agree with the different EOFM characteristics of the HBD defect compared to the other EOFM characteristics. The different EOFM characteristics between SBD and HBD are also present at reverse bias., An increasing absolute slope with increasing degradation can be observed for the SBD. Overall, the slopes are still lower compared to a positive bias. The EOFM characteristic of the HBD, again, does not fit into the pattern of the SBD characteristics.

Degradation level	no stress	100pA	10nA	1 $\mu$ A
$\Delta V_{FB}[V]$	0	-0.65	-1.4	-1.05
Defect type	None	SBD	SBD/HBD	HBD

Table 4: Flat band shift overview during degradation

Concluding, a series of EOFM measurements can be merged in order to measure an EOFM characteristic. This characteristic can be used to obtain insight into the charge carrier density of a MIS system. A series of EOFM characteristics can be used to monitor the degradation of a MIS test structure. A key parameter is the monitoring of the flat-band voltage shift for different levels of degradation. It has been found that an increased degradation increases the rate at which minority carriers can be delivered to the

semiconductor insulator interface in order to build an inversion layer. These minority carriers are likely delivered via the increased leakage current through the dielectric layer.

As the results presented of EOFM as a device characterisation method are novel, there is room for further improvements, which will give even more insight into the device and its degradation process. For example, measurements with lower input frequencies would also allow the threshold voltage to be extracted and monitored. In perspective, the 2D information about the relative charge carrier density distribution is provided by EOFM measurements has the potential to visualise the field distribution within a MIS system. Thus, a dedicated proof of concept measurement for defect localisation with EOFM is desirable. Defect localisation with EOFM would benefit from the relatively low device stimulation voltages, which significantly reduce the degradation during the defect localisation compared to localisation based on thermal laser or photon emission. If no 2D information is desired, electro optical probing (EOP) represents an alternative to EOFM. EOP measurements can be performed faster. Analysing the measured EOP waveform can be beneficial to obtain more specified information about the device at a single measurement point. However, for monitoring a device degradation, it can be difficult to ensure that the EOP measurement spot includes the defect. Thus, especially for larger BEOL test structures the 2D information from EOFM measurements is essential.

### 6.8 Experiments for future applications – OBIRCH with a SNOM

At the beginning of the research carried out in the framework of this thesis, different activities had been started in parallel. One track was the development of localisation techniques that can be used to detect soft breakdown defects. The path of this track has been outlined throughout the thesis. However, concerns about sufficient spatial measurement resolutions were addressed from the beginning. Consequentially, a second track dealt with possibilities to improve the resolution of the evaluated localisation techniques. As research progressed, it was found that the available resolution is not the limiting factor in locating a soft breakdown defect. At this point, the development of methods to improve the resolution was stopped. Nevertheless, the results made on this track are worth mentioning.

A commercial way to increase the optical resolution of an existing optical system is the application of a solid immersion lens (SIL). The effect of a SIL has been discussed in chapter 5.2.5. However, in 6.2 it was shown that the SIL was not required to increase the optical resolution but to increase the systems detection sensitivity for photon emission measurements. A different approach evaluated the utilisation of the non-diffraction limited near field optics resolution.

#### 6.8.1 Optical near field measurements

The transformation of a standard scanning near field optical microscopy (SNOM) setup into a near field OBIRCH setup is described in chapter 5.5.5. The current chapter shows first OBIRCH measurement results that were measured with a modified SNOM setup. A simplified test structure is used to verify the new measurement technique. The test structure consists of a polysilicon resistor that is connected to the overlying metal layer. The resistor is covered with inter-level dielectric as well as inter-metal dielectric. The test structure is operated with a constant voltage of 25mV. Figure 82 shows the near field OBIRCH measurement of the electrically operated poly-silicon test structure. Figure 82a shows the measured height information. The buried resistor is not identifiable from the height information image. Figure 82b shows the measured near field OBIRCH image. A clear OBIRCH signal can be identified. In Figure 82c, showing an overlay of the height and the

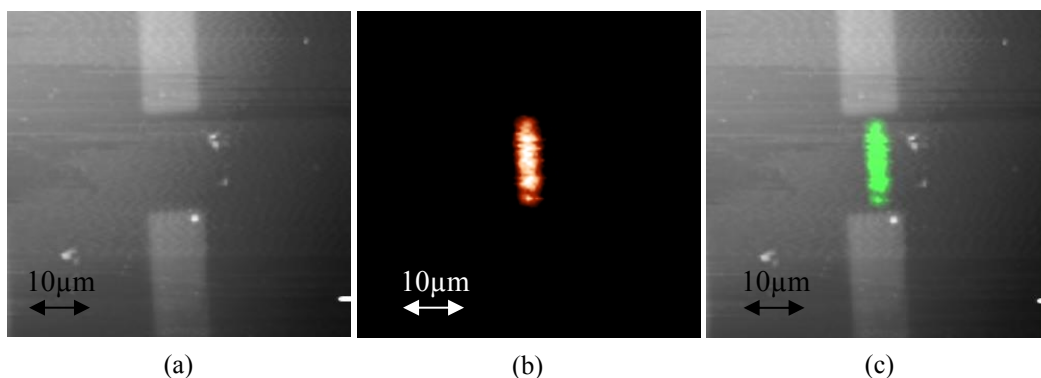
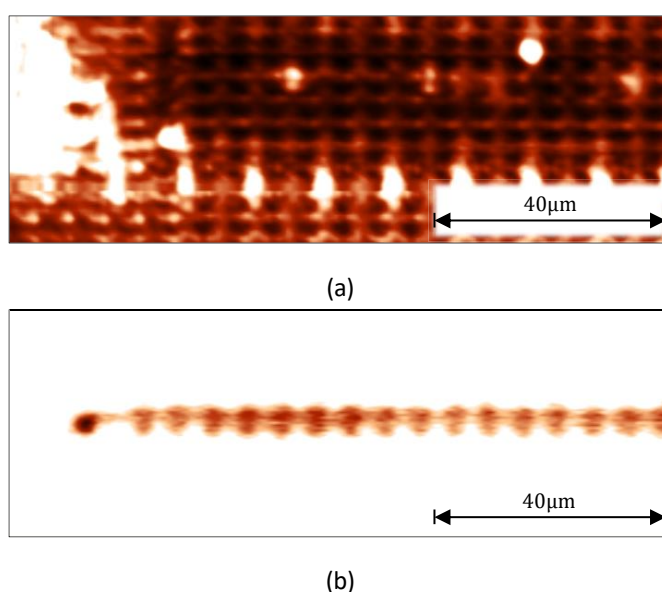


Figure 82: Scanning near field optical microscopy measurement of a buried poly silicon resistor; (a) height information; (b) OBIRCH image; (c) superposition of height and OBIRCH image

OBIRCH signal, the path of the current flow can be identified as straight between the metal lines. As the test structure is known, the location of the OBIRCH signal can be identified as the location of the buried resistor. At this point it can be stated that the OBIRCH technique can be successfully transferred into a SNOM system. At 532nm, however, the wavelength of the SNOM laser can generate pairs of electron holes within the poly silicon resistor. Thus, the measured OBIRCH signal is likely to be affected by generated electron hole pairs. Nevertheless, Figure 83 shows a SNOM OBIRCH measurement on a buried metal line. The jagged OBIRCH signal is caused by metal fill shapes that partially shade the analysed metal layer. Unfortunately, the results suffered from a defective SNOM controller, which led to the destruction of the SNOM tip during the measurements. Another problem that needs to be addressed is the adherence of the near field conditions. Depending on how deep the analysed structure is buried, the distance to the SNOM tip can be larger than the laser wavelength used. This would violate the condition for using the rule set of near field optics and the resolution will be diffraction limited.



**Figure 83: Scanning near field optical microscopy measurement of a buried metal line; reduced optical resolution due to defective SNOM tip; (a) reflection image; (b) OBIRCH image**

Concluding, OBIRCH measurements can be transferred to a SNOM system. The potential of a near field limited optics resolution limit is promising, however, the sensitivity limitations described in chapter 6.4 persist.

## 7 Conclusion

Throughout the previous chapters an in-depth study of failure analysis on specialised low k dielectric test structures was shown. The path to achieve reproducible and explainable defect signatures from soft breakdown (SBD) and hard breakdown (HBD) states is described in detail. Based on the electrical characterisation of the available test structures, a comprehensive analysis of different failure localisation methods follows. The physical analysis of localised failures as well as supportive failure analysis measurements give a first insight into the defect development.

The reliability characterisation of the time-dependent dielectric breakdown (TDDB) is performed with the aid of multiple electrical measurements and subsequent statistical evaluation. In contrast to this stands the evaluation of physical analysis of individual samples in order to conclude on the defect development, or the significance of the samples shown in this thesis, respectively. Among the available test structure sizes, the  $2\mu\text{m} \times 2\mu\text{m}$  samples showed a negligible variance in their voltage dependent degradation behaviour. Consequently, the physical analyses shown are representative of the test structure type analysed. The archived possibility to physically analyse early states of degradation, the SBD, allows to deepen the understanding of the defect development. This was due to the utilisation of dielectric test structures developed by imec, consisting of a metal insulator semiconductor (MIS) material stack, which opened the field for a variety of methods for failure analysis.

### 7.1 Defect localisation

Different failure localisation methods have been evaluated for their capability to localise SBD defects with sample resistances of several G $\Omega$  and higher. Such high sample resistances require extraordinary measurement sensitivity.

#### 7.1.1 Photon emission microscopy

Of the available localisation techniques, photon emission microscopy (PEM) with an InGaAs detector and a silicon solid immersion lens (SIL) has proven to be the most sensitive localisation technique. Thus, the detection of SBD defects with sample resistances of  $\sim 200\text{G}\Omega$  is possible on a regular basis. In the past, defects with such a high resistance could only be analysed if localisation was not required, since the test structure itself localised the defect, which is only possible on non-area-related test structures. The developed possibility of detecting defects with such a high sample resistance or low leakage currents is not only important for the presented application, but it is also likely that these findings will enrich the field of semiconductor device failure analysis.

The limiting factor for further sensitivity improvements of PEM measurements with an InGaAs detector is the material-caused internal noise generation of the detector. Thus, no further improvements are expected for the available setup. However, PEM experiments with a Si-CCD revealed potential to improve sensitivity. An ultra-thinned bulk silicon would

neglect the drawback of the spectral sensitivity of the Si-CCD and release the full potential of the low noise generating Si-CCD detector.

### 7.1.2 *Optical beam induced resistance change*

The ability to localise a SBD defect in low k materials with the help of optical beam induced resistance change (OBIRCH) measurements was demonstrated. Even though, the detection sensitivity achieved was inferior to PEM measurements, the limiting factors were clearly identified. The input resistance of the available voltage amplifier is  $100\text{M}\Omega$ , which is orders of magnitude lower than the resistance of the analysed samples in extremely low degradation states. Under this condition, the measurement principle of OBIRCH no longer works properly, since the major part of the stimulating current flowed through the amplifier rather than the defect. The localisation of a SBD defect with a  $1\text{nA}$  leakage current from a  $20\text{G}\Omega$  sample was best achievable sensitivity.

A significantly improved detection sensitivity can be expected by implementing specially developed amplifiers with an input resistance in the same order of magnitude or even higher as the analysed sample. Under these circumstances, the theoretical superiority of OBIRCH over PEM for high resistance samples could be unlocked.

## 7.2 Physical analysis

The defect development of a stressed low k dielectric was sketched with the help of physical analysis of defects with different levels of degradation. An influence of the electrical stress method on the defect morphology was identified. Although the electrical characteristics of the different stress methods indicate interchangeability, the physical analysis showed a characteristic detail for defects generated by electrical stress methods using a voltage overstress.

The depth information about the defect shape, which was obtained by scanning electron microscopy (SEM) in combination with a continuous ablation of material through a focused ion beam, was essential for understanding the analysis on sample lamellas.

However, the measurement of a sample lamella using transmission electron microscopy (TEM) is inevitable to expose the details of the defect morphology. In particular the scanning TEM energy dispersive x-ray analysis (STEM-EDEX) is extraordinary useful for the reconstruction of the material movement within the defect area.

## 7.3 Non Invasive defect analysis

Apart from defect localisation, failure analysis offers the possibility of characterising the failure. Spectral photon emission microscopy (SPEM) in particular contributed to

## *7. Conclusion*

indispensable defect attributes that were necessary to understand the physical analysis. Monitoring the SPEM parameter electron temperature for varying levels of degradation revealed a clear separation between the soft breakdown and hard breakdown domain. Whereas the electron temperature is variable in soft breakdown, it is constant for different levels of hard breakdown. However, physical analysis of different hard breakdown levels revealed morphological differences that could not be understood without SPEM measurements.

## 8 Epilogue

The ever-increasing complexity of today's problems in the field of semiconductor industry necessitates an increased collaborative effort of different sub-areas. Due to the constantly shrinking structure sizes, the interdependency between the different parts of a silicon die increases. Departments that were historically strictly separate, such as the front end of line and the back end of line departments, are now forced to work together much closer and find solutions to their problems that do not adversely affect the other departments concerned. It is therefore vital for the involved scientists to know about the departments that are related to and influence the problems examined. This maxim is also applicable to the semiconductor failure analysis. The pure application of failure analysis methods without a deeper understanding of the underlying problem is unlikely to solve the problem in the best possible way, or worse, it could result in a misinterpretation of the results. Vice versa, it will be difficult to solve state of the art problems without knowing about the underlying basics of the failure analysis methods available.

Developing soft breakdown localisation techniques and investigating the degradation process of a soft breakdown defect is a good example of a synergy between different fields of knowledge. The development of the ultra sensitive localisation techniques required an understanding of the underlying device reliability. The physical analysis of the localised soft breakdown defects and their interpretation was merely possible due to the combination of knowledge from the field of semiconductor failure analysis, physical analysis, and back end of line reliability. Not losing the perspective and considering the special needs of the different fields of knowledge is challenging but rewarding. This thesis gave a first impression of the soft breakdown defect development based on physical analysis and on results of advanced failure characterisation methods.

Emphasising the need for increased collaborative efforts of multiple fields of knowledge increases the difficulty for new scientists to access scientific problems. On the other hand, it strengthens the need for passionate supervisors who are not afraid to share their experience with the next generation of scientists.

## 9 References

- [1] K. Croes *et al.*, “Current Understanding of BEOL TDDB Lifetime Models,” *ECS Journal of Solid State Science and Technology*, vol. 4, no. 1, N3094-N3097, 2014, doi: 10.1149/2.0101501jss.
- [2] L. Zhao, Z. Tokei, G. G. Gischia, M. Pantouvaki, K. Croes, and G. Beyer, “A novel test structure to study intrinsic reliability of barrier/low-k,” in *IEEE International Reliability Physics Symposium, 2009: IRPS 2009 ; 26 - 30 April 2009, Montreal, QC, Canada*, Montreal, QC, Canada, 2009, pp. 848–850.
- [3] L. Zhao, Z. Tikei, G. G. Gischia, H. Volders, and G. Beyer, “A new perspective of barrier material evaluation and process optimization,” in *IEEE International Interconnect Technology Conference, 2009: IITC 2009 ; 1 - 3 June 2009, Royton Sapporo Hotel, Sapporo, Japan*, Sapporo, Japan, 2009, pp. 206–208.
- [4] C. Wu, “In-depth understanding of low-k dielectric reliability in interconnect system,” Dissertation, 2016.
- [5] L. Zhao *et al.*, “Role of copper in time dependent dielectric breakdown of porous organo-silicate glass low-k materials,” p. 222110.
- [6] *Koaxialkabel – Wikipedia*. [Online]. Available: <https://de.wikipedia.org/wiki/Koaxialkabel> (accessed: Mar. 29 2020).
- [7] *Triaxialkabel – Wikipedia*. [Online]. Available: <https://de.wikipedia.org/wiki/Triaxialkabel> (accessed: Mar. 29 2020).
- [8] A. Wadsworth, *The Parametric Measurement Handbook: 4th Edition*. [Online]. Available: <https://www.keysight.com/de/de/assets/7018-05884/application-notes/5992-2508.pdf> (accessed: Mar. 29 2020).
- [9] *4200A-SCS Parameter Analyzer Datasheet | Tektronix*. [Online]. Available: <https://de.tek.com/datasheet/4200a-scs-parameter-analyzer> (accessed: Apr. 25 2020).
- [10] A. Kim, E. Wu, B. Li, and B. Linder, “Transformation of Ramped Current Stress V BD to Constant Voltage Stress TDDB T BD,” in *2019 IEEE International Reliability Physics Symposium (IRPS)*, Monterey, CA, USA, Mar. 2019 - Apr. 2019, pp. 1–5.
- [11] T. Nigam, R. Degraeve, G. Groeseneken, M. M. Heyns, and H. E. Maes, “Constant current charge-to-breakdown: Still a valid tool to study the reliability of MOS structures?,” in *1998 IEEE International Reliability Physics Symposium proceedings: 36th annual, Reno, Nevada, March 31, April 1, 2, 1998*, Reno, NV, USA, 1998, pp. 62–69.
- [12] “Photon Emission in Silicon Based Integrated Circuits,” in *Microelectronics failure analysis: Desk reference*, T. Gandhi, Ed., Materials Park, Ohio: ASM International, 2019, pp. 180–195.
- [13] C. Boit, “Fundamentals of Photon Emission (PEM) in Silicon – Electroluminescence for Analysis of Electronic Circuit and Device Functionality,” in *Microelectronics failure analysis: Desk reference*, 5th ed., Materials Park, OH: ASM International, 2004, pp. 356–368.
- [14] R. Soref and B. Bennett, “Electrooptical effects in silicon,” *IEEE J. Quantum Electron.*, vol. 23, no. 1, pp. 123–129, 1987, doi: 10.1109/JQE.1987.1073206.

- [15] H. Lohrke *et al.*, “Contactless Fault Isolation for FinFET Technologies with Visible Light and GaP SIL,” *ISTFA 2016*, 2016.
- [16] J.C.H. Phang *et al.*, “A review of near infrared photon emission microscopy and spectroscopy,” in *Proceedings of the 12th International Symposium on the Physical & Failure Analysis of Integrated Circuits: IPFA 2005 : [27 June to 1 July 2005, Shangri-La's Rasa Sentosa Resort, Singapore]*, Shangri-La's Rasa Sentosa Resort, Singapore, 2005, pp. 275–281.
- [17] P. Scholz, “Focused Ion Beam Created Refractive and Diffractive Lens Techniques for the Improvement of Optical Imaging through Silicon,” 2012.
- [18] U. Kindereit, “Fundamentals and future applications of Laser Voltage Probing,” in *2014 IEEE International Reliability Physics Symposium (IRPS 2014): 1-5 June 2014, Waikoloa, HI, Waikoloa, HI, USA, 2014*, 3F.1.1-3F.1.11.
- [19] S. M. Sze and K. K. Ng, *Physics of semiconductor devices*, 3rd ed. New Dehli: Wiley-India, 2007.
- [20] W. Lo, N. Nataraj, N. Boiadjieva, P. Vedegarbha, and K. Wilsher, “Polarization difference probing: A new phase detection scheme for laser voltage probing,” *Proceedings of the 30th International Symposium for Testing and Failure Analysis, ISTFA 2004*, pp. 9–17, 2004.
- [21] U. Kindereit, “Investigation of laser-beam modulations induced by the operation of electronic devices,” 2009.
- [22] L. V. Keldysh, “Behavior of non-metallic crystals in strong electric fields,” *Soviet Journal of Experimental and Theoretical Physics*, vol. 6, p. 763, 1958.
- [23] L. V. Keldysh, “The effect of a strong electric field on the optical properties of insulating crystals,” *Sov. Phys. JETP*, vol. 7, no. 5, pp. 788–790, 1958.
- [24] T. S. Moss, G. J. Burrell, and B. Ellis, *Semiconductor opto-electronics*: Butterworth-Heinemann, 2013.
- [25] H. K. Heinrich, B. R. Hemenway, R. A. Marsland, and D. M. Bloom, “A Noninvasive Optical Probe for Detecting Electrical Signals in Silicon IC’s,” in *Review of Progress in Quantitative Nondestructive Evaluation: Volume 7B*, D. O. Thompson and D. E. Chimenti, Eds., Boston, MA: Springer US, 1988, pp. 1161–1166. [Online]. Available: [https://doi.org/10.1007/978-1-4613-0979-6\\_34](https://doi.org/10.1007/978-1-4613-0979-6_34)
- [26] *Principles of Lock-in Detection | Zurich Instruments*. [Online]. Available: <https://www.zhinst.com/others/resources/principles-lock-detection> (accessed: Mar. 3 2020).
- [27] A. Firiti, D. Lewis, F. Beaudoin, P. Perdu, G. Haller, and P. Fouillat, “Photoelectric laser stimulation in a failure analysis laboratory,” 101–104 vol. 1, doi: 10.1109/ISIE.2004.1571789.
- [28] *Thermocouple - Wikipedia*. [Online]. Available: <https://en.wikipedia.org/wiki/Thermocouple> (accessed: Mar. 7 2020).
- [29] F. Beaudoin, Desplats R., P. Perdu, and C. Boit, “Principles of Thermal Laser Stimulation Techniques,” in *Microelectronics failure analysis: Desk reference*, 5th ed., Materials Park, OH: ASM International, 2004, pp. 417–425.
- [30] L. Novotny, D. W. Pohl, and P. Regli, “Near-field, far-field and imaging properties of the 2D aperture SNOM,” *Ultramicroscopy*, vol. 57, 2-3, pp. 180–188, 1995, doi: 10.1016/0304-3991(94)00133-8.

## 8. Epilogue

- [31] J. W.P. Hsu, "Near-field scanning optical microscopy studies of electronic and photonic materials and devices," *Materials Science and Engineering: R: Reports*, vol. 33, no. 1, pp. 1–50, 2001, doi: 10.1016/S0927-796X(00)00031-0.
- [32] D. W. Pohl and D. Courjon, *Near Field Optics*. Dordrecht: Springer, 1993. [Online]. Available: <http://site.ebrary.com/lib/alltitles/docDetail.action?docID=10654431>
- [33] W. Boxleitner, G. Hobler, V. Klüppel, and H. Cerva, "Simulation of topography evolution and damage formation during TEM sample preparation using focused ion beams," *Nuclear Instruments and Methods in Physics Research Section B: Beam Interactions with Materials and Atoms*, 175-177, pp. 102–107, 2001, doi: 10.1016/S0168-583X(01)00334-2.
- [34] *An Introduction to Electron Microscopy - SEM : consists of an electron optical column, a vacuum system, electronics, and software | Thermo Fisher Scientific*. [Online]. Available: <https://www.fei.com/introduction-to-electron-microscopy/sem/> (accessed: Apr. 14 2020).
- [35] G. D. Danilatos, "Foundations of Environmental Scanning Electron Microscopy," in *Advances in Electronics and Electron Physics*, v. 71, *Advances in electronics and electron physics*, P. W. Hawkes, Ed., Boston: Academic Press, 1988, pp. 109–250.
- [36] *Dennis McMullan Scanning Microscope*. [Online]. Available: <http://www-g.eng.cam.ac.uk/125/achievements/mcmullan/mcm.htm> (accessed: Apr. 14 2020).
- [37] M. von Ardenne, "Das Elektronen-Rastermikroskop," *Z. Physik*, vol. 109, 9-10, pp. 553–572, 1938, doi: 10.1007/BF01341584.
- [38] L. A. Giannuzzi and F. A. Stevie, "A review of focused ion beam milling techniques for TEM specimen preparation," *Micron*, vol. 30, no. 3, pp. 197–204, 1999, doi: 10.1016/S0968-4328(99)00005-0.
- [39] P. D. Nellist, "The Principles of STEM Imaging," in *Scanning transmission electron microscopy: Imaging and analysis*, S. J. Pennycook and P. D. Nellist, Eds., New York, NY: Springer, 2011, pp. 91–115.
- [40] H. Kohl and L. Reimer, *Transmission Electron Microscopy: Physics of Image Formation*. New York, NY: Springer-Verlag New York, 2008.
- [41] C. Helfmeier, A. Beyreuther, A. Fox, and C. Boit, "Ultra sensitive measurement of dielectric current under pulsed stress conditions," *Microelectronics Reliability*, vol. 55, no. 11, pp. 2254–2257, 2015, doi: 10.1016/j.microrel.2015.06.119.
- [42] C. Wu, Y. Li, J. Bommels, I. de Wolf, Z. Tokei, and K. Croes, "New breakdown mechanism investigation: Barrier metal penetration induced soft breakdown in low-k dielectrics," in *2016 International Reliability Physics Symposium*, Pasadena, CA, USA, 2016, 3A-2-1-3A-2-6.
- [43] R. Pagano *et al.*, "A novel approach to characterization of progressive breakdown in high-k/metal gate stacks," *Microelectronics Reliability*, vol. 48, no. 11, pp. 1759–1764, 2008, doi: 10.1016/j.microrel.2008.07.071.
- [44] C. Boit, H. Lohrke, P. Scholz, A. Beyreuther, U. Kerst, and Y. Iwaki, "Contactless visible light probing for nanoscale ICs through 10  $\mu$  m bulk silicon," 2015.
- [45] S. B. Ippolito, B. B. Goldberg, and M. S. Ünlü, "High spatial resolution subsurface microscopy," *Appl. Phys. Lett.*, vol. 78, no. 26, pp. 4071–4073, 2001, doi: 10.1063/1.1381574.

- [46] T. Breuer, *Untersuchung der Degradation von elektrisch gestresstem nano- porösem ultra low-k Dielektrikum vor dem elektrischen Durchschlag*. Zugl.: Berlin, Techn. Univ., Diss., 2012. Münster: Verl.-Haus Monsenstein u. Vannerdat OHG, 2012.
- [47] H. Okamoto, "Supplemental Literature Review of Binary Phase Diagrams: Ag-Ni, Ag-Zr, Au-Bi, B-Ni, Co-Sb, Cu-Mn, Cu-Si, Cu-Zn, Fe-Zr, Li-Sb, Mg-Pu, and Si-Zr," *J. Phase Equilib. Diffus.*, vol. 39, no. 1, pp. 87–100, 2018, doi: 10.1007/s11669-017-0610-3.
- [48] A. Kiani, K. Venkatakrisnan, and B. Tan, "Micro/nano scale amorphization of silicon by femtosecond laser irradiation," *Optics express*, vol. 17, no. 19, pp. 16518–16526, 2009, doi: 10.1364/OE.17.016518.
- [49] Y. Taur and T. H. Ning, *Fundamentals of modern VLSI devices*, 2nd ed. Cambridge: Cambridge Univ. Press, 2013.

## 10 List of Figures

Figure 1: Schematic drawing of a metal insulator semiconductor test structure; the aluminium on the back is removed locally to grant optical access to the bulk silicon and the test structure.....	19
Figure 2: Images of a analysed non-degraded test structures; (a) laser scanning microscope image measured from the back; (b) Cross section measured with a transmission electron microscope.....	19
Figure 3: Schematic drawing of coaxial and triaxial cable cross sections. ....	21
Figure 4: Printed circuit board package for low current measurements; (a) from the front side with moulded chip; (b) from the back side with the blank chip back side and aluminium substrate contact visible; (c) front side view of the non-moulded chip – showing the bond wires .....	23
Figure 5: Schematic drawing of the front panel of the low noise preamplifier SR560.....	24
Figure 6: (a) Band diagram of a pn - junction in forward bias; increased recombination due to an increased minority carrier concentration at the boundary of the space charge region and an increased carrier density in the space charge region; (b) Conduction band of a band diagram from a pn - junction in reverse bias; intra-band relaxation processes and resulting photon emission. ....	27
Figure 7: Schematic drawing of a photon emission measurement setup with the possibility to acquire a reflection image.....	28
Figure 8: (a) reflection image of a generic test structure; (b) generic photon emission measurement image; (c) superimposition of the reflection image and photon emission measurement.....	29
Figure 9: Photon energy related silicon absorption coefficient for different doping concentrations .....	29
Figure 10: Spectral sensitivity of photon emission microscopy detectors and wavelength dependent silicon transmission for $10\mu m$ and $100\mu m$ silicon thickness.....	30
Figure 11: Comparison of internal noise generation characteristics of an InGaAs and Si – CCD photon detector.....	31
Figure 12: Back side photon emission (a) without SIL, refraction and total reflection at the silicon surface occurs (b) with SIL refraction and total reflection is prevented.....	33
Figure 13: Schematic drawing of the dispersion on a prism .....	35
Figure 14: Dispersion characteristics of the prism used to measure the spectral photon emission from the back of the chip.....	36
Figure 15: Lens calibration factors for the spectral photon emission system used; factors determined from a calibration light source. Factors for different lenses are not comparable .....	36
Figure 16: Exemplary reconstruction of a photon emission spectrum: (a) image of the measured photon emission spot; (b) image of the measured photon emission with prism inserted into the optical path; (c) plotted spectral data; (d) photon emission spectrum...	37
Figure 17: Characteristic spectral distribution of recombination based photon emission (R – PE) and electrical field supported photon emission (F-PE) .....	39

Figure 18: Generic fully evaluated photon emission spectra with extracted electron temperature and specification of goodness of fit.....	40
Figure 19: Schematic drawing of an EOFM setup; EOFM signal generation only occurred if the reflected laser beam was dynamically modulated.....	43
Figure 20: Schematic setup of a laser scanning microscope with extensions for measuring changes in resistance induced by optical beams.....	46
Figure 21: (a) Generic OBIRCH measurement, (b) the corresponding reflection image and (c) the overlay of OBIRCH signal and reflection image.....	47
Figure 22: Schematic drawing to illustrate how near field optics can overcome the diffraction limit and thus achieve a sub-wavelength resolution. ....	48
Figure 23: Schematic setup of a scanning near field optical microscopy with a tuning fork to control the height.....	49
Figure 24: Schematic setup of a scanning near field optical microscopy with a tuning fork to control the height and additional extensions to allow resistance change measurements induced by optical beams. ....	50
Figure 25: Basic components of a dual beam system.....	52
Figure 26: Schematic drawing of the interaction volume generated when an electron beam strikes the sample surface and the generated electrons.....	52
Figure 27: Schematic drawing of image acquisition in transmission electron microscopy (a) TEM: The entire image is acquired at once; (b) scanning TEM: pointwise measurement of the image enables the use of different detectors to specify the evaluated signal.....	53
Figure 28: Ramped voltage stress measurements performed on different BEOL MIS test structure sizes. Error bars indicate the sample variation. ....	55
Figure 29: Constant voltage stress measurements on dielectric test structures. ....	57
Figure 30: Constant voltage degradation with a reduced voltage stress level to allow an identification of four degradation phases.....	57
Figure 31: A series of constant voltage stress measurements with varying levels of current compliance.....	59
Figure 32: Injected charge during constant voltage stress measurements with current compliance; the related constant voltage stress measurements are marked with dashed lines.....	60
Figure 33: Ramped voltage stress with a current compliance set to 100pA.....	61
Figure 34: Resistance over time of a ramped voltage stress with a current compliance. ....	62
Figure 35: Selected constant voltage stress measurements with self-healing effect of 100 $\mu$ m x 100 $\mu$ m back end of line test structures.....	63
Figure 36: Current density of ramped voltage stress measurements performed on different BEOL MIS test structure sizes. Error bars indicate the sample variation. ....	64
Figure 37: Superimposed photon emission signal and reflection image of a dielectric hard breakdown measured with a Si-CCD from the (a) front and (b) back.....	65
Figure 38: Leakage current of a dielectric test structure under constant voltage stress of 29V; Different windows for photon emission integration are marked.....	66

## 10. List of Figures

Figure 39: Leakage current of a 26.5V stressed low k MIS test structure; Adaptive photon emission measurement integration time windows are marked .....	67
Figure 40: Results of the photon emission measurement of a 26.5V constant voltage stressed low k MIS test structure; (a) laser scanning microscope reflection image; (b-e) photon emission results from integration windows 1-4 .....	68
Figure 41: Degradation curve of a constant voltage stresses low k MIS test structure with two subsequent current compliances of 1nA and 100nA. Red curve shows the sample resistance. Red shaded areas mark regions of photon emission measurements. ....	69
Figure 42: Back side photon emission measurement of a 100nA leakage current using an InGaAs detector; Defect localisation is possible within the 2 $\mu$ m x 2 $\mu$ m test structure .....	70
Figure 43: Comparison of the measured photon emission intensity (a) without solid immersion lens, 100s (5 frames with 20s each) integration 100nA leakage current 210M $\Omega$ sample resistance (b) x-z data plot of emission measurement without SIL (c) with solid immersion lens, 100s (5 frames with 20s each) integration 100nA leakage current 240M $\Omega$ sample resistance (d) x-z data plot of emission measurement with SIL .....	71
Figure 44: Leakage current and sample resistance of a 2 $\mu$ m x 2 $\mu$ m low k MIS test structure under 28V constant current stress with a 100pA current compliance. ....	72
Figure 45: Photon emission measurement on a 250G $\Omega$ sample with a leakage current of 100pA (a) emission image (b) emission image, superimposed with the InGaAs reflection image (c) emission image, superimposed with the laser scanning microscope reflection image.....	73
Figure 46: Degradation curve of a low k MIS test structure under a ramped voltage stress with a current compliance of 100pA; I-V curve shown on the primary axes shown in black; R-t curve shown in blue on the secondary axes (dashed) .....	74
Figure 47: Superimposed reflection image of the laser scanning microscope and photon emission image from a 100pA leakage current defect; a ramped voltage stress with current compliance was used to create the defect .....	75
Figure 48: Pre-stress degradation with a ramped voltage stress and a 10pA current compliance of sample A and sample B .....	75
Figure 49: Superimposition of a photon emission image with the reflection image of a laser scanning microscope; the photon emission was measured from a leakage current of 10pA .....	76
Figure 50: Subsequent constant voltage stress with a 25V stress level and a 100pA current compliance. Stress was applied after a pre-stress.....	77
Figure 51: Photon emission image from a 100pA leakage current from a 25V constant voltage stress following a pre-stress .....	77
Figure 52: Spectral photon emissions from a hard breakdown with varying current compliances. Initial current compliance of (a) 50nA and the endpoint current compliance of (b) 50 $\mu$ A are shown. ....	79
Figure 53: Photon emission spectra of a hard breakdown with stepwise increasing current compliance.....	80
Figure 54: Photon emission spectra of a soft breakdown with gradually increasing current compliance; Spectra are normalised at 0.85 eV .....	82

Figure 55: Measured spectral data from different leakage currents (a-b) 100pA; (c) 500pA; (d); 1nA.....	83
Figure 56: Extracted parameter electron temperature from three different samples with gradually increasing levels of degradation; Linear regression for each sample soft breakdown region.....	84
Figure 57: Optical beam induced resistance changes measurement on a structure in hard breakdown with the following varying currents: (a) Signal from a 1 $\mu$ A current and (b) the associated laser reflection image overlay; (c) Signal from a 1pA current and (d) the associated laser reflection image overlay.....	87
Figure 58: Soft breakdown defect detection with (a) optical beam induced resistance change and (b) the corresponding reflectance image overlay of a 20G $\Omega$ sample with a 1nA leakage current.....	88
Figure 59: Electron images of: (a) a hard breakdown from a metal-insulator-metal (MIM) test structure; (b) a corresponding cross section image of a MIM hard breakdown; (b) an unstressed MIM test structure; (d)a cross section of an unstressed MIM test structure...	90
Figure 60: Bright field scanning transmission electron microscopy image of a 1.3 $\mu$ m TEM lamella; (a)&(b) from sample MIS-A, a 250G $\Omega$ soft breakdown defect; (c)&(d) from sample MIS-B, a 260G $\Omega$ soft breakdown defect.....	91
Figure 61: 100nm TEM lamella from sample MIS-B, a 260G $\Omega$ soft breakdown defect (a) & (b) bright field scanning transmission electron microscopy image; (c) high-angle annular dark field image transmission electron microscopy image.....	92
Figure 62: Elemental mapping with energy dispersive x-ray analysis of a 100nm lamella of soft breakdown sample MIS-B. Shown is (a)Silicon (b)Copper (c)Oxygen (d) Carbon (e)Tantalum (f)an overlay of all elements shown.....	94
Figure 63: Energy dispersive x-ray analysis of a defect generated by ramped voltage stress with a current compliance of 100pA.....	96
Figure 64: Bright field transmission electron microscopy image of a 1.8 $\mu$ m thick sample lamella from a defect generated by ramped voltage stress with a current compliance of 10pA.....	97
Figure 65: In-lens detector image at different sample lamella thinning steps (a) thinning step number nine; (b) thinning step number eleven.....	98
Figure 66: Energy dispersive x-ray analysis of a 0.5 $\mu$ m thick sample lamella from a defect generated by ramped voltage stress with a current compliance of 10pA.....	98
Figure 67: Estimated 3D model of a soft breakdown defect within a low k dielectric metal insulator semiconductor test structure.....	99
Figure 68: Dark field transmission electron microscopy image of a 4k $\Omega$ hard breakdown defect.....	100
Figure 69: Energy dispersive x-ray analysis of a 4k $\Omega$ hard breakdown.....	101
Figure 70: High angle annular dark field transmission electron microscopy image of a 314k $\Omega$ hard breakdown defect.....	102
Figure 71: HAADF images of different 100nm thick sample lamellae: (a) a 260k $\Omega$ soft breakdown defect; (b) a 312k $\Omega$ hard breakdown defect; (c) a 4k $\Omega$ hard breakdown defect.....	103

## 10. List of Figures

Figure 72: Silicon - Copper phase diagram.....	105
Figure 73: Cross section of the created 3D model used to simulate the thermal conditions during the soft breakdown defect development.....	107
Figure 74: Cross section of the heat flux from the simulated test structure .....	107
Figure 75: Top view of the low k dielectric and its surface temperature distribution. Temperature distribution similar for applied power densities of $6 \cdot 10^{13} \text{ W} \cdot \text{m}^{-3}$ – $1 \cdot 10^{15} \text{ W} \cdot \text{m}^{-3}$ .....	108
Figure 76: Selection of measurements from a complete EOFM characteristic measurement series from -10V to 10V .....	110
Figure 77: Dependency of the EOFM signal intensity and the DUT stimulation voltage creates an EOFM characteristic /das Bild ist abgeschnitten.....	111
Figure 78: Free carrier density in a MIS system with n-substrate in relation to the silicon band bending .....	112
Figure 79: C-V characteristic of an MIS structure with n-substrate .....	112
Figure 80: Levels of degradation analysed with EOFM characteristics .....	113
Figure 81: EOFM characteristics from different levels of degradation .....	114
Figure 82: Scanning near field optical microscopy measurement of a buried poly silicon resistor; (a) height information; (b) OBIRCH image; (c) superposition of height and OBIRCH image.....	116
Figure 83: Scanning near field optical microscopy measurement of a buried metal line; reduced optical resolution due to defective SNOM tip; (a) reflection image; (b) OBIRCH image.....	117

## 11 List of Equations

Equation 1: Minimum distance ( $x_{min}$ ) to resolve two distinct light sources according to Rayleigh (Rayleigh criterion). $\Lambda$ is the considered wavelength, NA is the numerical aperture of the optical objective used. ....	32
Equation 2: Spectral distribution of an F - PE.....	39
Equation 3: Silicon index of refraction.....	41
Equation 4: Silicon absorption coefficient.....	41
Equation 5: Heat induced resistance change .....	44
Equation 6: Heat induced voltage alteration using a constant current source to stimulate the device under test .....	44
Equation 7: Heat induced current alteration using a constant voltage source to stimulate the device under test .....	44
Equation 8: Charge carrier concentration in relation to the silicon band bending for an n-doped substrate .....	111

## 12 List of Tables

Table 1: Electron temperatures extracted of a set of subsequently increasing current compliances of a single sample .....	80
Table 2: Soft breakdown electron temperatures at different current levels .....	83
Table 3: Layer parameters used for the thermal model .....	106
Table 4: Flat band shift overview during degradation .....	114